

# The critical role of architecture in constraining fluid-flow and chemical gradients in Late Archean Gold Systems, eastern Yilgarn Craton

Adam B. Bath and John L. Walshe

Mineral Resources, CSIRO, Kensington, WA, Australia

**Abstract.** Deposit- to camp-scale quantified mineral maps have been generated for numerous Archean gold systems within the Yilgarn Craton to delineate gold mineral systems. Zoning of minerals produced by hydrothermal alteration are traced using energy-dispersive x-ray spectral measurements from the scanning electron microscope (SEM; 1000s of samples), textural SEM phase maps, whole-rock multi-element geochemistry and trace elements of select mineral phases. We show that fluid pathways in Archean gold systems can be strongly controlled by the architecture (both structural and lithological). Impermeable or weakly permeable talc-rich ultramafic and thick coherent phenocryst-rich mafic volcanics occur in the hanging-wall of ore-zones. Footwall domains contain broad (>100m) alteration zones with minerals, such as anhydrite paragenetically linked to mineralisation. Footwall pyrite-anhydrite domains transition into pyrrhotite-domains into mineralised zones, indicating chemical redox gradients. Other minerals (micas, chlorite, sulphides, amphibole, Ti-phases and feldspars) also display complex spatial distributions that are controlled by fluid pathways as well as the precursor lithology. Textural relationships demonstrate syn-mineral stage alteration that extends significant distances from the main structures which host ore zones. These data reflect the chemical evolution of gold mineral systems, ultimately driven by changes in fluid chemistry, T and P.

## 1 Introduction

Late Archean orogenic gold deposits are known from five continents and represent one of the great epochs of gold metallogeny in Earth's history. The Yilgarn craton, one of the world's most well-endowed cratons, has a resource of >250 Moz of Au (Goldfarb et al. 2005) with approximately half of this resource occurring in the Kalgoorlie Terrane (Fig 1). Despite extensive work there is still debate about the source of gold and fluids, time and length scales of transport, nature and chemistry of the transport medium and mechanisms of precipitation for these systems (Phillips and Evans, 2004; Goldfarb et al., 2005; Large et al., 2007). Fluid–rock reactions are considered essential in forming world-class orogenic gold deposits, with precipitation of gold driven by physicochemical changes as the gold-bearing fluid equilibrates with the wall-rocks (Evans, 2010). Rocks with high Fe/(Fe+Mg) are seen as favorable reactants to destabilize gold–sulphide ligands (Evans, 2010), leading to coeval gold and sulphide deposition. However, this

model is not universal, as many deposits are hosted in rocks with low Fe/(Fe+Mg) ratios (Groves and Foster, 1991). Fluid immiscibility and the generation of two different fluid phases (e.g. boiling) has also been proposed as an effective depositional mechanism (Sibson, 1987). Separation of acid-generating volatiles (i.e. CO<sub>2</sub> and H<sub>2</sub>S) raises the pH of the residual fluid and promotes the deposition of native metal, carbonate and sulphide phases (Drummond and Ohmoto, 1985).

In addition to uncertainty around processes related to the transport and deposition of gold are the size of alteration footprints and critical fluid pathways. These systems are considered relatively difficult to explore due to the fact that alteration halos are considered cryptic and less well-developed compared with many other hydrothermal mineral deposits (Goldfarb et al. 2005). However technological advances allow new and novel approaches to mapping cryptic alteration patterns at a range of scales, delineating fluid pathways. To predict using minerals requires key data-sets on host-rock chemistry/lithology, geological framework (i.e., structure and lithological boundaries), paragenesis (textural data), and an understanding of how key styles of alteration relate to fluid chemistry (i.e. CO<sub>2</sub>-rich fluids, aH<sub>2</sub>S, temperature etc.). Here we provide examples of detailed

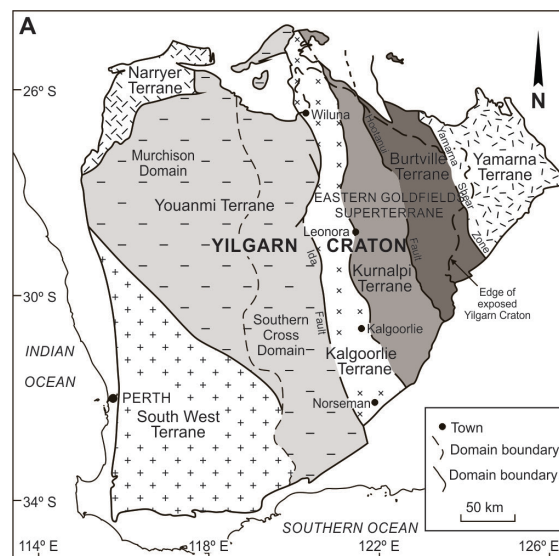


Figure 1. Map of the major terranes of the Yilgarn Craton.

mineral mapping at the camp- and deposit-scale from important Au camps (e.g., St Ives and Kundana) from Western Australia's Eastern Goldfields. In this paper we summarize some salient conclusions regarding

architecture (structural, lithological) controls on fluid-flow and mineralogical zoning in Late Archean Gold Systems of the eastern Yilgarn Craton.

## 2 Architectural controls: Terrane- to deposit-scale

Major Au camps of the Eastern Goldfields straddle late Archean, granite-cored domes and related architecture (Blewett et al. 2010, Davis et al. 2010). The domes are considered the first-order pathways for advection of lower crust/ mantle energy and volatiles into hydrothermal systems in the mid-upper crust. The impacts of dome architecture on fluid flow patterns were complex. Flat architectural elements of domes (extensional structures and basins, thrusts and associated stacked lithologies) commonly created regional-scale aquitards as well as aquifers. In contrast steeply dipping intrusive rocks within domes provided major sub-vertical pathways for advection of deep-seated crust/mantle fluids. Secondary porosity in albited porphyries (Bath et al. 2013) allow the possibility of significant fluid flow within steeply-dipping porphyry bodies, not just on the contacts.

*Faults as aquiclude*: Extant fluid-flow models for the formation of the St Ives camp consider the Repulse–Playa Fault as a major fluid pathway linked to the Boulder–Lefroy Fault System (Cox and Ruming 2004). The Boulder–Lefroy Fault System forms part of a crustal-scale fault architecture (Blewett et al. 2010) and gold camps such as St Ives ultimately reflect the fluid flux within this crustal architecture (Groves 1993, Hagemann and Cassidy 2000). However systematic S- and C-isotope mapping of reduced and oxidised assemblages within the Victory–Defiance complex (Neumayr et al., 2008) shows major changes in redox conditions across the Repulse and Britannia Shears (Fig 2). The most oxidised fluids (negative  $\delta^{34}\text{S}$  values in sulphides) were focused below the Repulse Shear and the most reduced fluids (positive  $\delta^{13}\text{C}$  values in carbonate) above the Britannia thrust. These patterns imply that Repulse and Britannia structures acted as aquiclude rather than aquifers, at least in the vicinity of the East Repulse deposit and on the eastern side of the Victory–Defiance complex. The seal above the East Repulse deposit appears to have a significant factor in the location of the mineralisation. Breaching of the seal led to mixing of  $\text{SO}_2\pm\text{HSO}_4^{1-}$  fluids with  $\text{CH}_4$ -rich fluids, creating a halo of strongly negative  $\delta^{13}\text{C}_{\text{carbonate}}$  values above the deposit.

The distribution of trace-elements (Mo, W, Bi), commonly associated with oxidised fluids, on the footwall of the Playa–Repulse Fault hints that the Repulse–Playa segment of the Boulder–Lefroy Fault System behaved as a district-scale aquiclude rather than as a major aquifer. The fault system possibly operated in tandem with talc–carbonate altered Kambalda Komatiite to separate domains of dominantly oxidised and reduced fluids. Based on the identification of a sub-vertical pathway of highly oxidised fluid, spatially associated with porphyries beneath the East Repulse deposit (Bath et al., 2013), it is suggested the NW–SE trending porphyry dikes across the Victory–Defiance complex provided the major sub-

vertical pathways for oxidised fluids, either within or on the contacts of the porphyries.

*Lithological aquiclude and aquifers*: Significant gold deposits occur in almost every rock type of the Kalgoorlie Terrane. The Golden Mile Deposit is hosted in dolerite, Wattle Dam in ultramafics, Athena and Hamlet (St Ives Gold Camp) in basalts, Invincible (St Ives Gold Camp) in Black Flag Beds, Wallaby in Late Basin conglomerates and the Kanowna Belle Au deposit in porphyries. This diversity of rock types hosting both high-grade and large-tonnage deposits strongly suggests that fluid–rock reactions are not the primary control on physicochemical changes driving gold deposition. Nonetheless, commonly observed but not unique associations with host rocks do occur, the most widely recognized being the association of mineralisation with Fe-rich dolerites. An alternate explanation is that it is the rheological properties of the rock that is the important factor. Rocks that are inherently strong and fail brittlely may act as either aquiclude or aquifers. There are a number of rock types in addition to Fe-rich dolerites, including the variole-rich middle Paringa Basalt (St Ives Camp) and the phenocryst-rich Victorious Basalt (Kundana Camp) that potentially acted as “strong beams” within the architecture, influencing fluid flow and ultimately deposit location. In the St Ives camp the Paringa basalt has been subdivided into Lower, Middle and Upper Paringa on the basis of the Cr/Ti ratio coupled with coherent map patterns (Walshe et al. 2014). The geochemical subdivision is supported by visual logging of textural characteristics. The Upper Paringa Basalt is fine grained and massive, the Middle Paringa Basalt is visually identified by abundant varioles. The Lower Paringa Basalt is also variolitic but to a lesser degree. The best gold shoots with the Athena and Hamlet shears are hosted by the Middle Paringa Basalt.

## 3 Alteration zonation of the East Repulse deposit

The Eastern Repulse deposit occurs within the Victory–Defiance Complex, Yilgarn Craton, Western Australia (approx. 60 km south of Kalgoorlie; Fig 1). Rocks consist of mafic to ultramafic volcanics of the Kambalda Sequence, which occur within an antiform that plunges gently towards the south (~2710–2690 Ma; Blewett et al., 2010). The Kambalda Sequence is intruded by intermediate to felsic intrusions, which commonly show ages of ca. 2670 and 2650 Ma; although younger and older age intrusions have also been documented (Fig 2; Nelson, 1997; Neumayr et al., 2008; Watchorn, 1998; Yeats et al., 1999). Rocks were metamorphosed to upper greenschist and lower amphibolite facies through four main deformation events between ca. 2700 and 2630 Ma (Swager, 1997). Gold mineralisation in the Kalgoorlie Terrane is thought to have occurred between ca. 2640 and 2630 Ma following peak metamorphism. Gold mineralisation within the East Repulse deposit occurs at a depth of about 250 meters below the present surface (Fig 2). Much of the mineralisation occurs along the shallowly-dipping Repulse thrust.

Three dominant stages of alteration have been

established relative to mineralisation at the East Repulse deposit (Bath et al., 2013). These include: (1) early-stage albite-carbonate-sulphates-magnetite  $\pm$  chlorite and/or epidote; (2) main-stage biotite-amphibole-anhydrite-carbonate  $\pm$  pyrite and gold; and (3) late-stage carbonate-albite-pyrite  $\pm$  chlorite and/or epidote alteration (Bath et al. 2013). These stages of alteration overprint komatiite, basalt, dolerite, metasediments and granitoids. Alteration assemblages of the East Repulse deposit have also been divided into domains that reflect the distribution of alteration assemblages from the footwall through to the hanging wall of the deposit (Bath et al. 2013). Main domains include upper, transitional, ore and lower and these zones are reflected in the sulphide-sulphate mineralogy (Fig. 2). The upper domain contains pyrite and pyrrhotite, as well as nickel sulphides (e.g., millerite, pentlandite and seigenite) and cobaltite. The transitional domain occurs above the ore-domain and contains bismuthinite and galena. The ore-domain is dominated by sulphides, but contains minor amounts of sulphate minerals. Sulphate occurs in the form of barite and celestine – anhydrite is less common. Sulphides in the form of pyrite, chalcopyrite, molybdenite, galena and rare bismuthinite. The lower domain contains sulphates (anhydrite, celestine and/or barite) and sulphides (pyrite, molybdenite, galena and chalcopyrite). These reflect a strong redox gradient between the hanging and footwall.

#### 4 Alteration zonation Kundana gold camp

The Kundana gold camp is located approximately 20 km west of Kalgoorlie along the Zuleika Shear Zone in the Kundana mining district (Fig. 1). The camp lies within the Coolgardie Domain of the Kalgoorlie Terrane (Swager, 1997). Mineralisation occurs along a main K2 lode centered on a shale unit that is bounded by plagioclase-phyric basalt (hanging-wall) and intermediate volcaniclastic units (footwall). The main high-grade K2 lode contains laminated or massive quartz veins. Free-gold occurs with scheelite, galena, sphalerite, pyrrhotite and pyrite along micro-fractures that cross-cut quartz veins. Surrounding wall rocks are variably mineralised and show evidence of weak to pervasive muscovite-albite-arsenopyrite-pyrrhotite alteration or biotite-andesine  $\pm$  anorthite  $\pm$  calcite alteration. Pervasive albite-calcite-dolomite-pyrrhotite  $\pm$  barite alteration occurs in the footwall and overprints intermediate volcanoclastics. Lower-grade mineralized lodes occur in the hanging wall of the deposit (K2A lodes). There K2A lodes cross-cut equigranular basalt and volcaniclastic units. K2A lodes show biotite-anorthite-calcite-arsenopyrite-scheelite-calcioancylite ( $\text{CaCe}(\text{CO}_3)_2(\text{OH})(\text{H}_2\text{O})$ )  $\pm$  muscovite (often quartz-undersaturated rock matrix) alteration with peripheral albited domains, which are enriched in ullmannite ( $\text{NiSbS}$ ). Cobaltite ( $\text{CoAsS}$ ) enrichment domains also form halos around main K2 lode and K2A lodes. These patterns reflect chemical gradients and predictable mineral zonation patterns around gold lodes.

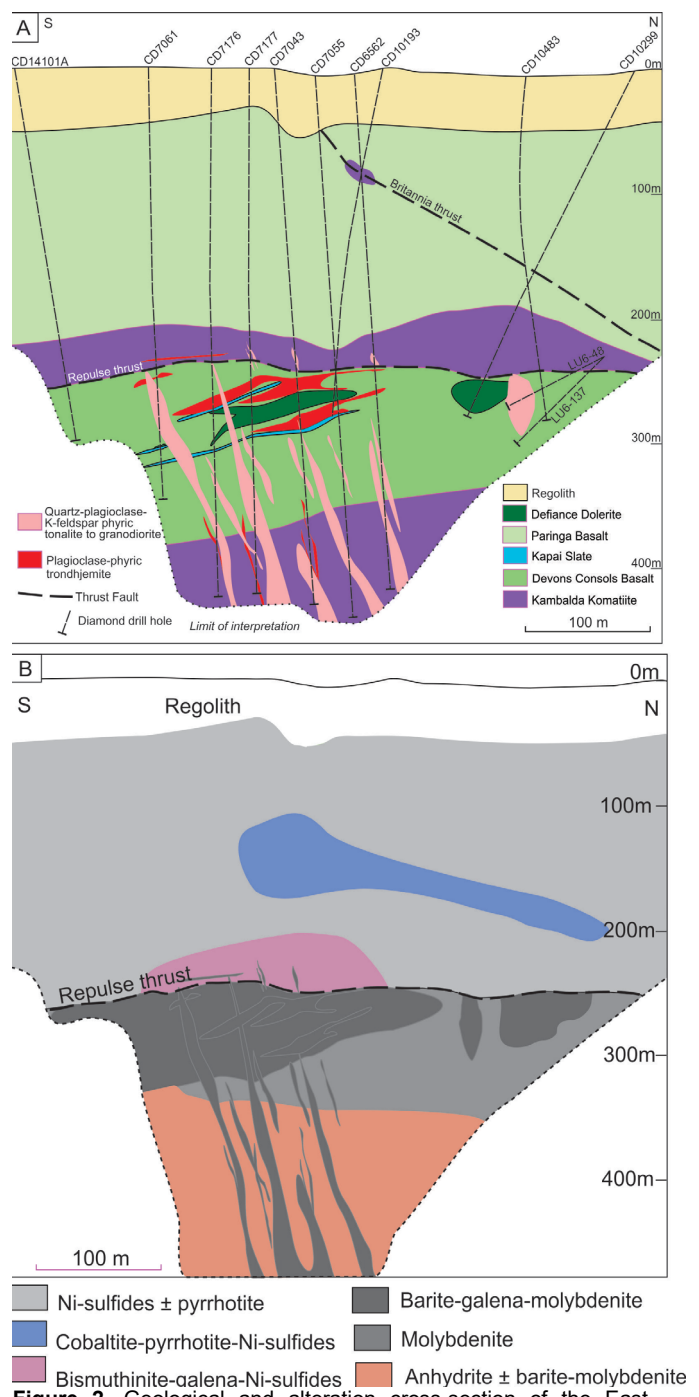


**Figure 2.** Geological and alteration cross-section of the East Repulse gold deposit from the >12 Moz St Ives gold camp.

High-grade areas of the main K2 lode are associated with deeper domains of biotite-andesine  $\pm$  anorthite  $\pm$  calcite alteration of wall rocks, whereas shallower lower grade zones to the east are associated with muscovite-albite altered graphitic-rich sediments. These assemblages reflect the presence of more acidic fluids with lower-grade muscovite alteration ( $\text{pH} < 4.3$ ) relatively to high-grade biotite-calcite ( $\text{pH} > 4.3$ ) assemblages. The presence of anhydrite and barite in footwall albite-rich alteration assemblages are calculated to form at  $\text{pH} > 6.5$  at conditions above the  $\text{CO}_2 - \text{CH}_4$  buffer, indicating a switch to alkaline conditions in the footwall (i.e. neutral pH

$\approx 5.5$  at  $400^{\circ}\text{C}$ ). Auriferous fluids may have been alkaline. Fluid-mixing between reduced water-rich acid and  $\text{CO}_2$ -rich relatively alkaline fluids at the time of mineralisation may have played an important role in destabilising  $\text{Au}(\text{HS})_2^-$  complexes at the time high-grade gold was deposited.

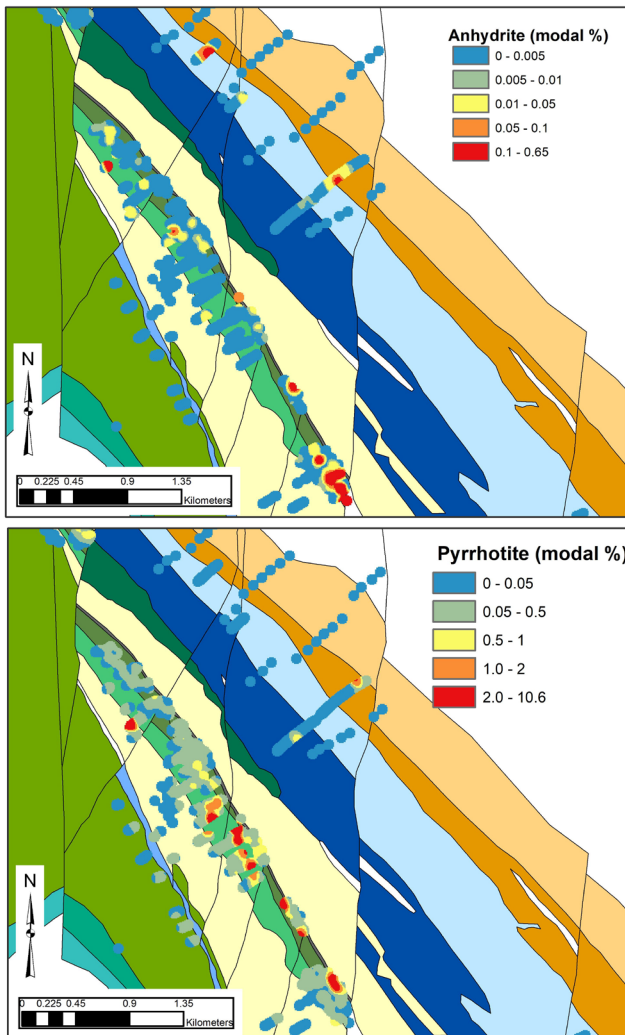


**Figure 3.** Distribution of anhydrite and pyrrhotite along the K2 mineralised zone from the >8 Moz Kundana gold camp. Much of the mineralization occurs with pyrrhotite where sediments (yellow, blue and orange) form contacts with mafic volcanics or intrusives (green).

## 5 Conclusions

Mineralisation in camps from the World class Kalgoorlie Terrane are hosted along the contact between impermeable or weakly permeable talc-rich ultramafic and thick coherent phenocryst-rich mafic volcanics and permeable albite altered rocks in the footwall. Footwall domains contain broad ( $>100\text{m}$ ) alteration zones with minerals, such as anhydrite, mapped and linked to mineralisation. Footwall pyrite-anhydrite domains transition into pyrrhotite-domains into mineralised zones,

indicating chemical redox gradients. Other chemical gradients such  $f\text{CO}_2$ ,  $a\text{H}_2\text{O}$  and pH likely also played a role in the deposition of gold in these key zones.

## References

- Bath, A. B., J. L. Walshe, J. Cloutier, M. Verrall, J. S. Cleverley, M. I. Pownceby, C. M. Macrae, N. C. Wilson, J. Tunjic and G. Nortje (2013). "Biotite and apatite as tools for tracking pathways of oxidized fluids in the Archean East Repulse gold deposit." *Economic Geology* 108(4): 667-690.
- Blewett, R. S., P. A. Henson, I. G. Roy, D. C. Champion and K. F. Cassidy (2010). "Scale-integrated architecture of a world-class gold mineral system: The Archean eastern Yilgarn Craton, Western Australia." *Precambrian Research* 183(2): 230-250.
- Blewett, R. S., R. Squire, J. M. Miller, P. A. Henson and D. C. Champion (2010). "Architecture and geodynamic evolution of the St Ives Goldfield, eastern Yilgarn Craton, Western Australia." *Precambrian Research* 183(2): 275-291.
- Cox, S. F. and K. Ruming (2004). "The St. Ives mesothermal gold system, Western Australia - a case of golden aftershocks?" *Journal of Structural Geology* 26: 1109-1125.
- Czarnota, K., D. C. Champion, B. Goscombe, R. S. Blewett, K. F. Cassidy, P. A. Henson, and P. B. Groenewald, 2010, Geodynamics of the eastern Yilgarn Craton: *Precambrian Research*, v. 183, p. 175-202.
- Davis, B. K., R. S. Blewett, R. Squire, D. C. Champion and P. A. Henson (2010). "Granite-cored domes and gold mineralisation: Architectural and geodynamic controls around the Archean Scotia-Kanowna Dome, Kalgoorlie Terrane, Western Australia." *Precambrian Research* 183(2): 316-337.
- Drummond, S. E., and H. Ohmoto, 1985, Chemical evolution and mineral deposition in boiling hydrothermal systems: *Economic Geology*, v. 80, p. 126-147.
- Evans, K. A., 2010, A test of the viability of fluid-wall rock interaction mechanisms for changes in opaque phase assemblage in metasedimentary rocks in the Kambalda-St. Ives goldfield, Western Australia: *Mineralium Deposita*, v. 45, p. 207-213.
- Goldfarb, R. J., T. Baker, B. Dube, D. I. Groves, C. J. R. Hart, and P. Gosselin, 2005, Distribution, character and genesis of gold deposits in metamorphic terranes: *Economic Geology*, 100th Anniversary Volume, p. p. 407-450.
- Groves, D. I. (1993). "The crustal continuum model for late Archean lode-gold deposits of the Yilgarn Block, Western Australia." *Mineralium Deposita* 28: 366-374.
- Hagemann, S. G. and K. F. Cassidy (2000). "Archean orogenic gold deposits." *Reviews in Economic Geology* 13: 9-68.
- Large, R. R., V. V. Maslennikov, F. Robert, L. V. Danyushevsky, and Z. Chang, 2007, Multistage Sedimentary and Metamorphic Origin of Pyrite and Gold in the Giant Sukhoi Log Deposit, Lena Gold Province, Russia: *Economic Geology*, v. 102, p. 1233-1267.
- Neumayr, P., J. L. Walshe, S. G. Hagemann, K. Petersen, R. Roache, P. Frikken, L. Horn and S. Halley (2008). "Oxidized and reduced mineral assemblages in greenstone belt rocks of the St. Ives gold camp, Western Australia: vectors to high-grade ore bodies in Archean gold deposits?" *Mineralium Deposita* 43: 363-371.
- Phillips, G. N., and K. A. Evans, 2004, Role of  $\text{CO}_2$  in the formation of gold deposits: *Nature*, v. 429, p. 860 - 863.
- Sibson, R. H., 1987, Earthquake rupturing as a mineralizing agent in hydrothermal systems: *Geology*, v. 16, p. 551-555.
- Walshe, J. L., J. Cloutier, A. B. Bath and R. M. Hough (2014). Chemical gradients and pathways to mineralisation Argo-Apollo-Hamlet-York corridor, St Ives Gold Field, Yilgarn Craton, Western Australia High grade Au deposits:processes to prediction J. L. Walshe, J. Cloutier, A. B. Bath and R. M. Hough. Perth, Geological Survey Western Australia. Report 145: 7-28.

# Critical mineral systems under cover: insights from magnetic, gravity, and magnetotelluric 3D inversion models, Southern Midcontinent, USA

A.E. McCafferty, P.A. Bedrosian, J.D. Phillips

U.S. Geological Survey, Geology, Geophysics, and Geochemistry Science Center, Denver, USA

**Abstract.** 3D inversion models of magnetic, gravity, and magnetotelluric (MT) data reveal evidence for concealed critical metal mineral systems at regional scales in the US southern Midcontinent. The region contains several igneous-related critical-element-bearing ore deposits of different types and ages that have been sourced from ore-forming fluids originating from the upper mantle to shallow crustal levels. These include the Mesoproterozoic IOCG-Co and IOA-REE deposits, which are part of the southeast Missouri iron metallogenic province. A depth slice along the top of the mantle from the 3D models reveals feeder zones that allowed development of large ca 1.4 Ga magmatic systems that host mineralization in the upper crust. Shallow crust to upper mantle conductivity sources dip under the iron province and may reflect a potential sulfur source for IOCG mineralization. Our findings indicate that the iron deposits show an unambiguous connection at depth by means of an inferred magmatic system that is traceable to the mantle and that different IOA, IOA±REE and IOCG deposits may be located in distinct parts of the same magmatic system. Several trans-crustal to trans-lithospheric magmatic plumbing systems are revealed and show how the Mesoproterozoic architecture may have influenced subsequent carbonatite and peralkaline igneous activity.

## 1 Introduction

Gravity, magnetic, and magnetotelluric data covering a large part of the US Midcontinent were inverted to 3D models of density, magnetic susceptibility, and electrical resistivity (Fig. 1). Regional- to continental-scale coverages such as these are required to adequately map and model the overall crustal architecture underlying large mineral provinces.

The mining community, along with federal governments and academia, has shown an increasing interest in large-scale geophysical data sets and their utility in exploration. A few examples include Laurentian University's Metal Earth Project, Australia's UNCOVER initiative, and the recently announced U.S. Geological Survey's Earth Mapping Resource Initiative (Earth MRI) (Day 2019). The growing interest is driven, in large part, by a global shift to improve resource exploration undercover and identify large regions for further study.

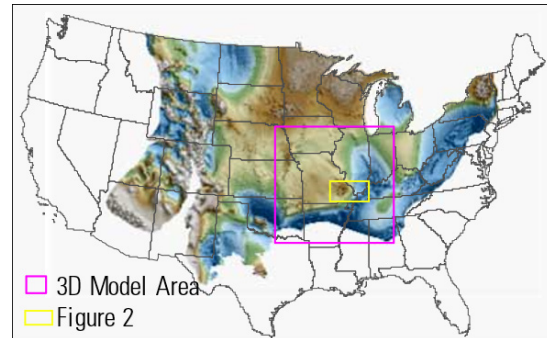


**Fig. 1** 3D model area and location of mineral deposits in Fig. 2. Base shows Precambrian topography (Marshak et al., 2016).

### 1.1 Purpose and Scope

The purpose of this study is to leverage existing regional-scale gravity, magnetic, and magnetotelluric data to create physical property models of the crust below the southern Midcontinent of the US. The integration of the 3D models with isotopic and geologic constraints allows for a more robust interpretation of the anatomy of the crust and provides important guidance in defining prospective regions for critical mineral-bearing deposits over a large, under explored region in the US.

## 2 Geological Setting

The Precambrian crystalline basement in the southern Midcontinent of the US is only partly exposed in the St. Francois Mountains of southeast Missouri (Fig. 2). The majority is concealed and known only through sparse drill hole data and geophysical map interpretation. The basement consists of a collage of metamorphic and igneous rocks that formed between ca 1.8 to ca 1.1 Ga (Lund et al. 2015 and references therein), either through accretionary processes or intraplate magmatism, along the southern margin of the Laurentia continent. Major geologic provinces that form the Precambrian basement in our model area include the ca 1.8 to 1.63 Ga Central Plains orogeny; the ca 1.45 Ga Eastern Granite Rhyolite Province and the ca 1.35 Ga Southern Granite Rhyolite Province.

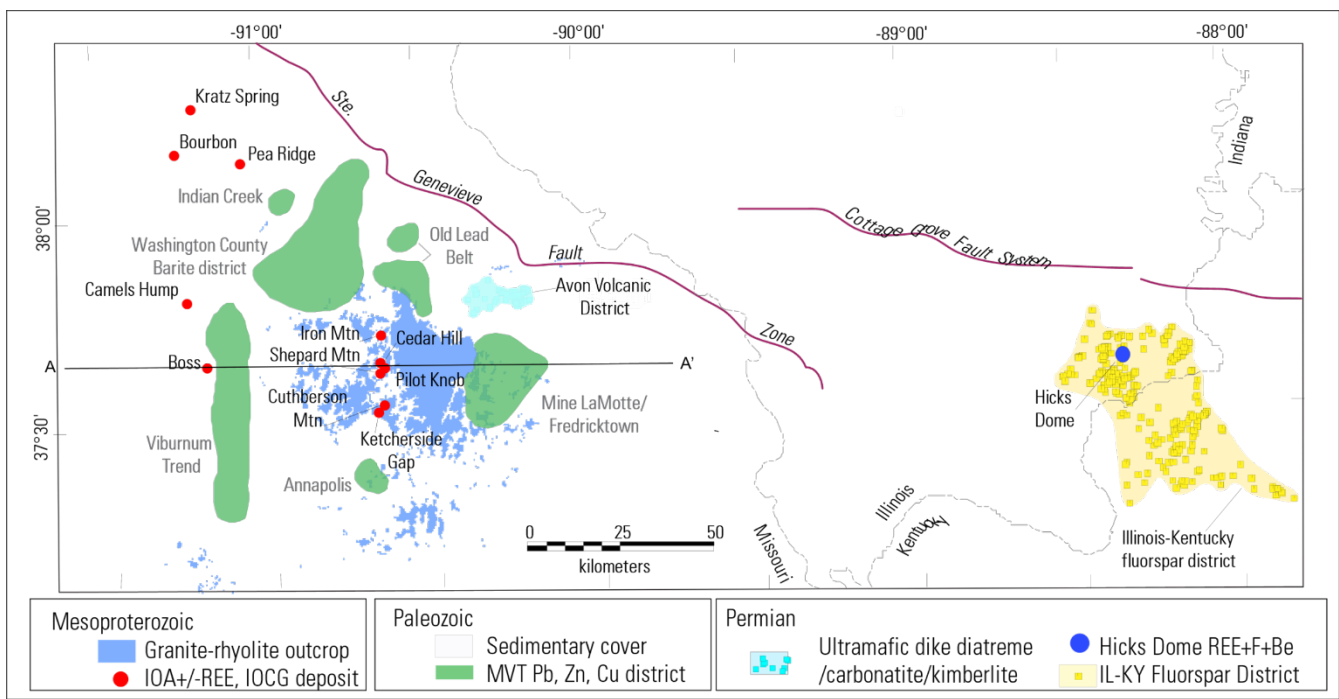


**Fig. 2 General geology and mineral deposits. Interpreted section along A-A' is shown in Fig. 3.**

## 2.1 Mineral Resources

The Mesoproterozoic iron metallogenic province in southeast Missouri (Kisvarsanyi and Proctor 1967) occurs within a 35- by 115-km region and is comprised of several iron, copper, cobalt, manganese, and rare-earth element deposits and prospects (Fig. 2), including one iron oxide-copper gold (IOCG) deposit and seven known iron oxide-apatite ± rare earth element (IOA ± REE) deposits (Nold et al. 2014). The deposits are hosted in 1.48 to 1.44 Ga high-silica rhyolites and intermediate to mafic-composition volcanic rocks. Most of the known deposits are located within or near Precambrian outcrops in the St. Francois Mountains. To date, no mineralization has been discovered in the contemporaneous ca 1.46 Ga granitoids or in the younger (ca 1.35 Ga) assemblage of two-mica granites and minor mafic intrusions that intrude the older Mesoproterozoic igneous rocks.

In addition to the mineral potential associated with the Mesoproterozoic IOA/IOCG deposits, other geologic terranes in the southern Midcontinent have a high potential for several valuable critical mineral and base metal commodities. The USGS has identified 35 critical minerals that either have important technological uses or are an import supply risk for the United States (Schultz et al. 2017; Fortier et al. 2018). Critical mineral commodities or commodity groups that are known to occur within our study area include aluminum, barite, beryllium, cobalt, fluorspar, gallium, germanium, manganese, niobium, rare-earth elements, titanium, and vanadium. Base and precious metal commodities present in various deposit types include copper, lead, zinc, and gold.

Critical mineral, base-, and precious-metal mineral commodities occur in various deposit types across a range of geologic terranes in the basement and in the

overlying sedimentary section. Igneous deposit types include the southeast Missouri IOA+REE and IOCG+Co deposits; the Nb-REE-bearing carbonatite at Elk Creek, Nebraska; and a peralkaline intrusion complex with HREE-enriched fluorspar mineralization at Hicks Dome, Illinois. Sedimentary-hosted MVT Co, F, Ge, and Ba deposits are also present. A goal of our study is to evaluate how these various mineral systems might relate.

## 3 Data and Models

National-scale potential field databases of magnetic and gravity data (Phillips et al. 1993; Ravat et al. 2009) were inverted to 3D models of density and magnetic susceptibility, respectively. National-scale EarthScope magnetotelluric data, supplemented with stations collected by the USGS, which provided an increased site density, were used to construct the 3D resistivity model.

Model constraints were provided by a database of Precambrian basement topographic elevations (Marshak et al., 2016) and a database of continental crust thickness (Shen and Ritzwoller 2016). The surfaces define the top and bottom elevations of the potential field inversion models and are especially important given the extreme structural relief in some parts of the Precambrian basement. The crustal thickness data are derived from inversion of USAarray/Transportable Array seismic measurements from the EarthScope initiative and provide estimates related to variations in the depth to the Moho relative to the topographic surface.

A west to east vertical section was extracted through the magnetic susceptibility and density models (A-A' in Fig. 2) along a profile that includes several iron deposits located in the St. Francois Mountains and major geologic features. An interpretation was produced that combined the density and susceptibility properties across the section (Fig. 3). Map sections from the 3D density and magnetic susceptibility models of the deep crust were

develop moderate to high susceptibility apophyses that envelope both the ca 1.4 Ga caldera structures and ca 1.3 Ga plutons at mid to shallow depths. We assume that areas where the high susceptibility column is also dense, larger volumes of mafic rock are present in the crust that were part of the IOA/IOCG ore-forming system.

The distinct nonmagnetic masses under the ca 1.3 Ga Graniteville and Buick granitic plutons extend to

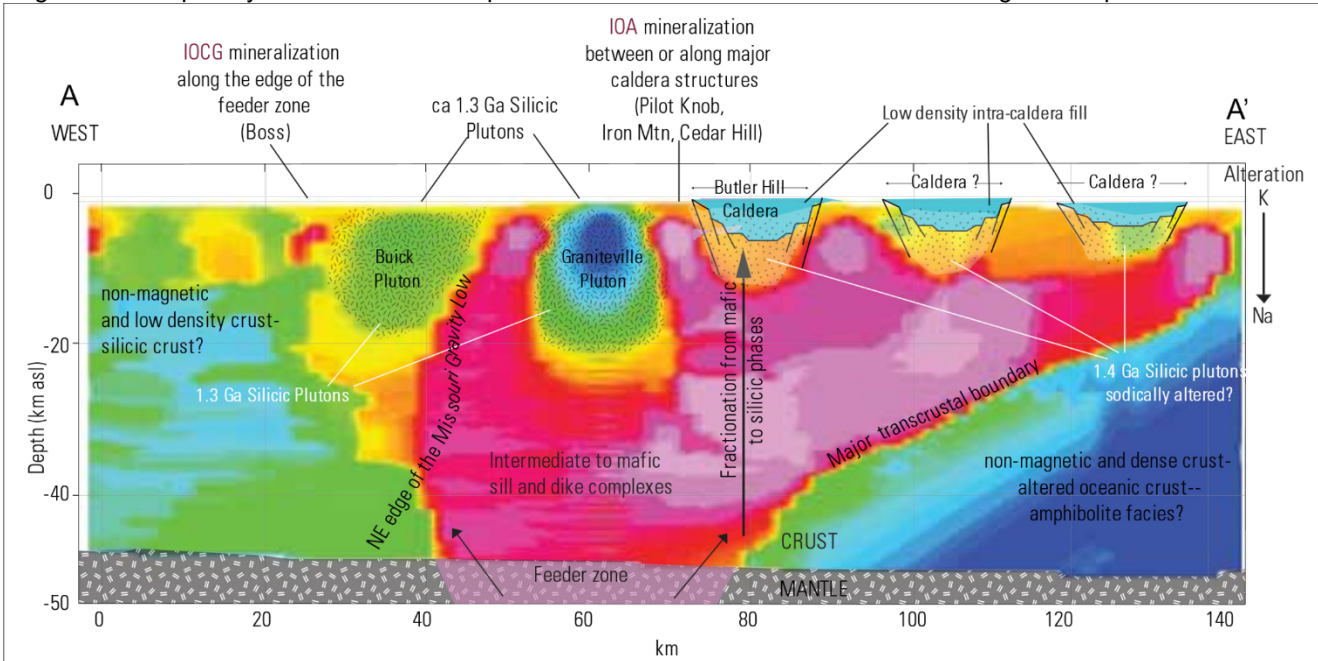


**Fig. 3 Schematic section showing IOA/IOCG mineral system under southeast Missouri iron metallogenic province from an integration of magnetic susceptibility and density 3D inversion models.**

generated by extracting voxels along an irregular surface just above the Moho surface (Figs. 4a,b). Depths to this surface range from 34 to 42 km-equivalent to the variable thickness of crust across the study. A depth slice of crustal resistivity was extracted at 27 km from the 3D resistivity model (Fig. 4c).

#### 4 Results

The mineral system below IOA/IOCG deposits is visualized on a schematic cross section that transects the major iron deposits (Fig. 3) and depicts a regional crustal framework that highlights important physical property manifestations related to the formation of the deposits. The susceptibility inversion section is used as a backdrop but the illustration incorporates important information from the density inversion, geology and geochronology of the St. Francois Mountains and a model for the genesis of the iron deposits.

Our findings suggest that the iron deposits in southeast Missouri, with no obvious connection at the surface, are part of one large magmatic system at depth (Fig. 3). At deep crustal levels, the section along A-A' shows the crust beneath the iron province contains broad (up to 75 km-wide) column of high magnetic susceptibility material, which serves to anchor the upper caldera-forming parts of the crust to the mantle. The magnetic column splayes up and outward from the mantle and through the crust to

somewhat greater depths and yield lower susceptibilities compared to that observed under the older Butler Hill caldera (Fig. 3). The model results are consistent with magnetic susceptibility measurements on hand and drill core samples that show the ca 1.3 plutons have the lowest magnetic susceptibilities compared to the older granites. While not conclusive, the lower susceptibility to greater depths indicated on the magnetic susceptibility inversion model, may help to distinguish younger plutons from older caldera structures in concealed parts of the Precambrian basement. Differentiating these two features may aid targeting of favorable exploration areas for IOA/IOCG deposits. Similar trans-crustal boundaries such as those present in Fig. 3 are also imaged near the Hicks Dome peralkaline complex (Fig. 2), which suggests Hicks Dome may be located along a reactivated Mesoproterozoic structure.

The nature of the lower crust across the southern Midcontinent is revealed in the susceptibility and density depth slices (Figs. 4a,b). Results show that the iron deposits formed above a magmatic system that extends over 170 km within a 40 to 50 km-wide elongate-track of high magnetization/moderately dense rocks that trends northwesterly. The IOA deposits sit directly over the high magnetization track while the Boss IOCG and the Camel's Hump IOA(?) deposits sit within 30 km of the central axis of the base of the proposed magmatic system. Other similar magnetic tracks along the top of the mantle are interpreted to represent the base of other

prospective regions for iron mineralization.

Inversion of long-period magnetotelluric data to electrical resistivity, provides a third physical property that informs changes in the deep crust related to the tectonic and magmatic history across the southern Midcontinent.

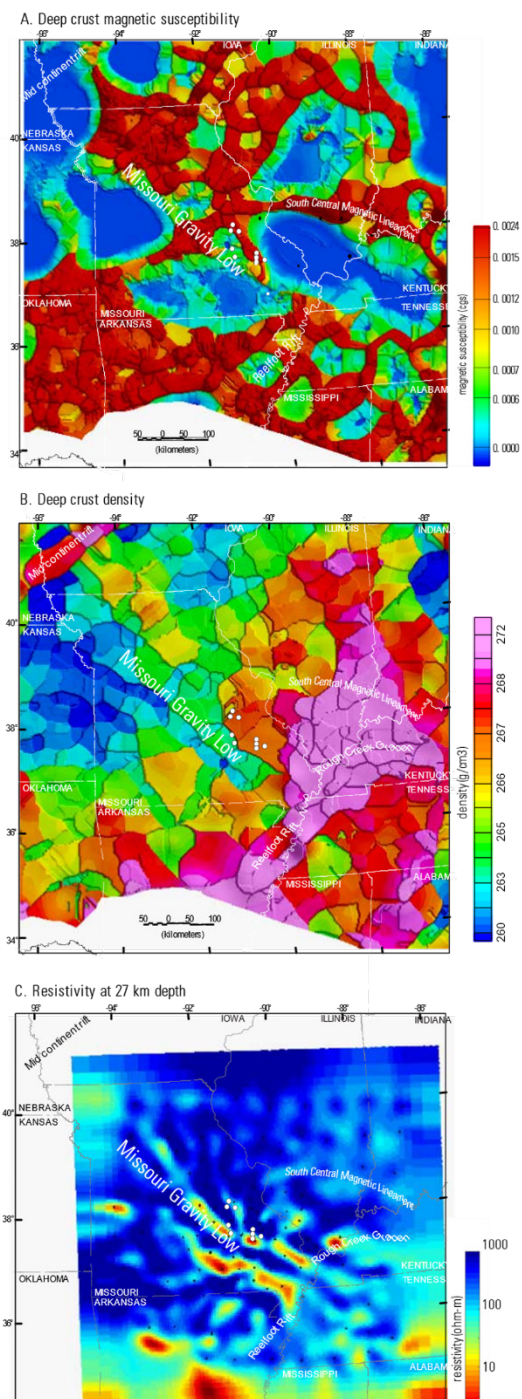


**Fig.4 (A) Magnetic susceptibility of the deep crust; (B) density of the deep crust and (C) resistivity at 27 km depth.**

An enhanced conductivity anomaly, calculated from EarthScope magnetotelluric data, coincides with the

northwest-trending Missouri Gravity Low (DeLucia et al. 2019). Major and minor IOA and IOCG deposits are located along the northeast edge of the anomaly. Shorter period magnetotelluric data used in this report show two parallel tracts of high conductivity exist at mid crust to mantle depths (Fig. 4c). A permissive source for the high conductivity may be older metasedimentary rock that underlies the more extensive granite and rhyolite. A metasedimentary package could be a potential source for sulfide mineralization in the iron deposits.

## Acknowledgements

This work was supported by the U.S. Geological Survey Mineral Resource Program.

## References

- Day W (2019) The earth mapping resources initiative (Earth MRI): Mapping the nation's critical mineral resources: US Geol Surv Fact Sheet 2019-3007, doi:10.3133/fs20193007
- De Lucia M Marshak S Murphy B Egbert G (2019) The Missouri high-conductivity belt, revealed by magnetotelluric imaging: Evidence of a trans-lithospheric shear zone beneath the Ozark Plateau, Midcontinent USA?: J. Tecto, doi:10.1016/j.tecto.2019.01.011
- Fortier S Nassar N Lederer G Brainard J Gambogi J McCullough E (2018) Draft critical mineral list—Summary of methodology and background information—U.S. Geological Survey technical input document in response to Secretarial Order No. 3359: US Geol Surv Open-File Rep 2018-1021, doi:10.3133/ofr20181021
- Kisvaranyi G Proctor P (1967) Trace element content of magnetites and hematites, southeast Missouri metallogenic province, U.S.A.: Econ Geol 62:449–471
- Lund, K Box S Holm-Denoma C San Juan C Blakely R Saltus R Anderson E DeWitt E (2015) Basement domain map of the conterminous United States and Alaska: US Geol Surv Data Ser 898:41, doi:10.3133/ds898
- Marshak S Domrois S Abert C Larson T (2016) DEM of the great unconformity, USA cratonic platform: Univ of Illinois at Urbana-Champaign, doi:10.13012/B2IDB-546972\_V1
- Nold J Dudley M Davidson P (2014) The southeast Missouri (USA) Proterozoic iron metallogenic province—types of deposits and genetic relationships to magnetite-apatite and iron oxide-copper-gold deposits: Ore Geo Rev 57:154–171
- Phillips J Duval J Ambroziak R (1993) National geophysical data grids; gamma-ray, gravity, magnetic, and topographic data for the conterminous United States: US Geol Surv Data Series DS-09
- Ravat D Finn C Hill P Kucks R Phillips J Blakely R Bouligand C Sabaka T Elshayat, Aref A Elawadi E (2009) A preliminary, full spectrum, magnetic anomaly grid of the United States with improved long wavelengths for studying continental dynamics—A website for distribution of data: US Geol Surv Open File Report 2009-1258
- Schulz, K DeYoung J Seal R Bradley D eds., (2017) Critical mineral resources of the United States—Economic and environmental geology and prospects for future supply: US Geol Surv Prof Paper 1802:797, doi:10.3133/pp1802.
- Shen W Ritzwoller MH (2016) Crustal and uppermost mantle structure beneath the United States, J. Geophys. Res. Solid Earth, doi:10.1002/2016JB012887

# Automated facies classification and gold grade prediction using machine learning algorithms

Glen T. Nwaila, Steven E. Zhang

School of Geosciences, University of the Witwatersrand, South Africa

Hartwig E. Frimmel

Bavarian Georesources Centre, Institute of Geography and Geology, University of Würzburg, Germany

**Abstract.** Point-wise gold grade data are commonly used to guide exploration and resource estimation with the application of spatial interpolation techniques such as kriging. The application of kriging is not optimal where high nugget thresholds exist, such as the gold deposits in the Witwatersrand Basin of South Africa. To reduce the impact of subjective grade interpolation and geological interpretation, as well as to exploit currently unused geological descriptions, we present a novel machine learning-based algorithm called GS-Pred. It combines both sedimentological and gold assay data for point-wise gold grade prediction and automated facies identification in a conglomerate-hosted gold deposit. For this application, GS-Pred requires an input database of sedimentological descriptions, spatial information and gold grades, and makes predictions of gold grades at any point within the spatial coverage of the input database, provided that it has appropriate sedimentological descriptions. This novel machine-learning algorithm is entirely data-driven. We have shown its successful application in a complex geological setting of the Witwatersrand basin.

## 1 Introduction

Conglomerate-hosted gold deposits in the Witwatersrand Supergroup (South Africa) include the largest palaeoplacer deposits known in the world. Although their genesis is still debated, a present-day understanding suggests a synsedimentary gold concentration with post-depositional hydrothermal remobilisation of some of the gold particles over short, economically insignificant, distances (Frimmel 2018). A significant amount of high-dimensionality (i.e. more than 10 attributes) sedimentological and metal grade data has been accumulated for most of the time these deposits have been mined (over a century) from various Witwatersrand goldfields. Qualitative relationships between the sedimentology and the gold grade in the Witwatersrand Supergroup have long been recognised through the daily practice of core-logging, underground mapping and sampling (Nami and Verrezen 1986), but these relationships exhibit spatial variability and can be complex. The evolution and adoption of computer technology and machine learning in resource exploration and exploitation has made this data more meaningful and contextually relevant. Techniques using machine-learning algorithms are well-suited for high-dimensionality data, complex processes and spatially-

dispersed data (Kanevski et al. 2009).

Here we introduce a set of algorithms to predict gold grade and perform facies identification called GS-Pred, which uses geological descriptions and gold assay data. GS-Pred consists of data pre-processing, weighted and spatially-localised linear regressions, and cluster analysis. GS-Pred infers unknown metal grades at points that are within the vicinity of previously sampled areas and in its present form requires knowledge of the deposits on a mine- and regional-scale. Compared to the standard approach of chemical assays, GS-Pred is less accurate but rapid and highly automatable. This makes GS-Pred a viable tool for mine production, planning and target exploration.

We evaluate the performance of GS-Pred on a test dataset consisting of sedimentological and gold grade data from the Witwatersrand Basin of South Africa. In particular, we compare our regression algorithm to the elastic net, K-nearest neighbours, non-linear support vector regression and ordinary kriging. We show that our algorithm is generally more accurate over the test dataset and that under similar circumstances, the machine learning algorithms are more capable than traditional geostatistical methods. In addition, we show that a simple mixture of kriging and machine learning predictions enhances the prediction performance.

## 2 Machine learning, geostatistics and geologic background

### 2.1 Machine learning and geostatistics

Machine-learning algorithms are applied by computers on data to recognise patterns using automated mathematical induction. They are highly successful in geosciences and closely-related fields (e.g. Melo et al. 2017). In this paper, we explore several multivariate regression algorithms including LRPCC, non-linear support vector regression (SVR) with a radial basis function kernel, non-parametric regression, K-nearest neighbours (KNN) and penalised linear regression in the form of elastic net regression with cross-validation ("ElasticNetCV"). The unique parameters in each method can be determined through cross-validation testing. In addition, we use the K-means clustering algorithm to identify rock facies using sedimentological descriptions. Kriging is a progressive interpolation method using a spatial model for point-wise estimations of a regionalised variable. It is a popular technique in the geosciences, such as in ore and natural

resource evaluations (e.g. Goovaerts 1997).

## 2.2 Geologic background

The Witwatersrand Supergroup, located near the centre of the Kaapvaal Craton (South Africa), is one of the best preserved Mesoarchaean sediment archives that records the development of a cratonic sedimentary basin in a tectono-sedimentary environment (Fig. 1). It is known to cover an area that stretches for about 350 km in a northeasterly, and about 200 km in a northwesterly, direction and is the largest known gold province in the world. The Witwatersrand Supergroup has been subdivided into the lower gold-poor West Rand Group (2.99–2.91 Ga) and the upper gold- (and uranium-) rich Central Rand Group (2.90–2.79 Ga; Kositcin and Krapež 2004).

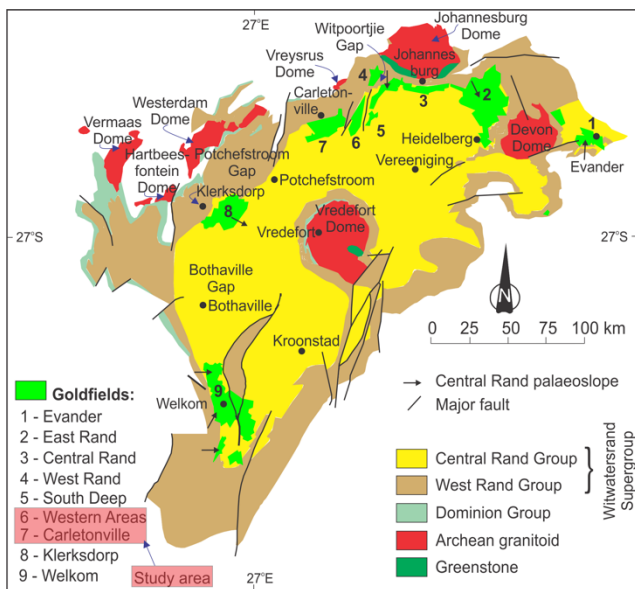


**Figure 1.** Simplified surface and sub-surface geological map of the Witwatersrand Basin, also showing the distribution of Archaean granitoid domes, the location of the study area and major faults (Frimmel and Minter 2002).

## 3 Material and methods

### 3.1 Data

Rocks of the Witwatersrand Supergroup are best studied in underground mine exposures and drill cores. We collected 1964 samples (Fig. 2) comprising sedimentological data and gold assays that have been declared as qualified for resource and reserve estimations from published industry reports and dissertations that focused on the West Rand goldfields.

The information contained in the datasets are sample coordinates ( $x$ ,  $y$ ,  $z$ ); conglomerate thickness (CW); volume percentage of conglomerate; quartz/chert pebble size; pebble packing; pebble roundness and sorting; % pyrite; the colour of the conglomerate matrix; the type of the conglomerate basal contact. This dataset covers an area of about 46 km<sup>2</sup>.

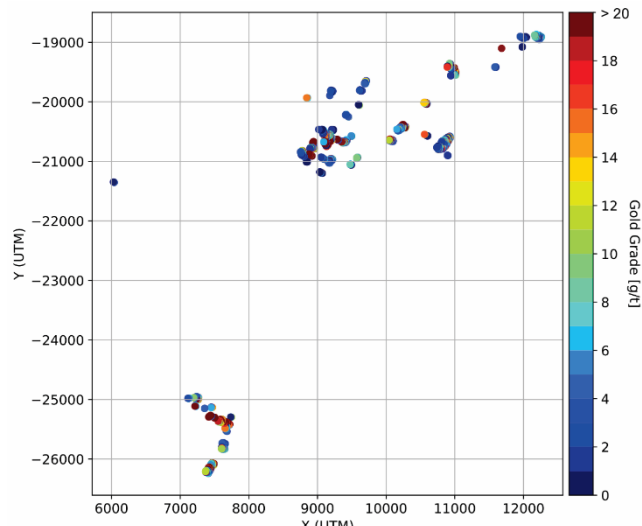


**Figure 2.** A 2D visualisation of the spatial distribution of samples and gold grades (g/t) in the study area.

### 3.2 Development of the prediction model

The mean gold grade in the dataset is 14.91 g/t with a standard deviation of 45.62 g/t. Within the dataset are samples with 0 g/t (the detection limit is 0.001 g/t) and high gold grade (e.g. 1402 g/t). Data below the 2nd percentile (about 2 % of the data) was removed as outliers. The gold grade is approximately log-normally distributed. Normalisation is unnecessary for machine learning algorithms in general, but is necessary for many geostatistical techniques. GS-Pred normalises the gold grade data using a three-parameter log-transformation with an additional small positive constant,  $\beta$ , that is added to the gold grade to minimise the D'Agostino's K-squared omnibus test results (D'Agostino and Pearson 1973). The transformation for the gold grades can be written as

$$\Gamma = \ln(Au[g/t] + \beta), \quad \text{Eq. 1}$$

where  $Au$  [g/t] are gold grades in grams per ton and  $\Gamma$  are log-transformed gold grades.

The test statistics of the D'Agostino's K-squared, Anderson-Darling and Shapiro-Wilks tests on the untransformed gold grade data are 1246.11, 102.88 and 0.75 respectively. After the transformation, the mean is 1.97 and the standard deviation is 1.18. The test statistics of the D'Agostino's K-squared, Anderson-Darling and Shapiro-Wilks tests are 18.24, 2.49 and 0.99, respectively. GS-Pred also maps the sedimentological descriptions into numeric feature labels (e.g. shades of colours into a sequence of integers) that are suitable for regression algorithms.

GS-Pred includes four main steps: (1) an automated semi-variance modelling routine that incorporates the spherical model to determine the range and sill within the dataset; (2) a linear regression and Pearson correlation-based prediction algorithm that predicts metal grades with sedimentological features using training data localised within an Euclidean neighbourhood based on the range (LRPCC); (3) a K-means clustering analysis on the sedimentological features of the entire dataset to

automatically identify rock facies; (4) leave-one-out cross-validation testing and facies-specific prediction performance evaluation.

In LRPCC, feature weighting and training occurs on a per-target basis. For each target, the algorithm can be written as:

$$Y = \sum_i f(\Gamma, \omega_i) \cdot \left( \begin{cases} \rho_i^2 / \sum_j \rho_j^2, \rho_i^2 \geq c \\ 0, \rho_i^2 < c \end{cases} \right) \quad \text{Eq. 2}$$

where each feature (" $i$ ") is used in a univariate linear regression to make a prediction  $Y_i \approx f(\Gamma, \omega_i)$ , where  $\Gamma$  is a set of known labels (e.g. metal grades). The output is normalised by the sum of the squares of the Pearson correlation coefficients (" $\rho_i^2$ ") between all features and the labels  $\Gamma$ .  $\bar{Y}_i = Y_i \cdot \rho_i^2 / \sum_j \rho_j^2$ . The algorithm output is

the sum of all feature's contributions,  $Y = \sum_i \bar{Y}_i$ . A small positive threshold parameter  $0 \leq c < 1$  can mute features that are poorly correlated with the metal grade per prediction target (where  $\rho_i^2 < c$ ). Fixing all other algorithms in GS-Pred, LRPCC is compared with ElasticNetCV, SVR and KNN algorithms to assess its prediction performance. The parameter  $c$  in LRPCC can range between 0 and 1. For all other regression methods, the parameters are determined through cross-validation, and for the elastic net method, on a per-target basis. Prediction performance is evaluated through the mean and median of the absolute value of the relative errors (MRE and MER). For the K-means cluster analysis, feature rescaling was applied to ensure that each feature spans an identical range.

## 4 Results

From the automated semi-variogram modelling, the correlation range in the test dataset is about 14 m; the nugget threshold is 0.54 and the sill 0.87. Cross-validation testing during feature selection reveals that sedimentology and CW consistently produces lower MREs. This combination is used for all subsequent evaluations. For the parameter  $c$ , higher values result in lower prediction errors at the expense of the predictable fraction of samples. For comparison purposes, we adopt  $c=0.1$ , which does not decrease the predictable fraction noticeably (average relative loss of roughly 3 %).

The best kriging results obtained by cross-validation testing features an MRE of ~1.2 with ~0.9 of the dataset predictable. On average, LRPCC is more accurate than any other algorithm, and machine learning algorithms are usually better than ordinary kriging (Fig. 3). There are many ways to integrate regression and interpolation results to improve the overall prediction performance. Here we use a mixture parameter  $p$  based on the kriging standard uncertainty estimates  $s$ , such that  $p=e^{-s}$ . In our test dataset, the maximum kriging contribution is about 76 % and the minimum is 0 %. Results show that LRPCC+kriging is more accurate at larger radii compared to LRPCC-alone (Fig. 3).

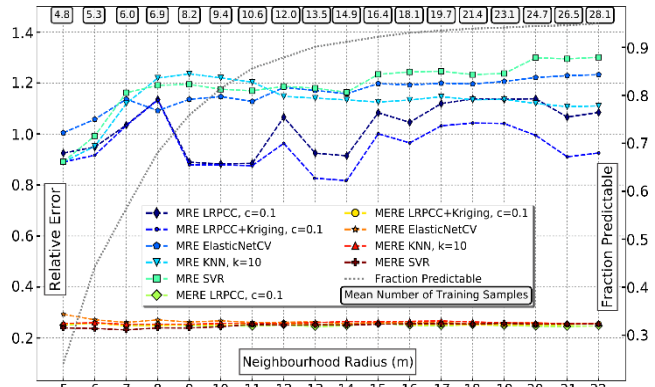


**Figure 3.** MRE and MER versus neighbourhood radii, a fraction of data points predictable and a mean number of training samples per prediction.

Cluster analysis of the sedimentological features resulted in at most four unique clusters that appear to be correlated with the samples spatial coordinates (Fig. 4).

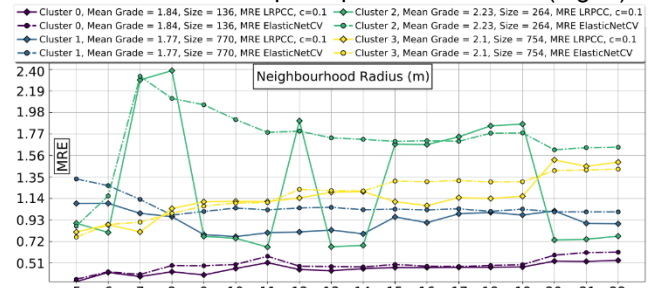


**Figure 4.** MRE of LRPCC ( $c = 0.1$ ) and ElasticNetCV vs neighbourhood radii for 4 unique sedimentological clusters/facies.

These clusters respond very differently to prediction, which produces distinct MRE profiles (Fig. 5).

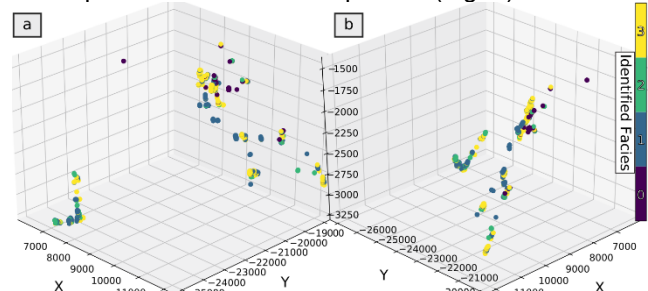


**Figure 5.** Spatial locations of members of 4 unique facies. Cluster 0 occurs at the shallowest depths; cluster 2 occurs in isolated patches throughout; cluster 1 occurs at mid to deeper depths and is mutually exclusive with cluster 0, cluster 3 occurs throughout.

The overall behaviour of the clusters is qualitatively the same with all regression algorithms, except where LRPCC is significantly more accurate (Fig. 4). Since these clusters are identified through sedimentological descriptions, we regard them as geological facies. Inverse transformation of predictions from log-space to grams per ton can be performed using Duan's smearing estimator (Duan 1983), which can be applied to any of the parametric methods.

## 5 Discussion

For LRPCC, the peak prediction accuracy occurs at a neighbourhood radius from 9 to 11 m (Fig. 3). Below 9 m distance, prediction performance degrades. LRPCC is able to reject a very small population of very-poorly predicted targets and eliminate poorly-correlated features. As a result, its MRE profile shows drastic dips in MRE at various radii. These points almost entirely belong to a particular facies (Figs. 4 and 5) that is located at mid to deeper depths of the sampled volume. Cluster analysis combined with gold grade predictions suggests that this facies consistently feature gold grades that are poorly correlated with the sedimentology. Detailed analysis suggests that members of this facies constitute less than about 15 % of the dataset population, 1/3<sup>rd</sup> of which feature high prediction errors that heavily inflate the MRE. The gold in this facies may be associated with non-sedimentary mineralisation processes and/or that additional processes have significantly modified the primary mineralisation processes, such as remobilisation via secondary hydrothermal processes (Phillips and Powel 2011). This is an interesting discovery and could contribute to the understanding of the genesis of the Witwatersrand gold deposits and the relative contributions of the various genetic hypotheses. Moreover, it is possible to employ GS-Pred to anticipate prediction behaviours for different facies and then generalise that knowledge to new exploration targets based on their geological descriptions.

There are at least two other probable causes for poorly correlated metal grades in samples that are not facies-specific. One is the qualitative nature of most of the sedimentological descriptions that imposes prediction errors of an unknown magnitude. Traditional interpolation techniques are at an inherent advantage in the sense that the assay data have well-constrained uncertainties and are fully-quantitative. Another probable cause is multiple remobilisation events of gold by various processes (be it by mechanical and/or chemical processes; Frimmel 2018).

Given that the dataset was originally unintended for machine-learning purposes, to be able to predict gold grade with low MERE demonstrates the potential of these algorithms and information within such datasets. Combining both GS-Pred and kriging can significantly improve prediction results at higher radii, because spatial correlations become progressively more significant with higher radii compared to localised relationships between gold grade and sedimentology. The best combination of the two still warrants further investigation.

## 6 Conclusion

We have proposed a set of algorithms called GS-Pred that use geological descriptions and assay data to predict gold grade and perform automated facies identification. GS-Pred was validated on a dataset of samples from the Witwatersrand Basin. It was able to classify samples into unique facies that feature different strengths of sedimentological control on the gold grade, and which are distributed differently in the sample coordinate space. Samples that cluster primarily with control sites for high gold mineralisation potential and feature a good prediction performance are good candidates for future exploration and site characterisation. The incorporation of both qualitative and quantitative geological and gold assay data in resource estimation of complex mineral deposits has the potential to expose hidden patterns of mineralisation diversity, that is of both an academic and industry interest.

## Acknowledgements

Glen Nwaila thanks CIMERA (Centre of Excellence for Integrated Mineral and Energy Resource Analysis) for funding this research, and Sibanye Stillwater for providing the data.

## References

- D'Agostino R, Pearson E (1973) Tests for departure from normality. Empirical results for the distributions of  $b_2$  and  $\sqrt{b_1}$ . *Biometrika* 60:613–622.
- Duan N (1983) Smearing Estimate: A Nonparametric Retransformation Method. *Journal of the American Statistical Association*, 78:605–610.
- Frimmel HE (2018) Episodic concentration of gold to ore grade through Earth's history. *Earth Science Reviews* 180:148–158.
- Frimmel HE, Minter WEL (2002) Recent developments concerning the geological history and genesis of the Witwatersrand gold deposits, South Africa: Society of Economic Geologists Special Publications 9:17–45.
- Goovaerts P (1997) *Geostatistics for Natural Resources Evaluation*. Oxford University Press, New York ISBN 0-19-511538-4.
- Kanevski M, Pozdnoukhov A, Timonin V (2009) Machine learning for spatial environmental data: theory. Applications and Software CRC Press Boca Raton. 368 pp.
- Kositcin N, Krapež B (2004) SHRIMP U–Pb detrital zircon geochronology of the Late Archaean Witwatersrand Basin of South Africa: relation between zircon provenance age spectra and basin evolution. *Precambrian Research* 129:141–168.
- Melo A, Sun J, Li Y (2017) Geophysical inversions applied to 3D geology characterisation of an iron oxide copper gold (IOCG) deposit in Brazil. *GEOPHYSICS*. 82:1–53.
- Nami N, Verrezen L (1986) The use of sedimentology to improve valuation on gold mines. Chamber of Mines of South Africa. Research report no. 32/86 Project no. GD1P.
- Phillips GN, Powell R (2011) Origin of Witwatersrand gold—A metamorphic devolatilisation-hydrothermal replacement model. *Applied Earth Sciences* 120:112–129.

# Comparisons of Metallogenesis within the Pyrenees-Alps-Zagros-Himalaya collisional orogens

Hongrui Zhang, Zengqian Hou

Key Laboratory of Deep-Earth Dynamics of Ministry of Natural Resources, Institute of Geology, Chinese Academy of Geological Sciences, China

**Abstract.** Modern collisional orogens represent a natural laboratory for the study of mineral deposit distribution in different tectonic environments. The Pyrenees, Alps, Zagros and Himalaya are all associated with Neo-Tethyan subduction and represent the youngest collisional orogens on Earth. Here, we compare these four orogens in terms of their composition, architecture, tectonic evolution, and metallogenic systems. The four orogens can be divided into simple and composite types. Simple orogens are represented by the Pyrenees and the Alps, and are characterized by narrow linear shapes in plain view and symmetric structures in cross-section, are free of arc magmatism, and are associated with Mississippi Valley-type Pb-Zn and orogenic gold deposits. In contrast, composite orogens, as exemplified by the Zagros-Iranian and Himalayan-Tibetan Plateaus, are associated with broad orogenic plateaus in plain view and asymmetrical structures in cross-section. These record extensive arc magmatism in continental margins, and are associated with a variety of deposit types including porphyry Cu-Mo, orogenic Au, Mississippi Valley type Pb-Zn, and detachment-fault-related polymetallic deposits.

## 1 Introduction

Collisional orogens are one of the most recognizable geotectonic features along convergent continental boundaries. The Pyrenees-Alps-Zagros-Himalaya mountain chain is a series of modern collisional orogens that are located along the southern margin of the Eurasian continent (Figure 1) and were generated following the closure of the Neo-Tethys Ocean. These four orogens have different patterns of collisional orogeny and tectonic histories, and are associated with different metallogenic systems (e.g., Hou and Zhang 2015). This study presents a review on these four orogens with the aim of gaining new insights into the metallogenesis across the region.

## 2 Architecture and evolution of the orogens

The Pyrenean orogen is a narrow linear mountain belt in the northern margin of the Iberian Peninsula. It is a typical symmetrical orogenic belt with a central axial zone that is surrounded by double-wedged ranges on each side (Verges and Fernandez 2012). It is formed by rifted and amalgamated of the Iberian plate with the Eurasian continent from Jurassic to Cenozoic.

The Alpine orogen within the Apennine region of southern Europe is a nearly E-W trending narrow linear

mountain belt that formed by the underthrusting of the Eurasian continent beneath the Adriatic Plate (Coward and Dietrich 1989). The Alps is similar to the Pyrenees in that the Alpine orogen is a symmetrical orogenic belt (Dal Piaz et al. 2003). However, the axial zone within the Alpine orogen is more complex than that in the Pyrenees and is divided into three units (Schmid et al. 2004): the Austroalpine domain, the Penninic domain, and the Helvetic domain. The tectonic evolution of the Alpine orogen is similar to that of the Pyrenean orogen in that it is divided into two phases: Mesozoic breakup and Cenozoic collision.

The structure of the Zagros-Iranian Plateau is different to that of the Pyrenean and Alpine orogens in that this region does not contain fold-and-thrust belts or an associated foreland basin on the upper side of the collision zone, but contains a broad tectono-magmatic zone that is present within the Sanandaj-Sirjan magmatic and metamorphic belt (SSZ) and the Urumieh-Dokhtar magmatic assemblage (UDMA) (Agard et al. 2011), indicating the Zagros-Iranian Plateau has an asymmetrical structure.

The Himalayan-Tibetan Plateau represents a composite accretionary-collisional orogen (Pan et al. 2012; Zhang et al. 2017a). The plateau also contains a huge tectono-magmatic zone that spans thousands of kilometers. The collisional related tectonism and magmatism of the four orogens are summarized in Figure 2.

## 3 Mineral deposits of the orogens

The Pyrenean orogen contains numerous Pb-Zn deposits (Figures 3a) that are generally located within foreland basins on both sides of the orogen (Leach et al. 2006).

The collision-related deposits of the Alpine orogen include orogenic Au gold deposits and MVT-type Pb-Zn deposits (Figures 3b). The orogenic Au deposits are generally located in the western Monte Rosa (Pettke et al. 2000) and eastern Hohe Tauern areas (Horner et al. 1997). The Alpine MVT-type Pb-Zn deposits are generally located within the Drau Range area of the middle and eastern parts of the orogen (Henjes-Kunst et al. 2017).

The Zagros-Iranian Plateau hosts a number of economically significant mineral deposits and contains various styles of mineralization. Mineral deposits related to continental collision include porphyry Cu-Mo-Au, MVT Pb-Zn, and orogenic Au deposits (Figure 3c). The main metallogenic belts include the Arasbaran-Kerman porphyry copper belt (Aghazadeh et al. 2015), the Takab-

Yazd MVT Pb-Zn belt (Ehya et al. 2010)), and the Piranshahr-Saqez-Sardasht orogenic Au district (Aliyari et al. 2012).

Numerous large and giant metal deposits within the Himalayan-Tibetan Plateau (Figure 3d). These include the Gangdese and Yulong porphyry copper belts (Hou et al. 2009a), the Sanjiang MVT-type Pb-Zn belt (Zhang et al. 2017b), the Ailaoshan orogenic Au belt (Deng et al. 2014), the Western Sichuan carbonatite-related rare earth element (REE) belt (Hou et al. 2009b) and the southern Tibet detachment-fault-related polymetallic belt (Li et al. 2017).

## 4 Comparison and discussion

### 4.1 Basic types of collisional orogenic belt

Continental collision orogens can be classified into simple and composite types, as evidenced by the four examples outlined above. Simple collisional orogens are characterized by a narrow linear orogenic belt, and has associated metallogenic systems that are dominated by processes within the middle and upper crust, forming mineralization such as MVT Pb-Zn and orogenic Au deposits, as exemplified by the Pyrenees and the Alps. Although collisional related calc-alkaline and potassic magmatism may develop, no pre-collisional magmatism recorded in this type of collision. In comparison, composite collisional orogens are characterized by the occurrence of continental arc magmatism with a broad orogenic plateau. The metallogenic systems in these types of collisional environments are associated with both crust and mantle processes, and form mineralization such as carbonatite-related REE deposits, collisional porphyry copper deposits (PCDs), orogenic Au deposits, MVT-like Pb-Zn deposits, and detachment-fault-related polymetallic deposits. This type of collision is exemplified by the Zagros-Iran and Himalayan-Tibetan plateaus.

Simple collisional orogens have symmetrical structures (Figure 4a) that consist of a central axial zone surrounded by fold-and-thrust belts and foreland basins. In contrast, composite collisional belts have asymmetrical structures (Figure 4b). For example, the Zagros orogenic belt contains a broad tectono-magmatic zone that contains the SSZ, the UDMA, and even part of the Central Iran block. The SSZ and UDMA are related to continental arc formation associated with subduction of the Neo-Tethys oceanic crust, whereas the Central Iran block contains continental lithospheric material that was located above the Paleo-Tethyan subduction zone. For the Himalayan orogeny, its influence has extended to a broad tectono-magmatic zone that includes the Lhasa, Southern Qiangtang, and Northern Qingtang blocks. These blocks were amalgamated by multiple accretionary and collisional processes between the Mesozoic and the Paleozoic, and the continental arc lithosphere in the Lhasa block was generated by subduction of the Neo-Tethys oceanic crust.

### 4.2 Mineralization within different types of continental collisional orogen

Different types of collisional orogens have similarities in terms of metallogenesis. For example, sediment-hosted Pb-Zn deposits (in the form of MVT-type and MVT-like deposits) are present in all four of the continental collisional orogenic belts. Three of the four orogenic belts considered here (except the Pyrenees) contain limited orogenic Au deposits. This type of gold deposit generally forms in accretionary orogenic settings and is closely related to metamorphic fluids that can leach gold from source rocks, be transported along major fault zones, and precipitate gold at sites of local extension (Goldfarb et al. 2005). During continental collision, metamorphic fluids can be produced by dehydration of the subducting crust and transported along translithospheric faults, including sutures and large shear zones, which provide ideal pathways for migration of the metamorphic fluids.

However, there are also some differences in the mineral deposits that form in different types of collisional orogen. The simple collisional orogens are absent of magmatic arcs and do not generally contain magmatism-related ore deposits, including carbonatite-related REE, PCD mineralization associated with magmas generated by the decompressional melting of sublithospheric mantle, and polymetallic deposits related to partial melting of the middle and upper crust. All of these ore deposits are present within the composite collisional orogens in addition to the occurrence of continental margin arcs. This indicates that these composite collisional orogens involve the intense reactivation and migration of crust and mantle materials as well as the formation of large ore deposits in shallow crustal environments.



**Figure 1.** Global distribution of collisional orogens (modified from [www.ngdc.noaa.gov](http://www.ngdc.noaa.gov)).

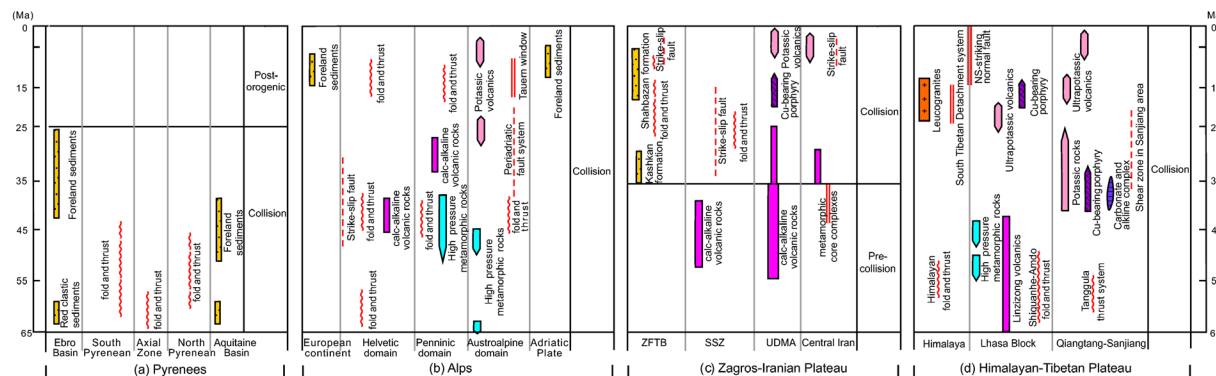


**Figure 2.** Tectonism and magmatism recorded by the Pyrenean, Alpine, Zagros-Iranian, and Himalayan-Tibetan collisional orogens.

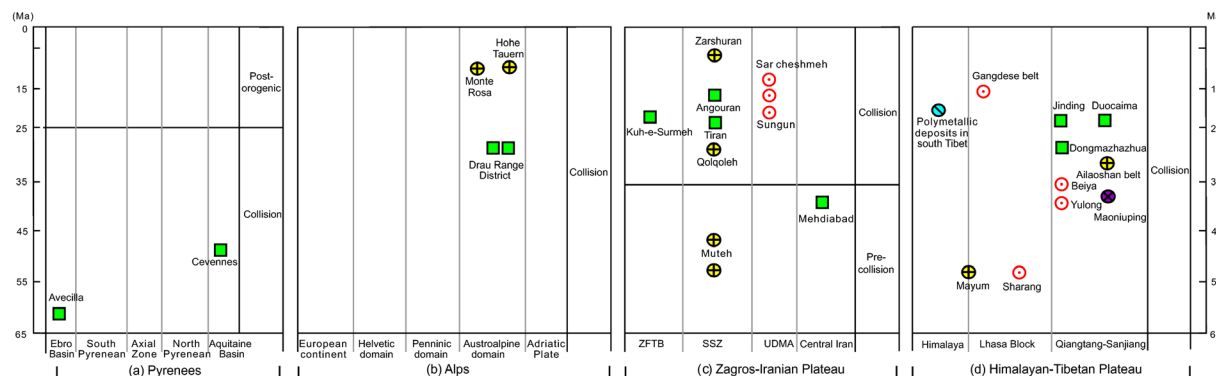


**Figure 3.** Temporal distribution of mineral deposit types within the Pyrenean, Alpine, Zagros-Iranian, and Himalayan-Tibetan collisional orogens.

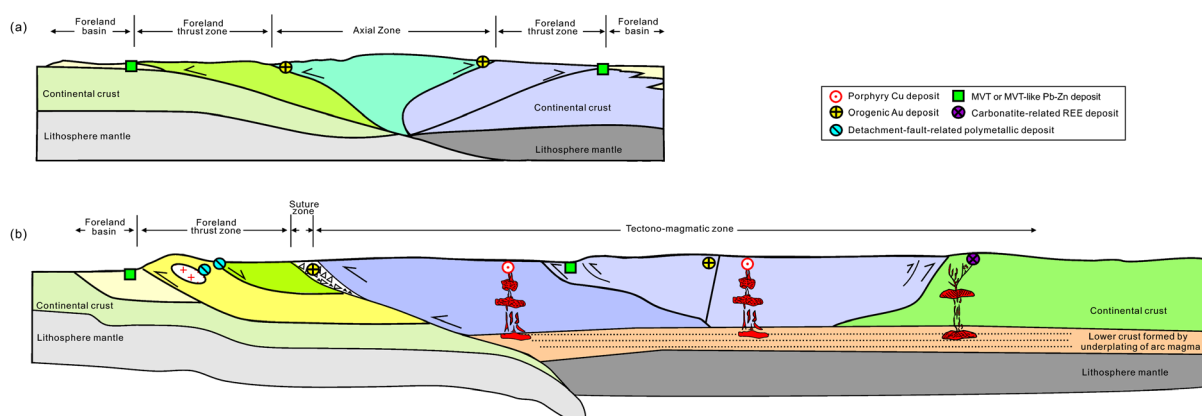


**Figure 4.** Sketch diagram showing the relationship between structures and the main mineral deposit types within (A) simple and (B) composite types of collisional orogen (not to scale)

## Acknowledgements

This research was supported by the National Natural Science Foundation of China (Grant Nos. 41772088, 41773042, 41773043), and the China Geological Survey (Grant No. DD20190001). Contribution to IGCP 662.

## References

- Agard P, Omrani J, Jolivet L, Whitechurch H, Vrielinck B, Spakman W, Monie P, Meyer B, Wortel R (2011) Zagros orogeny: a subduction-dominated process. *Geological Magazine* 148(5–6): 692–725.
- Aghazadeh M, Hou Z, Badrzadeh Z, Zhou L (2015) Temporal–spatial distribution and tectonic setting of porphyry copper deposits in Iran: Constraints from zircon U–Pb and molybdenite Re–Os geochronology. *Ore Geology Reviews* 70: 385–406.
- Aliyari F, Rastad E, Mohajjel M (2012) Gold Deposits in the Sanandaj–Sirjan Zone: Orogenic Gold Deposits or Intrusion–Related Gold Systems? *Resource Geology* 62: 296–315.
- Coward M, Dietrich D (1989) Alpine tectonics—an overview. Geological Society, London, Special Publications 45(1):1–29.
- Ehya F, Lotfi M, Rasa I (2010) Emarat carbonate-hosted Zn–Pb deposit, Markazi Province, Iran: A geological, mineralogical and isotopic (S, Pb) study. *Journal of Asian Earth Sciences* 37: 186–194.
- Dal Piaz GV, Bistacchi A, Massironi M (2003) Geological outline of the Alps. *Episodes* 26(3):175–180.
- Deng J, Wang Q, Li G, Santosh M (2014) Cenozoic tectono-magmatic and metallogenic processes in the Sanjiang region, southwestern China. *Earth-Science Reviews* 138: 268–299.
- Goldfarb RJ, Baker T, Dube B, Groves DI, Hart CJ, Gosselin P (2005) Distribution, character, and genesis of gold deposits in metamorphic terranes. *Economic Geology* 100:407–450.
- Henjes-Kunst E, Raith JG, Boyce AJ (2017) Micro-scale sulfur isotope and chemical variations in sphalerite from the Bleiberg Pb–Zn deposit, Eastern Alps, Austria. *Ore Geology Reviews* 90:52–62.
- Horner J, Neubauer F, Paar WH, Hansmann W, Koeppel V, Robl K (1997) Structure, mineralogy, and Pb isotopic composition of the As–Au–Ag deposit Rotgilden, Eastern Alps (Austria): significance for formation of epigenetic ore deposits within metamorphic domes. *Mineralium Deposita* 32:555–568.
- Hou ZQ, Yang ZM, Qu XM, Meng XJ, Li ZQ, Beaudoin G, Rui ZY, Gao YF, Zaw K (2009a) The Miocene Gangdese porphyry copper belt generated during post-collisional extension in the Tibetan Orogen. *Ore Geology Reviews* 36:25–51.
- Hou ZQ, Tian SH, Xie YL, Yang ZS, Yuan ZX, Yin SP, Yi LS, Fei HC, Zou TR, Bai G (2009b) The Himalayan Mianning–Dechang REE belt associated with carbonatite–alkaline complexes, eastern Indo-Asian collision zone, SW China. *Ore Geology Reviews* 36:65–89.
- Hou ZQ, Zhang HR (2015) Geodynamics and metallogeny of the eastern Tethyan metallogenic domain. *Ore Geology Reviews* 70:346–384.
- Leach D, Macquar JC, Lagneau V, Leventhal J, Emsbo P, Premo W (2006) Precipitation of lead–zinc ores in the Mississippi Valley-type deposit at Treves, Cevennes region of southern France. *Geofluids* 6:24–44.
- Li G M, Zhang L K, Jiao Y J, Xia X B, Dong S L, Fu J G, Liang W, Zhang Z, Wu J Y, Dong L, Huang Y (2017) First discovery and implications of Cuonadong superlarge Be–W–Sn polymetallic deposit in Himalayan metallogenic belt, southern Tibet. *Mineral Deposits* 36(4): 1003–1008.
- Pan G, Wang L, Li R, Yuan S, Ji W, Yin F, Zhang W, Wang B (2012) Tectonic evolution of the Qinghai–Tibet plateau. *Journal of Asian Earth Sciences* 53: 3–14.
- Pettke T, Diamond LW, Kramers JD (2000) Mesothermal gold lodes in the north–western Alps: A review of genetic constraints from radiogenic isotopes. *European Journal of Mineralogy* 12:213–230.
- Schmid SM, Fugenschuh B, Kissling E, Schuster R (2004) Tectonic map and overall architecture of the Alpine orogen. *Eclogae Geologicae Helvetiae* 97(1):93–117.
- Verges J, Fernandez M (2012) Tethys–Atlantic interaction along the Iberia–Africa plate boundary: The Betic–Rif orogenic system. *Tectonophysics* 579:144–172.
- Zhang HR, Yang TN, Hou ZQ, Dai MN, Hou KJ (2017a) Permian back-arc basin basalts in the Yushu area: New constrain on the Paleo–Tethyan evolution of the north-central Tibet. *Lithos* 286:216–226.
- Zhang HR, Yang TN, Hou ZQ, Song YC, Liu YC, Yang ZS, Tian SH (2017b) Structural controls on carbonate-hosted Pb–Zn mineralization in the Dongmozhazhua deposit, central Tibet. *Ore Geology Reviews* 90:863–876.

# 500 Myrs in the making: control of Gondwana margin assembly on Carboniferous orogenic gold in Peru

Daniel Wiemer, Steffen G. Hagemann, Nicolas Thébaud  
University of Western Australia

Carlos Villanes  
Compañía Minera Poderosa S.A.

**Abstract.** Carboniferous intrusion-related orogenic gold deposits in the Eastern Andean Cordillera display a high distribution-density in northern Peru. New geological-structural mapping suggests a basement domain boundary controlling the emplacement of large plutonic complexes and associated hydrothermal gold deposits. The southern *Montanitas Domain* basement comprises thrust nappes of imbricated ophiolite slices and granitic gneiss. The basement of the northern *Pataz Domain* forms a fold-and-thrust belt, where low-grade Ordovician volcanic arc rocks and marginal sedimentary rocks are thrust over semi-pelitic schists. Structural data indicates that both domains were deformed during a common orogeny, ascribed to the Late Famatinian (ca. 440 Ma) that affected the Eastern Cordillera to the south. North of the study area, no Late Famatinian imprints are documented. It is proposed that the study area is situated at the northernmost extent of an orogenic belt that formed through re-collision with the putative Paracas terrane that detached from Amazonia during Rodinia break-up. Carboniferous compression was accommodated in dextral strike-slip along the trans-crustal Rio Maranon Fault. We suggest that the greater width of the basement orogen to the south led to magma and fluid channeling at its northern tip. Gold mineralization focused in a narrow, strike-slip-induced dilation zone north of the basement block.

## 1 Introduction

The Eastern Andean Cordillera (EAC) of Peru is punctuated by numerous Carboniferous granitoid-hosted orogenic gold districts. The highest density and most productive (i.e., Pataz-Parcoy) known deposits are situated in a narrow belt at the latitude of Trujillo in northern Peru (Fig. 1; Haebel et al. 2004). Considering that the gold-hosting Carboniferous plutonic belt extends over hundreds of km along strike, the spatially restricted distribution of most productive deposits is intriguing. Specific sites in the tectonic framework of the EAC may have favored concentration of magmatic-hydrothermal gold-bearing fluids. Indeed, the pre-Carboniferous EAC formed through complex tectono-magmatic events associated with repeated terrane detachments and re-collisions along the (paleo-)Gondwana margin since the Mesoproterozoic (Chew et al. 2007, 2016; Mišković et al. 2009). The spatial delineation of crustal blocks/terrane, and their significance in shaping the basement tectonic framework(s) for the Carboniferous gold systems,

however, remain to be demonstrated.

Geological-structural mapping of a key area was conducted in the high production Pataz-Parcoy districts, and extends southward into the Montanitas-Ongón prospects (Fig. 1). Previous zircon isotopic data from Carboniferous igneous rocks, and basement depositional and metamorphic ages, indicate along strike variation in magmatic processes and basement components in the area (Chew et al. 2016; Angerer et al. 2018). Our results support the presence of distinct basement domains. We present a refined model of terrane assembly at the Peruvian Gondwana margin and discuss the role of basement inheritance on Carboniferous gold formation and distribution.

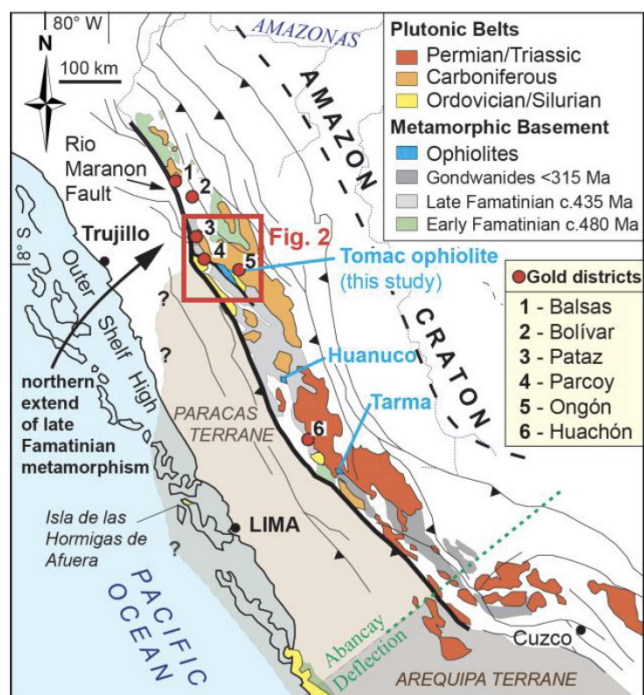


**Figure 1.** Simplified geological map of the Eastern Andean Cordillera (modified from Haebel et al. 2004; Romero et al. 2013; Chew et al. 2016).

## 2 Regional tectonic setting

Grenvillian basement of the EAC is evident in inherited and detrital zircons, attesting to the Mesoproterozoic Sunsas Orogeny as consequence of collision of Laurentia and Amazonia (Chew et al. 2007; Mišković et al. 2009; Witt et al. 2013). Rodinia break-up is poorly documented

in the EAC. However, putative ophiolite vestiges (Tarma, Fig. 1) indicate oceanic crust formation at ca. 720 Ma (Sm-Nd isochron; Tessinari et al. 2011). Ordovician arc magmatism along the entire EAC occurred at ca. 480 Ma during the Early Famatinian orogenic cycle (Chew et al. 2007). A Late Famatinian cycle is recorded in ~445 Ma granitic magmatism and subsequent metamorphism at ca ~435 Ma (U-Pb zircon and titanite, respectively; Chew et al. 2016). Importantly, Late Famatinian imprints are only observed as far north as the present study area (Fig. 1), affecting sedimentary rocks with maximum depositional ages consistent with Early Famatinian sources ("Young" Maranon Complex). Towards the north, no Late Famatinian imprints are documented, and maximum depositional ages are ~750 Ma ("Old" Maranon Complex) (Chew et al. 2007; Witt et al. 2013). Geochronological data from offshore boreholes attest to the presence of Grenvillian to Ordovician basement, which led to the interpretation of the existence of the Paracas and possibly the Oaxaquia (further west) terranes, interpreted to have been detached during Rodinia break-up and recollided with the Gondwana margin. In fact, recent metamorphic constraints indicate the formation of a paired HP/LT collisional belt, which incorporated the Tarma ophiolite during the Late Famatinian orogeny (Willner et al. 2014). However, the northernmost extent of Paracas offshore basement is located at the *Isla de las Hormigas de Afuera* (Fig. 1), whereas further to the north Permian ages are detected (Romero et al. 2013). Hence, the northern delineation of the putative Paracas terrane remains unknown.

Voluminous Carboniferous I-type magmatism largely affected the central to northern EAC (Fig. 1) and peaked between ca. 340–320 Ma (Witt et al. 2013). The Carboniferous gold deposits focus along the Rio Maranon Fault, a major trans-crustal structure and likely Famatinian suture (Schreiber et al. 1990; Fig. 1). Gold is found in quartz-sulfide veins, hosted in the Carboniferous granitic plutons.

### 3 Results from the study area

Geological-structural mapping revealed a significant change in basement lithologies from north to south that spatially coincides with a bend in the Rio Maranon Fault (Fig. 2). We defined a northern *Pataz Domain* and a southern *Montanitas Domain*, and provide evidence for their distinct basement lithological-structural inventories and Carboniferous magma emplacement style, below.

**Pataz Domain:** In the Pataz Domain, Carboniferous gold system-hosting granitoid suites intrude a narrow NNW-trending corridor parallel, and directly adjacent to the Rio Maranon Fault (Fig. 2). The granitic suites intrude two greenschist facies basement tectonic units: (i) semi-pelitic schists with rare m-thick quartzite intercalations, ascribed to the "Young" Maranon Complex (MC; max U-Pb detrital zircon depositional age of ~461 Ma; Chew et al. 2007) to the west, and (ii) easterly adjacent, tectonically overlying volcanic, volcanoclastic, and sedimentary rocks belonging to the *Eastern Andean Cordillera Group* (EACG; max depositional age of ~467

Ma; Witt et al. 2013). Sedimentary rocks of the EACG are part of the Contaya Formation, comprising *Graptolite* strata and turbidite sequences (Hughes et al. 1980; Schreiber et al. 1990), and volcanic rocks of the EACG display characteristic arc signatures.

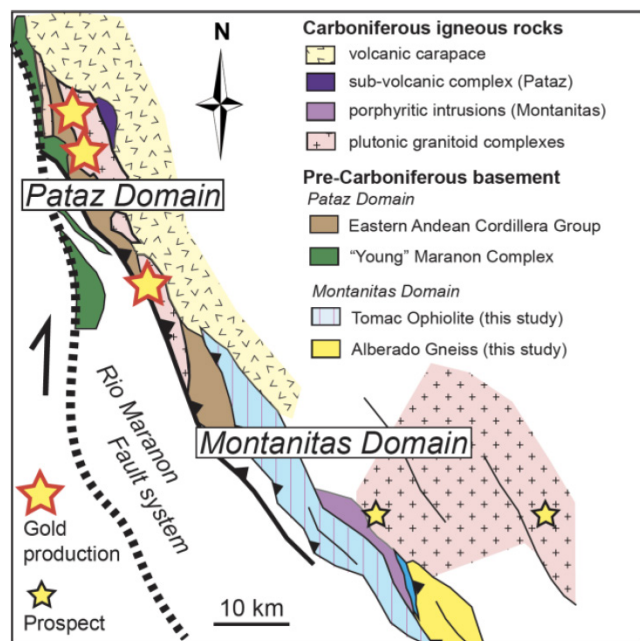


Figure 2. Simplified geological-structural map of the study area (location shown in figure 1). Description in text.

The basement tectonic units of the Pataz Domain show a common deformation history (D<sub>1</sub>-D<sub>3</sub>). Early S<sub>1</sub>-foliations developed parallel to bedding (S<sub>0</sub>) planes. S<sub>0</sub>/S<sub>1</sub>-planes strike NNW and dip dominantly to the E/NE (D<sub>1</sub>). Subsequent F<sub>2</sub>-folding around S<sub>1</sub>-strike-parallel subhorizontal axes is evident in dm-scale S/Z-type parasitic folds within up- or downward verging limbs of transposed larger-scale folds. Transposition of high intensity fold hinge zones led to local S<sub>2</sub> foliations. The S<sub>2</sub> planes correlate geometrically with brittle-ductile D<sub>2</sub> fault arrays. These E/NE-dipping faults caused the tectonic juxtapositioning of the MC and the EACG through top to the W/SW thrusting. A D<sub>3</sub> event locally reactivated these faults as ductile to brittle normal shear zones.

The Carboniferous plutonic rocks (Fig. 2) display a clear relative timing of distinct magma emplacements: (i) diorite, (ii) granodiorite/tonalite, and (iii) late-stage monzogranite, and pegmatite/aplite dikes. These components successively intruded to form the presently exposed batholith, without showing systematic spatial-compositional trends. It is noted, however, that the eastern extent of the batholith is unknown and tectonically delineated by over-thrust extrusive equivalents (*volcanic carapace*, Fig. 2). Magma emplacement followed the NE-dipping S<sub>0</sub>/S<sub>1</sub> planes of the basement, as evident in numerous parallel 10- to 100-m-wide supra-solidus magmatic flow zones of elongated diorite enclaves in granodiorite.

The Pataz Domain experienced a syn- to post-batholith syn-mineralization D<sub>4</sub> event that produced F<sub>4</sub>-kink folds and faults in the basement, and faults and fault-

fill veins in the batholith. Auriferous quartz-sulfide fault-fill veins follow three orientations: (i) the steep N/NNW-trending western batholith contact, (ii) the medium ENE-dipping basement-inherited S<sub>1</sub>-planes in the magmatic architecture, and (iii) shallow-medium NE-dipping veins are observed in the footwall of the mineralized system. Type-iii veins formed as thrust faults that match Andersonian-type orientations assuming NE-SW compression. Type-i/ii veins display progressive textural dextral shear development. All veins formed during an early quartz-pyrite paragenetic stage (Fig. 3, D<sub>4a</sub>). WNW-trending steep faulting accompanied early vein formation, as evident in syn-mineralization drag-folds. A second quartz-pyrite-sphalerite-galena paragenetic stage fills dilational sites indicating re-opening of former shear/fault veins associated with N-NE-trending normal faults. The normal faults indicate NW-SE extension consistent with horst-and-graben development during late-stage deposition of the volcanic carapace (Fig. 3, D<sub>4b</sub>).

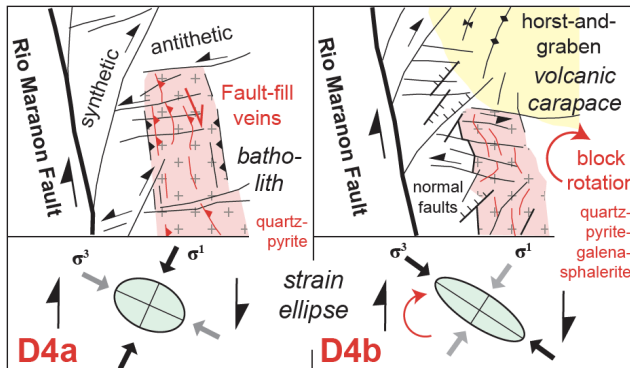


Figure 3. Schematic structural model for gold vein system formation during D<sub>4</sub> in the northern Pataz Domain.

**Montanitas Domain:** In the Montanitas Domain, the western demarcation of the Carboniferous batholith is markedly offset eastward from the present surface exposure of the Rio Maranon Fault (Fig. 2). Here, the magmatic suites extend over a much wider area towards the east, and display a more systematic spatial trend of eastward increase in more differentiated magmas (diorite, granodiorite, potassic granite; not shown in Fig. 2).

The basement between the Rio Maranon Fault and the Carboniferous igneous rocks constitutes imbricated orogenic nappes, comprising the newly identified *Tomac Ophiolite* and *Alberado Gneiss* (Fig. 2). Where relatively undeformed, the Tomac Ophiolite comprises alternating pillow basalt (Fig. 4a) and more massive basalt and dolerite (i.e., diabase). Deformation intensity increases towards high-strain thrust zones within the nappe stack, where sheared pillows and/or mafic schists are observed. The highest strain occurred where the Alberado Gneiss nappes are thrust over the mafic rocks (top to SW). Here, the two basement units are interfolded isoclinally (D<sub>2</sub>) over 10-50 m-wide zones (Fig. 4b). Geochemical data of the Tomac Ophiolite indicates MORB affinity (Fig. 4c). The Alberado Gneiss nappes are differentiated granites with pronounced arc signatures (Fig. 4c). The gneisses comprise remnant former upper amphibolite facies

mineralogy (plagioclase, biotite, amphibole), but are often overprinted by retrograde chlorite-bearing assemblages. Both basement units were affected by cm-scale recumbent folds and associated incipient hinge faults, which we correlate to the F<sub>4</sub> kink-folds and associated faults in the Pataz Domain basement.

Auriferous quartz-sulfide veins in the Montanitas Domain mostly form arrays sub-parallel to steep NNW-striking contacts between distinct Carboniferous intrusions, or sub-parallel to ~NW-striking faults similar to those observed in the Pataz Domain.

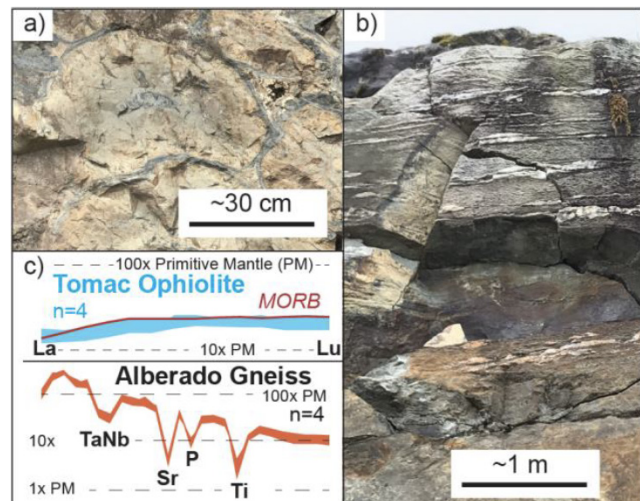


Figure 4. a. Pillow basalt (Tomac Ophiolite). b. F<sub>2</sub>-isoclinal interfolding of the Tomac Ophiolite and the Alberado Gneiss in high-strain thrust zone. c. MORB-type REE pattern for the Tomac Ophiolite and trace element arc-signature of Alberado Gneiss (Primitive Mantle normalized after McDonough and Sun, 1995).

## 4 Discussion

Based on presented data, we propose the following model:

- (1) We correlate the newly identified Tomac Ophiolite with previously identified ophiolites to the south (e.g., in Tarma, Huanuco). Oceanic protoliths formed during Rodinia break-up at ~720 Ma (Tessinari et al. 2011; Fig. 5a).
- (2) EACG volcanic activity was part of extensive Early Famatinian arc formation along the EAC (Fig. 5b). Based on the similar deformation history, it is likely that the Alberado Gneiss protoliths were emplaced at this time.
- (3) Based on previous constraints for synchronous deposition of EACG and “Young” MC detritus, we propose a marginal to sub-marine arc-forearc environment. During this inter-Famatinian phase, *Graptolite* shales, turbidites (EACG) and outboard deep-marine sediments (MC) were deposited (Fig. 5c).
- (4) In line with evidence for paired metamorphic belt formation and associated Tarma Ophiolite emplacement further south, we propose that Late Famatinian collisional orogeny affected the study area (D<sub>1</sub>-D<sub>2</sub>; Fig. 5d). As ophiolite and gneiss nappes are only observed in the Montanitas Domain, and no Late Famatinian imprints are recorded north of the study area, we suggest that the study area was situated at the northern extent of this

orogeny. We propose that this marks the northern delineation of the Paracas terrane and therefore limits its re-collision impact on the Gondwana margin.

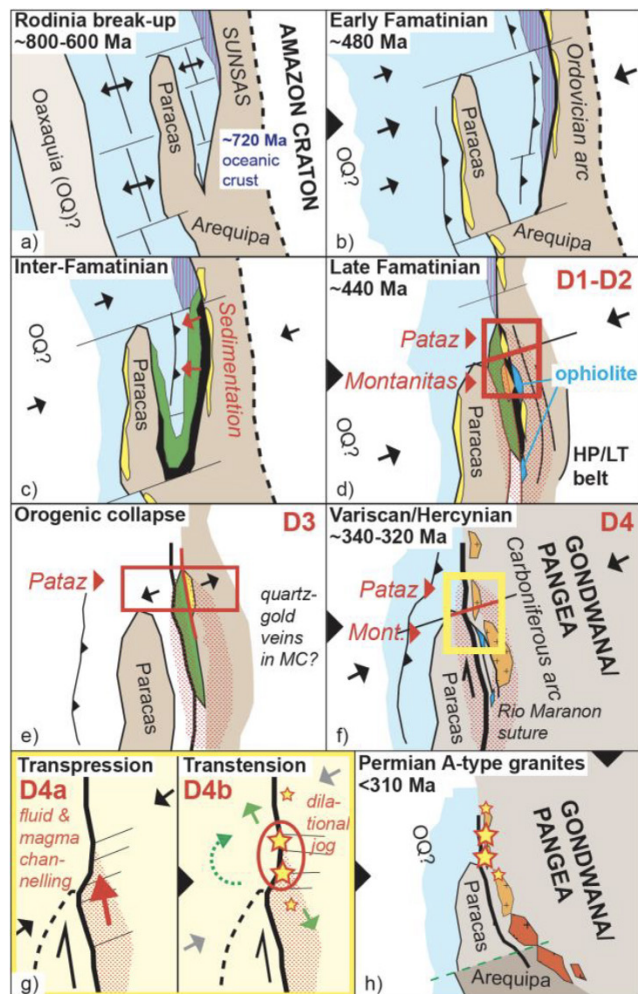


**Figure 5.** Illustration of model for micro-terrane assembly in north-central Peru. Refer to text for description of a-h.

(5) Normal fault reactivation in the Pataz Domain (D<sub>3</sub>) records post-orogenic collapse (Fig. 5e).

(6) Carboniferous arc formation affected the entire central-north Peruvian EAC (Fig. 5f). Magma and fluid were channeled into a narrow corridor in the Pataz Domain. Upon batholith crystallization, initial veins formed through energy release(s) accommodating ongoing strike-slip (D<sub>4a</sub>). The southern basement block caused a dilational jog, where block rotation and normal faulting accompanied mineralization of the gold-bearing second paragenetic stage (D<sub>4b</sub>; Fig. 5g).

(7) Permo-Triassic S- and A-type magmatism focused along the southern Famatinian suture (Fig. 5h).

## 5 Implications

A new model for Gondwana margin assembly in the EAC

provides insights into the formation of gold deposits in northern Peru. The northern delineation of the Paracas terrane is recorded in the newly identified Tomac Ophiolite and Alberado Gneiss. Carboniferous intrusion-related orogenic gold formed in a strike-slip-induced dilatational corridor north of this Late Famatinian basement. The Paracas detachment may have isolated an upper mantle reservoir, fertilized during renewed subduction onset, and tapped in the Carboniferous.

## Acknowledgements

We thank the Compania Minera Poderosa S.A., particularly F. Cueva. Geochemical analyses were performed by the Bureau Veritas, Vancouver, Canada.

## References

- Angerer T, Kemp AIS, Hagemann SG, Witt WK, Santos JO, Schindler C, Villanes C (2018) Source component mixing controls the variability in Cu and Au endowment along strike of the Eastern Andean Cordillera in Peru. *Contrib Mineral Petrol* 173:1-36.
- Chew DM, Schaltegger U, Košler J, Whitehouse MJ, Gutjahr M, Spikings RA, Mišković A (2007) U-Pb geochronological evidence for the evolution of the Gondwana margin of the north-central Andes. *Geol Soc Am Bull* 119:697-711.
- Chew DM, Pedemonte G, Corbett E (2016) Proto-Andean evolution of the Eastern Cordillera of Peru. *Gondwana Res* 35:59-78.
- Haeberlin Y, Moritz R, Fontboté L, Cosca M (2004) Carboniferous Orogenic Gold Deposits at Pataz, Eastern Andean Cordillera, Peru: Geological and Structural Framework, Paragenesis, Alteration, and 40Ar/39Ar Geochronology. *Econ Geol* 90:73-112.
- Hughes C, Rickards R, Williams A (1980) The Ordovician fauna from the Contaya Formation of eastern Peru. *Geol Mag* 117:1-20.
- McDonough WF, Sun S-S (1995) The composition of Earth. *Chem Geol* 120:223-253.
- Mišković A, Spikings RA, Chew DM, Košler J, Ulianov A, Schaltegger U (2009) Tectonomagmatic evolution of Western Amazonia: Geochemical characterization and zircon U-Pb geochronologic constraints from the Peruvian Eastern Cordillera granitoids. *Geol Soc Am Bull* 121:1298-1324.
- Romero D, Valencia K, Alarcón P, Peña D, Ramos VA (2013) The offshore basement of Peru: Evidence for different igneous and metamorphic domains in the forearc. *J South Am Earth Sci* 42:47-60.
- Schreiber DW, Amstutz GC, Fontboté L (1990) The formation of auriferous quartz-sulfide veins in the Pataz region, northern Peru: A synthesis of geological, mineralogical, and geochemical data. *Miner Depos* 25:136-140.
- Tessinari CCG, Castroviejo R, Rodrigues JF, Acosta J, Pereira E (2011) A Neoproterozoic age for the chromitite and gabbro of the Tapo ultramafic Massif, Eastern Cordillera, Central Peru and its tectonic implications. *J South Am Earth Sci* 32:429-437.
- Willner AP, Tessinari CCG, Rodrigues JF, Acosta J, Castroviejo R, Rivera M (2014) Contrasting Ordovician high- and low-pressure metamorphism related to a microcontinent-arc collision in the Eastern Cordillera of Peru (Tarma province). *J South Am Earth Sci* 54:71-81.
- Witt WK, Hagemann SG, Villanes C, Zeng Q (2013) New geochronological results and structural evolution of the Pataz gold mining district: Implications for the timing and origin of the batholith-hosted veins. *Ore Geol Rev* 50:143-170.

# Geodynamic and metallogenetic reconstruction of the Neoarchean Qingyuan greenstone belt: evidence from petrogeochemistry and U-Pb geochronology

Zidong Peng, Lianchang Zhang, Changle Wang, Xiaoxue Tong

Institute of Geology and Geophysics, Chinese Academy of Sciences, China

**Abstract.** The Neoarchean Qingyuan greenstone belt (QGB) is located on the northern margin of the North China Craton (NCC). Despite close geological similarities with other greenstone terranes in the NCC, the QGB are characterized by hosts the oldest volcanogenic massive sulphide (VMS) deposit (Hongtoushan VMS, with 0.15 Mt Cu at 1.6% and 0.21 Mt Zn at 2.3%) in China. Moreover, there are also several economic banded iron formation-type iron deposits (e.g., Xiaolaihe, Yujabu, and Xiadianzi BIF) in this belt. Despite previous work in the area, the tectonic setting of the QGB is under debated; whereas the genetic relationship between mineralization and chemostratigraphic evolution of the area has also remained enigmatic. In this study, we present an integrated study of the supracrustal rocks in the QGB, including field and petrographic observations, whole-rock lithogeochemical data, and U-Pb geochronology of meta-felsic rocks that are interlayered with the BIF. The objectives are to (1) elucidate the petrogenetic history of these mafic and felsic volcanic rocks, and reconstruct their geodynamic setting, and (2) decode the metallogenetic history of VMS and BIF in the QGB.

## 1 Introduction

Archean greenstone belts are fertile terranes for various mineral deposits, among which the volcanogenic massive sulphide (VMS) deposits and banded iron formations (BIFs) of Algoma type have significant research and economic significance (Bekker et al. 2010; Mercier-Langevin et al. 2014). In general, there has been unprecedented research on virtually all aspects of VMS and BIF has mushroomed in the past fifty years (e.g., Franklin et al., 2005; Bekker et al., 2010; Piercey 2011). Interestingly, some of these research illustrates that in the Precambrian VMS and BIF usually have close spatial and temporal associations (e.g., Huston and Logan, 2004), and in most cases they are recognized as syngenetic and strata bounded within the supracrustal rocks of old craton (e.g., Zaleski and Peterson 1995; Slack et al. 2007). Although great progress has been made to figure out the cause and connection of VMS-BIF paragenetic assemblages, but there are still some aspects remain poorly constrained, such as their tectonic setting and the relationship between geodynamic evolution of the greenstone belt and its mineralization.

The Neoarchean Qingyuan greenstone belt (QGB) is located on the northern margin of the North China Craton (NCC) (Fig. 1a), it hosts several VMS and BIF-type iron deposits that formed synchronously (Wan et al. 2012; Zhang 2014; Zhu et al. 2015). Nevertheless, for a long

time the tectonic setting of the QGB is under debated, whether it represents an intra-continental rift (Zhai et al. 1985) or formed above a mantle plume (Wu et al. 2013) or was similar to modern arcs (Peng et al. 2015). Furthermore, the relationship between its mineralization and chemostratigraphic evolution has also remained enigmatic. Hence, a detailed work on the supracrustal rock sequences of the QGB may be a fruitful approach to achieve these attempting targets, and is presented herein.

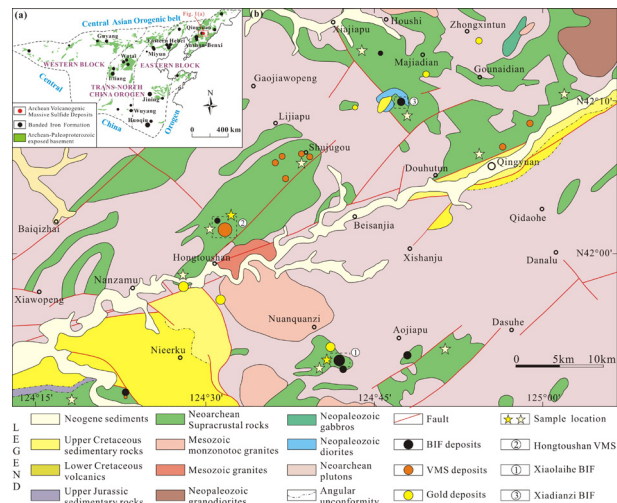


**Figure 1.** (a) Tectonic subdivision of the North China Craton (NCC) showing location of the Qingyuan area and distribution of major Archean-Paleoproterozoic BIF and VMS deposits (modified from Zhao et al. 2005); (b) Geological sketch map of the Qingyuan area showing Neoarchean pluton and supracrustal rocks together with post Archean sequences (modified from Shenyang Institute of Mineral Geology, 2006)

## 2 Geological background

The QGB is situated in the northern margin of the EB, covering an area of ~25,000 km<sup>2</sup> (Peng et al. 2015). It comprises Archean plutons (covering about 70% of the area) and supracrustal rocks, some of which are unconformable covered by Mesozoic sedimentary rocks and intruded by Neopaleozoic plutons as partly showing in Fig. 1b. The Neoarchean plutons in Qingyuan area were grouped into two major episodes by Wang et al. (2016) based on U-Pb isotopic data, the older ~2.56-2.53 Ga strongly gneissic quartz dioritic and tonalitic to trondhjemite gneisses series, and the younger ~2.52-2.49 Ga weakly gneissic to massive quartz monzodioritic and monzogranitic gneisses series. These plutons are present as domes and as irregularly shaped outcrops,

which control the distribution of greenstone units within the study area. Meanwhile, the Neoarchean supracrustal rocks were subdivided into three main assemblages from bottom to top mainly based on their lithologic association and metamorphic grade (Zhai et al. 1985; Shen et al. 1994): the Shipengzi Formation (SF) composed of tholeiitic to calc-alkalic meta-mafic volcanic rocks with some bimodal lithofacies and BIFs, the Hongtoushan Formation (HF) composed of meta-calc-alkaline bimodal volcanic rocks with VMS and minor BIFs, and the Nantianmen Formation (NF) composed of sedimentary lithofacies with lesser amount of tholeiitic to transitional meta-mafic volcanics and BIFs.

### 3 Results and Discussion

#### 3.1 Chronology

The analysed zircons can be divided into three groups according to its CL textures and Th/U values. Group I and Group II both are mostly subhedral to euhedral prismatic crystals with blurred oscillatory- or sector-zoning, but their Th/U ratios are different. The former possess a high Th/U ratio (average 0.63) and define an upper intercept age of  $2616.9 \pm 3.6$  Ma, whereas the latter have a moderate Th/U value (average 0.40) and yielded an upper intercept age of  $2565 \pm 7.8$  Ma. Group III are mostly subhedral prismatic crystals with fairy dark in colour and misty internal textures, their Th/U ratios are very low (average 0.07) and define an upper intercept age of  $2516.7 \pm 6.1$  Ma. Combined with previous geochronology (Zhu et al. 2015) in the QGB, we suggest that the  $2565 \pm 7.8$  Ma age is the formation age of these felsic metavolcanics, and also it represents the deposition age of the Xiadianzi BIF. In contrast, the older  $2616.9 \pm 3.6$  Ma age is the crystallization age of the inherited zircon, which indicates the existence of old crust in the Qingyuan area, the younger  $2516.7 \pm 6.1$  Ma age is similar to those metamorphic age presented by previous researcher (Wan et al. 2012).

#### 3.2 Petrochemical and Petrogenesis

The systematic stratigraphic variations in the trace elements geochemical characteristics of the QGB (Fig. 2 and Fig. 3) provide an optimized opportunity to decipher the petrogenesis of its volcanics. On the La/Sm vs. La/Ta diagram, all basalt samples show minimal contamination by continental materials (Fig. 4a), suggesting that they were formed by uncontaminated magma precursors. Among them, the geochemical features of groups I basalts are comparable to those of Mid-Ocean Ridge Basalts (MORB), which are further supported by the samples falling into the MORB field on the La/Nb vs. La and Th/Yb vs. Nb/Yb diagrams (Fig. 4b, c). Hence, the magmatic precursors of these rocks are inferred to have formed by the partial melting of depleted mantle, this inference are supported by their low  $(La/Sm)_N$  (average 1.3),  $(La/Yb)_N$  (average 1.4), Nb/Ta (average 16.4, primitive mantle 17.6) and Zr/Hf (average 34.5, primitive mantle 36) ratios.

Basalts samples from group II and group III all fall into

the IAB (island arc basalt) field on the La/Nb vs. La diagram (Fig. 4b). However, among them the group II basalts are characterized by slightly fractionated REE patterns and pronounced negative Nb anomalies, which closely compare with calc-alkaline island arc andesites-basalts. Similarly, on the Th/Yb vs. Nb/Yb diagram the group II basalts all plot in the calc-alkaline area within Cenozoic counterparts region (Polat et al. 2011), further supporting their genetic link with arc magmatism formed by slab dehydration and wedge melting. In contrast, group III basalts are characterized by unfractionated REE patterns, moderate negative Nb anomalies and devoid of pronounced HFSE anomalies, which are compositionally comparable to the typical primitive arc basalts (Hollings and Kerrich 2000). As a corollary, the group III basalts might source from partial melting of the sub-arc mantle wedge at high level, and accompanied by addition of limited fluids derived from subducted slab (Pearce and Parkinson 1993; Polat et al. 2011).

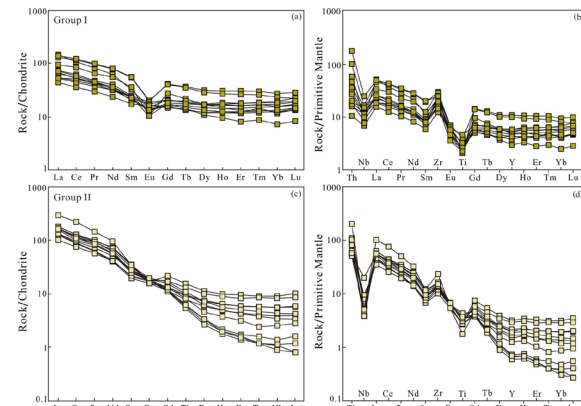


**Figure 2.** Chondrite-normalized REE diagrams and primitive mantle-normalized trace element diagrams for felsic rocks from the QGB (Normalizing values from Sun and McDonough, 1989)

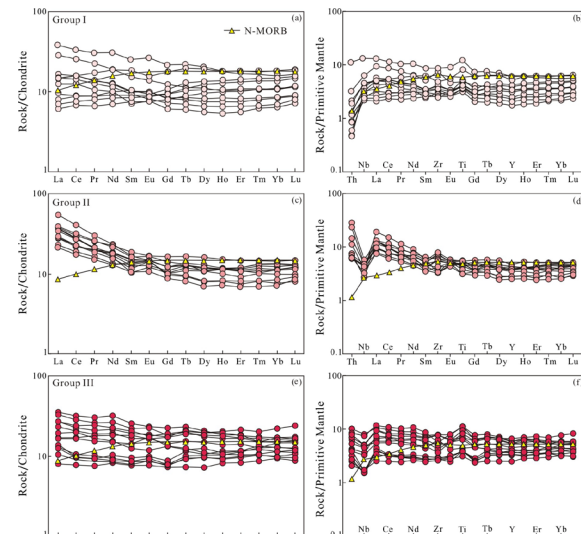


**Figure 3.** Chondrite-normalized REE diagrams and primitive mantle-normalized trace element diagrams for mafic rocks from the QGB (N-MORB and the normalizing values from Sun and McDonough, 1989)

The dominance of FII type felsic volcanic rocks (Group I, Fig. 5a, b) within the HF is consistent with a high-

temperature, medium pressure petrogenesis of partial melting at shallow (10-15 km perhaps) crustal levels with amphibole and plagioclase as residual mineral phases, as testified by the LREE-enriched REE patterns, high contents of HFSE and obviously negative Eu anomalies (Lesher et al. 1986) (Fig. 2a, b). While, group II felsic volcanics from bimodal volcanic sequence of the SF are characterized by high Zr/Y values (average 29.8), fractionated REE patterns ( $\text{La}/\text{Yb}_{\text{CN}} = 16.5\text{-}187.9$ ) and weakly negative to positive Eu anomalies (Fig. 2c, d), which are consistent with the typical features of FI type felsic volcanics, indicating that they might generate by low-degree partial melting of mafic source at high pressure ( $> 0.7 \text{ Gpa}$ ) with minimal fractionation (Lesher et al. 1986).

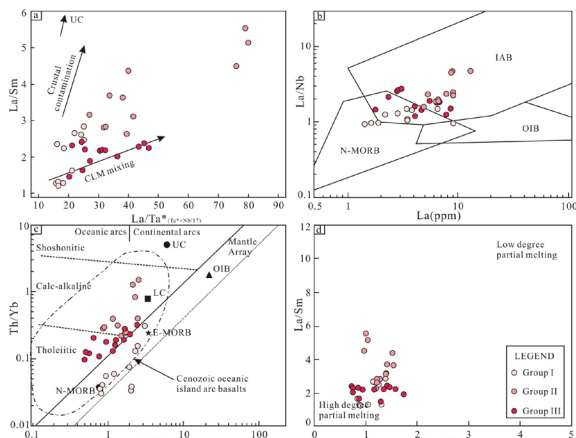


**Figure 4.** (a) Plot of La/Sm vs. La/Ta<sup>87</sup>-Nb<sup>87</sup> plot discriminant interaction of continental lithosphere mantle (CLM) versus contamination by continental crust; (b) La/Nb vs. La diagram distinguishing the tectonic setting for the magmatic precursors of all samples (after Li, 1993); (c) Th/Yb vs. Nb/Yb and (b) Zr vs. Ti diagram distinguishing the tectonic setting for the magmatic precursors of basalts (after Pearce, 2008; Angerer et al., 2013), the area of Cenozoic oceanic island arc basalts modified from Polat et al. (2011); (d) La/Sm vs. Gd/Yb diagram showing degree of partial melting

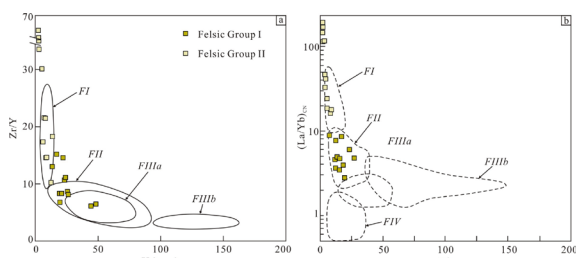


**Figure 5.** (a) Zr/Y vs. Y (ppm) diagram showing FI type affinities for the rhyodacites/dacites in the SF and FII type affinities in the HF (after Lesher et al., 1986); (b) La/YbCN vs. YbCN plot outlining the fields for FI-FIV types felsic volcanics (after Hart et al., 2004)

Collectively, considering the significant abundance of island arc basalts in the QGB and presence of numerous VMS deposits in the HF, a geodynamic setting characterized by arc rifting is favoured for the generation of these rocks: lithospheric extension in the overriding arc crust may have occurred in response to subducted slab rollback, causing rifting of the protoarc, and then the ascending of sub-arc mantle beneath the extensional arc may provide the heat source needed for the partial

melting process (Hart et al. 2004; Piercy 2011). Meanwhile, the subtle differences, such as lithofacies affinities and mineralization types, between the lower SF and the HF are likely attribute to the upwelling of underplated mafic magma beneath rifts into variable depths.

### 3.3 Tectonic evolution and mineralization

As documented earlier, the extensively exposed tholeiitic basalts (group III) with shallow negative Nb anomalies and transitional to calc-alkaline basalts (group II; the SF) with deeper negative Nb anomalies (Fig. 3) recorded the evolution from primitive arc to mature arc magmatism, while the stratigraphic younger sequences (the HF) composed of interlayered N-MORB type basalts (group I) with FI (group II) to FII (group I) felsic volcanics (Fig. 2, 3) are petrogenetic in response to rifting processes. Therefore, an extensional arc setting is proposed for the QGB, however, given the presence of slightly continental crust signatures, such as crustal contamination and xenocrystic zircons, in some supracrustal rocks the arc are more likely formed along the continental margin rather than intra-oceanic.

Based on an extensive database of compiled whole-rock geochemistry (Fig. 2, 3), U-Pb geochronology (not shown) and stratigraphic constraints, a simplified geodynamic scenario including the formation of an continental margin arc, the subsequent arc-rifting processes, and end of the extension is proposed for the formation of the SF, the HF and the NF in the QGB, respectively. The first stage is characterized by the generation of volume tholeiitic (group III) to calc-alkaline (group II) basalts in the lower most SF, it may reflect a gradual transition from depleted, weakly subduction altered to subduction metasomatized mantle melts (Manikyamba et al. 2015), because during early stage of subduction only limited flux generated by the dehydration process of oceanic slab, but as the increasement of subduction depth more transitional to calc-alkaline basalts occurred attesting to an increasing contribution from slab-derived fluid and/or melt (Stern 2002). Studies of the Phanerozoic island arc indicate that the magmatism can transform form primitive island arc to calc-alkaline just in a few million years (Jicha and Singer 2006), which is totally comparable with that of the QGB. The second stage is an extension-dominated geodynamic setting in which rifting of the continental margin arc, perhaps triggered by the subduction slab rollback, induced the thinning of overriding plate and the formation of numerous normal faults (e.g., synvolcanic and synsedimentary faults), which would increase the permeability for fluid flow and provided an accommodation space for upwelling mantle melts to occupy, thereby elevated the geothermal gradient of the rift (e.g., Schardt et al. 2005; Piercy et al. 2011). These processes, in the end would provide the necessities for generation and evolution of sub-sea floor hydrothermal systems. Convection of seawater through mafic crust leached large quantities of elements (i.e., sulfur, copper, zinc, iron, lead, and gold), deposition of these elements as sulfides and/or ferric oxyhydroxides on the seafloor in

certain environment generated the VMS and BIF in the QGB. Finally, the last stage is characterized by the presence of dominated sedimentary rocks, such as marble, quartzite and minor BIF in the upper NF (Zhang 2014), which may represent termination of the extension process and the following sedimentation.

## Acknowledgements

This research was financially supported by the National Natural Science Foundation of China (No. 41572076).

## References

- Bekker A, Slack JF, Planavsky N, Krapež B et al (2010) Iron formation: the sedimentary product of a complex interplay among mantle, tectonic, oceanic and biospheric processes. *Econ Geol* 105:467–508
- Franklin JM, Gibson HL, Galley AG, Jonasson IR (2005) Volcanogenic massive sulfide deposits. *Econ Geol* 100th Anniversary Volume. pp 523–560
- Hollings P, Kerrich R (2000) An Archean arc basalt-Nb-enriched basalts-adakite association: the 2.7 Ga confederation assemblage of the Birch-Uchi greenstone belt, Superior Province. *Contrib Mineral Petr* 139:208–226
- Hart TR, Gibson HL, Lesher CM (2004) Trace element geochemistry and petrogenesis of felsic volcanic rocks associated with volcanogenic massive Cu-Zn-Pb sulfide deposits. *Econ Geol* 99:1003–1013
- Houston DL, Logan GA (2004) Barite, BIFs and bugs: evidence for the evolution of the Earth's early hydrosphere. *Earth Planet Sc Lett* 220:41–55
- Jicha BR, Singer BS (2006) Volcanic history and magmatic evolution of Seguam Island, Aleutian Island arc, Alaska. *Geol Soc Am Bull* 118:805–822
- Li SG (1993) Ba–Nb–Th–La diagrams used to identify tectonic environments of ophiolite. *Acta Petrologica Sin* 9:146–157 (in Chinese with English abstract)
- Lentz D, Goodfellow W (1992) Re-evaluation of the petrochemistry of felsic volcanic and volcanioclastic rocks near the Brunswick no. 6 and 12 massive sulfide deposits, Bathurst mining camp, New Brunswick: Geological Survey of Canada Paper. pp 343–350
- Lodge RWD, Gibson HL, Stott GM, Franklin JM, Hamilton MA (2014) Geodynamic Reconstruction of the Winston Lake Greenstone Belt and VMS Deposits: New Trace Element Geochemistry and U-Pb Geochronology. *Econ Geol* 109:1291–1313
- Manikyamba C, Ganguly S, Santosh M, Saha A, Chatterjee A, Khelen AC (2015) Neoarchean arc-juvenile back-arc magmatism in eastern Dharwar Craton, India: Geochemical fingerprints from the basalts of Kadiri greenstone belt. *Precambrian Res* 258:1–23
- Mitjavila JM, Martí J, Soriano C (1997) Magmatic evolution and tectonic setting of the Iberian pyrite belt volcanism. *J Petrol* 38:728–755
- Mercier-Langevin P, Gibson HL, Hannington M, Goutier J, Monecke T, Dubé B, Houle MG (2014) A Special Issue on Archean Magmatism, Volcanism, and Ore Deposits: Part 2. Volcanogenic Massive Sulfide Deposits. *Econ Geol* 109:1–9
- Pearce JA, Parkinson IJ (1993) Trace element models for mantle melting to volcanic arc petrogenesis. In: Prichard HM, Alabaster T, Harris NBW, Neary CR (Eds.), *Magmatic Processes and Plate Tectonics: Geological Society Special Publication*. pp 373–403
- Piercey SJ (2011) The setting, style, and role of magmatism in the formation of volcanogenic massive sulfide deposits. *Miner Deposita* 46:449–471
- Polat A, Appel PWU, Fryer B (2011) An overview of the geochemistry of Eoarchean to Mesoarchean ultramafic to mafic volcanic rocks, SW Greenland: Implications for mantle depletion and petrogenetic processes at subduction zones in the early Earth. *Gondwana Res* 20:255–283
- Peng P, Wang C, Wang XP, Yang SY (2015) Qingyuan high-grade granite-greenstone terrain in the Eastern North China Craton: root of a Neoarchaean arc. *Tectonophysics* 662:7–21
- Sun SS, McDonough WF (1989) Chemical and isotopic systematics of oceanic basalts: implication for mantle composition and processes. In: Saunders AD, Norry MJ (Eds.), *Magmatism in Ocean Basins*, 42. Geological Society of London, Special Publication. pp 313–345
- Shen BF, Luo H, Han GG, Dai XY, Jin WS, Hu XD, Li SB, Bi SY (1994) Archean Geology and Mineralization of Northern Liaoning and Southern Jilin Province. Geological Publishing House, Beijing. pp 1–255 (in Chinese)
- Stern RJ (2002) Subduction zones. *Rev Geophys* 40:1–42
- Schardt C, Yang J, Large R (2005) Numerical heat and fluid-flow modeling of the Panorama volcanic-hosted massive sulfide district, Western Australia. *Econ Geol Bull Soc Econ Geol* 100:547–566
- Shenyang Institute of Mineral Geology, China. 2006. The map of geology and mineral resources at 1/200,000 scale in the Qingyuan area. Scientific Report (in Chinese)
- Slack JF, Grenne T, Bekker A, Rouxel OJ, Lindberg PA (2007) Suboxic deep seawater in the late Paleoproterozoic: Evidence from hematitic chert and iron formation related to seafloor-hydrothermal sulfide deposits, central Arizona, USA. *Earth Planet Sc Lett* 255:243–256
- Wu KK, Zhao GC, Sun M, Yin CQ, He YH, Tam PY (2013) Metamorphism of the northern Liaoning Complex: implications for the tectonic evolution of Neoarchean basement of the Eastern Block, North China Craton. *Geosci Front* 4:305–320
- Wan YS, Dong CY, Xie HQ, Wang SJ, Song MC, Xu ZY, Wang SY, Zhou HY, Ma MZ, Liu DY (2012) Formation ages of early Precambrian BIFs in the North China Craton: SHRIMP zircon U-Pb dating. *Acta Geol Sin* 86:1448–1478 (in Chinese with English abstract)
- Wang W, Liu SW, Cawood PA, Bai X, Guo RR, Guo BR, Wang K (2016) Late Neoarchean subduction-related crustal growth in the Northern Liaoning region of the North China Craton: evidence from ~2.55 to 2.50 Ga granitoid gneisses. *Precambrian Res* 281:200–223
- Zhai MG, Yang RY, Lu WJ, Zhou JE (1985) Geochemistry and evolution of the Qingyuan Archean granite-greenstone terrain, NE China. *Precambrian Res* 27:37–62
- Zaleski E, Peterson VL (1995) Depositional Setting and Deformation of Massive Sulfide Deposits, Iron-Formation and Associated Alteration in the Manitouwadge Greenstone Belt, Superior Province, Ontario. *Econ Geol* 90:2244–2261
- Zhao GC, Sun M, Wilde SA, Li SZ (2005) Late Archean to Paleoproterozoic evolution of the North China Craton: key issues revisited. *Precambrian Res* 136:177–202
- Zhang YJ (2014) Formation, evolution and metallogenesis of granite-greenstone belt in Qingyuan, Liaoning province (Doctor thesis). Changchun: Jilin University. pp 1–228 (in Chinese)
- Zhu MT, Zhang LC, Dai YP, Wang CL (2015) In situ zircon U-Pb dating and O isotopes of the Neoarchean Hongtoushan VMS Cu-Zn deposit in the North China Craton: Implication for the ore genesis. *Ore Geol Rev* 67:354–367

# Crustal architecture of the south-east Superior Craton

David R. Mole, Jeffrey H. Marsh, Phil Thurston, John A. Ayer

Mineral Exploration Research Centre (MERC), Harquail School of Earth Sciences and Goodman School of Mines, Laurentian University, Canada

Balz S. Kamber

Queensland University of Technology, Earth Environment and Biological Sciences, Australia

**Abstract.** The Neoarchean Abitibi sub-province of the south-east Superior Craton represents one of the most mineralized pieces of crust on Earth. Rich in both orogenic gold and base metal (Cu, Zn, Pb) VMS deposits, but relatively poorly endowed in komatiite-hosted Ni-Cu-PGE systems, the region appears to have a different mineral systems story to its Neoarchean counterpart; the Yilgarn Craton in Western Australia. Large-scale isotopic mapping using Sm-Nd and Lu-Hf systems have proven useful in understanding the large-scale cratonic architecture that controls metal endowment in the Yilgarn, and hence a major component of the Metal Earth project is to produce similar mapping products for the Superior Craton. Initial results from a small Lu-Hf dataset demonstrate a clear spatial variation in  $\epsilon_{\text{Hf}}$  across the Ontario Abitibi region. The area as a whole is juvenile, but small variations within these data correspond to east-west trending zones of relatively more- or less-juvenile crust. The occurrence of VMS systems and orogenic gold deposits correlate with the most juvenile zones, while the edge of these zones correlate with major structures important for mineralization, such as the Porcupine-Destor Fault. These observations suggest that crustal architecture has a fundamental large-scale control on regional metal endowment in the Abitibi sub-province.

## 1 Introduction

Lithospheric and crustal architecture – the framework of major tectonic blocks, terranes and their boundaries – represent a fundamental first-order control on major geological systems, including ore deposits and the location of world-class mineral camps. Existing work has demonstrated the ability of radiogenic isotope systems (i.e. Sm-Nd, Lu-Hf) to constrain time-resolved intra-cratonic lithospheric architecture. Champion and Cassidy (2007) used regional Sm-Nd isotopic data to map the crustal architecture of the Yilgarn Craton, while Mole et al. (2013) and Huston et al. (2014) demonstrated the association between that lithospheric architecture and BIF-hosted iron, orogenic gold, and komatiite-hosted Ni-Cu-PGE systems.

Those results demonstrated the underlying control of lithospheric-crustal architecture and the potential for isotopic mapping as a greenfields area selection tool. Further work by Mole et al. (2014), using Lu-Hf isotopes, demonstrated that the technique could account for rocks, events, and mineral systems of different ages, showing how Ni-Cu-PGE mineralized komatiite systems of the

Yilgarn Craton migrated with the changing lithospheric boundary (craton margin) from 2.9 to 2.7 Ga.

Beyond mineral systems science, the data collected in these studies allow a time-space assessment of craton construction and evolution, which provide vital information on the tectonic environment/s active on the Archean Earth.

Despite the increasing prevalence and use of the isotopic mapping technique in China (Hou et al. 2015) and West Africa (Parra-Avila et al. 2017), it is yet to be applied across the Earth's largest Archean craton – the Superior.

## 2 Isotopic mapping of the Superior Craton: the craton-scale module of Metal Earth

In the Superior Craton, the isotopic mapping technique has been applied locally to the Wabigoon region by Lu et al. (2013) and Bjorkman (2017), but information from other regions is currently sparse, or has not be collated to produce a spatial product. A primary goal of the new Metal Earth project at Laurentian University is to apply this technique to the entire Superior Craton, producing a craton-wide Lu-Hf isotopic map that will be used to: (1) Understand the development and evolution of the craton; (2) evaluate the spatial variability in magmatism and metal endowment; and (3) be available as an area selection tool for large-scale exploration activities.

## 3 Methodology

The isotopic mapping of the Superior Craton will be approached in an incremental method. The craton has been sub-divided into six main zones, based on geology, geography, and administration. Each zone is approached individually, with integration between zones as the project progresses. Samples are selected from a new, in-house geochronology database that contains the location of all current Superior zircon geochronology samples; all are felsic volcanics or granitoid rocks, which represent a physical sample of the Archean crust. These samples are then located in the relevant archive and sub-sampled. Once mounted and imaged, zircons undergo oxygen isotope analyses by secondary ion mass spectrometry (SIMS) at the Centre for Isotopic Microanalysis (CCIM) at the University of Alberta, before laser-ablation inductively-coupled plasma mass spectrometry (LA-ICP-MS) for U-Pb geochronology, Lu-Hf isotopes, and zircon trace element analyses at the Minerals Exploration

Research Centre Isotope Geochemistry Laboratory (MERC-IGL). The first zone to undergo this method is the south-east Superior, and data collection is on-going. The initial data presented here are solution ICP-MS zircon data provided by John Ayer and Balz Kamber.

#### 4 Early results from the south-east Superior Craton

The south-east Superior Craton comprises the Quetico, Abitibi, Opatica, and Wawa subprovinces, and thereby some of the most well-mineralised crust on Earth, with the Abitibi producing >180 Moz of Au alone (Spooner and Barrie 1993).

Initial results from the Ontario portion of the Abitibi are displayed in Figures 1 and 2. Figure 2 shows the variation in  $\epsilon$ Hf across this area of crust. This is essentially a time-slice of crustal architecture at 2740–2670 Ma, i.e. during

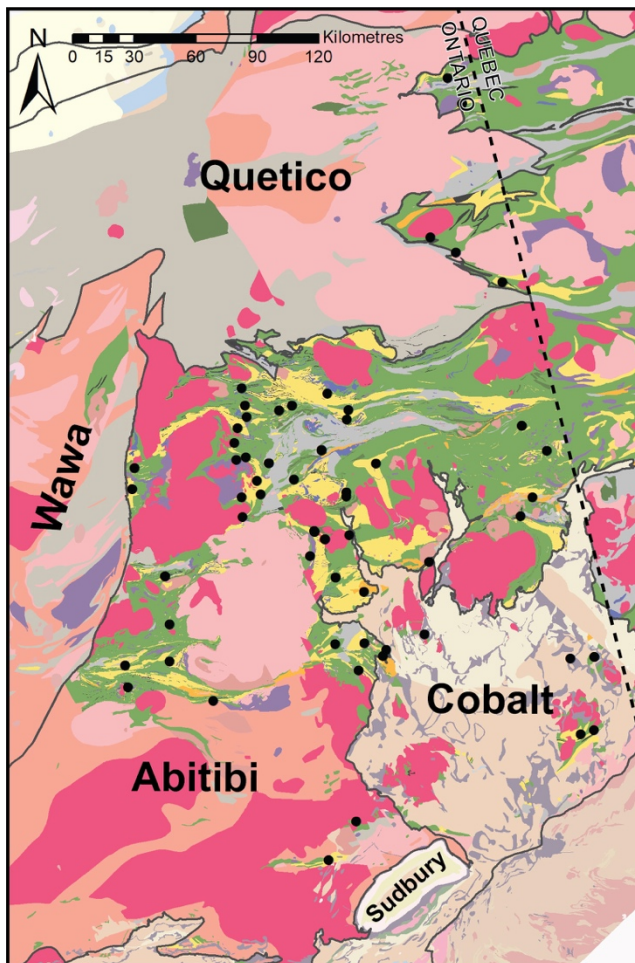


**Figure 1.** Geological map and location of Hf-isotope samples (black circles). Location of map is at the south-east corner of the Superior Craton. Shades of pink represent TTG-granitoid rocks, green = mafic rocks, yellow = felsic volcanics.

the development of the major Abitibi volcanic sequences from the 2750–2735 Ma Pacaud Assemblage to the Upper Blake River (2701–2695 Ma) and syn-sedimentary Porcupine and Timiskaming Assemblages. As we collect

more data, we will look to further define time-slices around major magmatic events (Thurston et al. 2008).

The first observation is that all the crust in this region of the south-east Superior is juvenile (Figures 2–3). All data fall between +5 and +2  $\epsilon$ Hf units, with no data below the chondrite uniform reservoir line (CHUR). This suggests that the crust of the Abitibi region has a short residence time. A number of interpretations are possible: (1) if the crust was extracted from a depleted mantle (DM) that corresponded to the DM model line (Figure 3), then it is possible an older element of the crust is 3100 Ma, and that this element may have mixed with younger crust between 2740–2670 Ma, resulting in the scatter in the  $\epsilon$ Hf plot; (2) the data may represent newly-extracted crust which was extracted from a DM that was less radiogenic than the model DM line, in which case any DM model ages (two-stage) would not be accurate; (3) hypotheses one and two could be correct, but also involve an older crustal element not represented here due to dilution within a mixing system dominated by the juvenile crust.

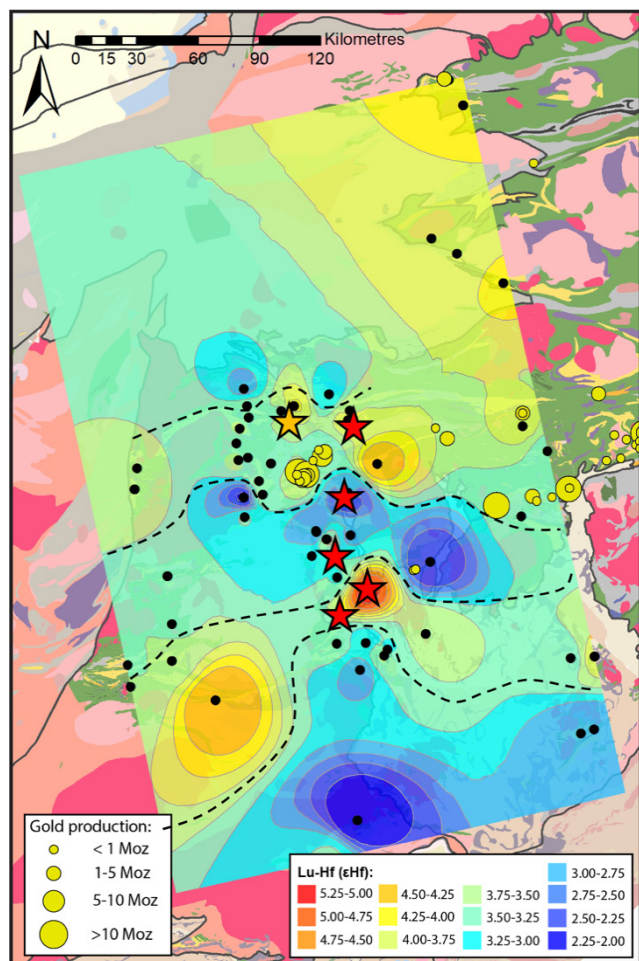


**Figure 2.** Contour map of Hf-isotope data (shown as  $\epsilon$ Hf). Gold deposits, Kidd-Creek VMS (yellow star) and komatiite-hosted Ni-Cu-PGE deposits (red stars) are shown. Black dashed lines are interpreted east-west linear isotopic zones. The  $\epsilon$ Hf group interval is based upon the analytical error, at 0.25 epsilon units (zircon solution ICP-MS data).

Given the lack of zircon xenocrysts >2.9 Ga and the lack of any older component in existing Hf and Nd datasets (Corfu and Noble 1992), we suggest that the crust of the Abitibi represents either very young ca. 2.7 Ga ‘primary’ crust (two-stage evolution to felsic crust) extracted from a depleted mantle that is less radiogenic than the current DM model; or that the crust has a slightly older, 3.1-2.9 Ga component, that would still be relatively juvenile at 2.7 Ga (Figure 3).

The spatial representation of these data in Figure 2 show a series of east-west trending isotopic zones of slightly different isotopic character. The regions of ‘hotter’ colours are ca. +5 to +3.5  $\epsilon$ Hf, whilst the ‘cooler’ regions are ca. +3.25 to +2 Ga. If we assume this crust was extracted from a model DM, then the cooler regions would represent ca. 3.1 Ga crust, and the hotter regions ca. 2.9 Ga material.

Interestingly, the northern-most juvenile isotopic zone hosts the major gold camps, including Timmins and Kirkland Lake, as well as the Kidd Creek and Kirkland Lake VMS systems. The komatiite-hosted Ni-Cu-PGE systems appear to form a north-south trend that is normal to the isotopic zoning and not constrained to a particular zone, or type of zone.

The Au systems appear to prefer the southern region of this zone, which corresponds spatially to the Porcupine-Dester Fault (PDF), suggesting the edges of the isotopic zones have structural representatives. The southern juvenile zone is currently poorly constrained, but additional data will aim to constrain if the margins of this zone correspond to the highly prospective Cadillac-Larder-Lake Fault (CLLF). The komatiite-hosted Ni-Cu-PGE systems appear to be aligned with the margin of the Wawa sub-province to the west, suggesting this may have a control on the location of these systems, such as that observed in the Yilgarn (Mole et al. 2014). However, at this stage the isotopic dataset is too small to evaluate this hypothesis.

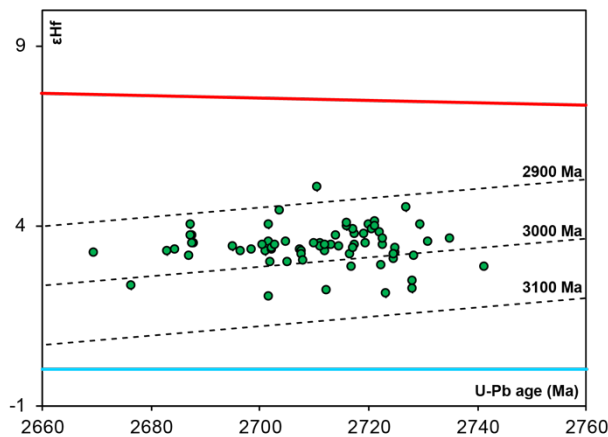


**Figure 3.** Age vs  $\epsilon$ Hf plot for felsic volcanic and granitoid rocks shown in Figures 1-2. The 2-sigma analytical error is 0.25 epsilon units. The depleted mantle line is in red, CHUR is in blue.

A number of tectonic-scale processes may have formed the east-west isotopic zones and corresponding crustal architecture:

1. Rift-basin architecture, where the highly-juvenile

zones represent grabens of thin, hot crust, and the relatively less-juvenile zones horsts of cooler crust. Within this interpretation, the less juvenile crust also could be slightly older, 3.1 Ga pre-existing crust rifted by a later, ca. 2.7 Ga magmatic period.

2. The isotopic zones may represent accreted ribbon continents and/or island arcs, each with a different character and crustal history. However, long-lived (<2760 Ma?) shared magmatic events across these zones do not support this;
3. Within a complex vertical tectonic regime, with crustal overturns and ‘drip’-style tectonics in operation (Nebel et al. 2018; Wiemer et al. 2018), reworking within overthickened mafic crust may result in spatial  $\epsilon$ Hf variations depending on the age of the reworked crust and geometry of a ‘drip’.

Our preferred interpretation at this stage is that the  $\epsilon$ Hf architecture in Figure 2 represents a rift basin similar to that in the Basin and Range province (Eaton 1982). This environment facilitated the formation of the VMS systems in the Abitibi and set-up the gold-rich source regions, prior to late compression, granitoid intrusion, and gold mineralizing events at <2.7 Ga.

This may suggest a rift- or extension-dominated volcanic evolution between ca. 2740-2690 Ma, followed by a brief period of ‘late’ subduction which drove compression, granitoid formation, basin formation (deposition of Porcupine and Timiskaming sediments), and ultimately orogenic gold mineralization. However, a possible alternative for late subduction could be the internal reworking of the 2740-2690 Ma greenstone sequence, to produce TTG, and reworking of existing TTG to form granitoids (Johnson et al. 2017; Bédard 2006; Sizova et al. 2015). This process would form basins and drive sedimentation processes, with late far-field compression driving the establishment of the final, current structural architecture. Further, detailed upcoming work is planned to try to address the tectonic setting for the south-east Superior Craton, and the role of subduction and/or any alternative tectonic processes.

## 5 Conclusions

Initial results from the isotopic mapping program of the Metal Earth project show a number of important features:

- The spatial distribution of crustal  $\epsilon$ Hf data reconcile a number of east-west zones of differing isotopic character; all are juvenile but some are more juvenile (+5 to +3.5) than others (+3.25 to +2);
- The more juvenile zones correlate with the occurrence of VMS and orogenic gold systems, and the edge of the zones correspond to major structures associated with gold prospectivity;
- These relationships are consistent with those constrained in the Yilgarn Craton;
- Together, these data suggest an intimate relationship between architecture, crustal history, and endowment, which can be mapped using the

- $\epsilon$ Hf data;
- The tectonic processes driving the formation of this architecture are controversial, and require more integrated information to differentiate. However, we suggest that the isotopic map captures a broad period of rifting, forming the east-west isotopic zones in a horst-and-graben -like environment, allowing the autochthonous greenstone formation observed across the Abitibi.
- This dataset represents a fragment of that being developed as part of Metal Earth's isotopic mapping project. Work is ongoing to look in more detail at time-resolved architectural evolution within the 2740-2670 Ma period in order to separate out the various events vital in the formation and establishment of this world-class mineral system.
- ## Acknowledgements
- This is contribution number MERC-ME-2019-170 of the Metal Earth project, hosted by the Mineral Exploration Research Centre (MERC) at Laurentian University, Canada. The project is funded by the Canada First Research Excellence Fund. We thank our partners at the Geological Survey of Canada, Ontario Geological Survey, and Ministère de l'Énergie et des Ressources naturelles (MERN). The assistance of the Jack Satterly Geochronology Laboratory at the University of Toronto and Geotop at University of Quebec at Montreal (UQAM) are much appreciated. We thank our collaborators at the Canadian Centre for Isotopic Microanalysis (CCIM) at University of Alberta, whom acquire our O-isotopes in zircon via SIMS.
- ## References
- Bédard JH (2006) A catalytic delamination-driven model for coupled genesis of Archaean crust and sub-continental lithospheric mantle. *Geochimica et Cosmochimica Acta* 70:1188-1214. doi: 10.1016/j.gca.2005.11.008.
- Bjorkman K (2017) 4D crust-mantle evolution of the Western Superior Craton: Implications for Archean granite-greenstone petrogenesis and geodynamics. University of Western Australia.
- Champion DC, Cassidy KF (2007) An overview of the Yilgarn Craton and its crustal evolution In: Bierlein FP, C.M. K-R (eds) Proceedings of Geoconferences (WA) Inc Kalgoorlie '07 Conference. Geoscience Australia Record 2007/14, Kalgoorlie, Western Australia, pp 8-13.
- Corfu F, Noble SR (1992) Genesis of the southern Abitibi greenstone belt, Superior Province, Canada: evidence from zircon Hf isotope analyses using a single filament technique. *Geochimica et Cosmochimica Acta* 56:2081-2097.
- Eaton GP (1982) The Basin and Range province: Origin and tectonic significance. *Annual Review of Earth and Planetary Sciences* 10:409-440.
- Hou Z, Duan L, Lu Y, Zheng Y, Zhu D, Yang Z, Yang Z, Wang B, Pei Y, Zhao Z (2015) Lithospheric architecture of the Lhasa terrane and its control on ore deposits in the Himalayan-Tibetan orogen. *Economic Geology* 110:1541-1575.
- Huston DL, Champion DC, Cassidy KF (2014) Tectonic controls on the endowment of Neoarchean cratons in volcanic-hosted massive sulfide deposits: evidence from lead and neodymium isotopes. *Economic Geology* 109:11-26.
- Johnson TE, Brown M, Gardiner NJ, Kirkland CL, Smithies RH (2017) Earth's first stable continents did not form by subduction. *Nature*.
- Lu Y-j, McCuaig TC, Hollings P, Ketchum K, Kerrich R, Smyk M, Cliff J, Bagas L (2013) Zircon multi-isotopic mapping in Wabigoon Subprovince, western Superior Craton: Implications for lithospheric architecture and controls on orogenic gold mineral systems. *Proceedings, 12th Biennial Meeting, Society For Geology Applied To Mineral Deposits*, pp 1148-1151.
- Mole D, Fiorentini M, Cassidy K, Kirkland C, Thebaud N, McCuaig T, Doublier M, Duuring P, Romano S, Maas R (2013) Crustal evolution, intra-cratonic architecture and the metallogeny of an Archaean craton. *Geological Society, London, Special Publications* 393:SP393. 398.
- Mole DR, Fiorentini ML, Thebaud N, Cassidy KF, McCuaig TC, Kirkland CL, Romano SS, Doublier MP, Belousova EA, Barnes SJ (2014) Archean komatiite volcanism controlled by the evolution of early continents. *Proceedings of the National Academy of Sciences* 111:10083-10088.
- Nebel O, Capitanio F, Moyen J-F, Weinberg R, Clos F, Nebel-Jacobsen Y, Cawood P (2018) When crust comes of age: on the chemical evolution of Archean, felsic continental crust by crustal drip tectonics. *Phil Trans R Soc A* 376:20180103.
- Parra-Avila LA, Belousova E, Fiorentini ML, Eglinger A, Block S, Miller J (2017) Zircon Hf and O-isotope constraints on the evolution of the Paleoproterozoic Baoulé-Mossi domain of the southern West African Craton. *Precambrian Research*.
- Sizova E, Gerya T, Stüwe K, Brown M (2015) Generation of felsic crust in the Archean: A geodynamic modeling perspective. *Precambrian Research* 271:198-224.
- Spooner ET, Barrie CT (1993) A special issue devoted to Abitibi ore deposits in a modern context; preface. *Economic Geology* 88:1307-1322.
- Thurston P, Ayer J, Goutier J, Hamilton M (2008) Depositional gaps in Abitibi greenstone belt stratigraphy: A key to exploration for syngenetic mineralization. *Economic Geology* 103:1097-1134.
- Wiemer D, Schrank CE, Murphy DT, Wenham L, Allen CM (2018) Earth's oldest stable crust in the Pilbara Craton formed by cyclic gravitational overturns. *Nature Geoscience* 11:357.

# Isotopic and geochemical indicators on volcanic-hosted massive sulfide prospectivity: a review

David L Huston, David C Champion and Michael P Doublier  
Geoscience Australia

**Abstract.** Well-mineralized Neoarchean volcanic-hosted massive sulfide (VHMS) provinces are characterized by rhyolites with specific geochemical features and juvenile radiogenic isotope signatures. Although well-mineralized Paleoproterozoic provinces share many similar characteristics, the signatures of fertile Phanerozoic provinces differ. These temporal changes not only have implications for the use of geochemical fertility signatures during VHMS exploration, but also for the secular evolution of tectonic process and metallogenesis. The changes in VHMS fertility indicators may relate to the change from unstable shallow slab break-off to stable deep break-off (modern-style) subduction during the Neoproterozoic.

## 1 Introduction

Black smokers, the modern analogue of volcanic-hosted massive sulfide (VHMS) deposits, presently form along mid-oceanic ridges and convergent margins, including back-arc settings (Hannington et al., 2005). Of these two settings, the former is highly likely to be destroyed by subsequent subduction, leaving the latter the dominant tectonic setting in which ancient VHMS deposits are preserved. The distribution of black smokers (Hannington et al., 2005) indicates that ancient VHMS deposits should be present in back-arc basins and rifted arcs that form above the subduction channel. Although a broad convergent margin setting is the main environment for VHMS formation, some ancient convergent margins appear to be better mineralized than others, raising the question as to whether better-mineralized can be distinguished from poorly-mineralized VHMS provinces using geological, geochemical and/or geophysical data.

A number of types of geochemical data have been used to distinguish better-mineralized VHMS provinces, including whole-rock rhyolite geochemistry, and the lead and neodymium characteristics of the province hosting the deposits (Lesher et al., 1986; Huston et al. 2005). These disparate signals probably reflect the tectonic environment in which the deposits form. Importantly, the geochemical characteristics of well-mineralized provinces change through time: well-mineralized Archean and Paleoproterozoic provinces have different geochemical and isotopic characteristics to well-mineralized Phanerozoic provinces. These changes probably relate to the evolution of tectonic processes through geological time.

The purpose of this contribution is to review geochemical and isotopic characteristics indicative of highly mineralized provinces and how these characteristics have changed through time, and then use

these observations and models of secular variations in tectonic processes to develop an overall model which points to how geochemical characteristics could be used in exploration for VHMS deposits.

## 2 Geochemical indicators of VHMS potential

The pioneering study by Lesher et al. (1986) indicated that the geochemistry of high field strength and rare earth elements (REE) from rhyolites can be used to determine the potential of the host package to contain VHMS deposits. Lesher et al. (1986), who worked exclusively on Neoarchean deposits, grouped rhyolites into four categories (types F1 to FIIIa; Fig. 1), of which two, FIIIa and FIIb, had the highest potential to host VHMS deposits. Subsequent workers have largely confirmed the original results of Lesher et al. (1986), with some important wrinkles.

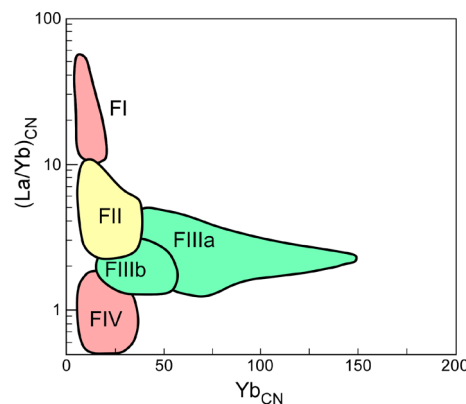
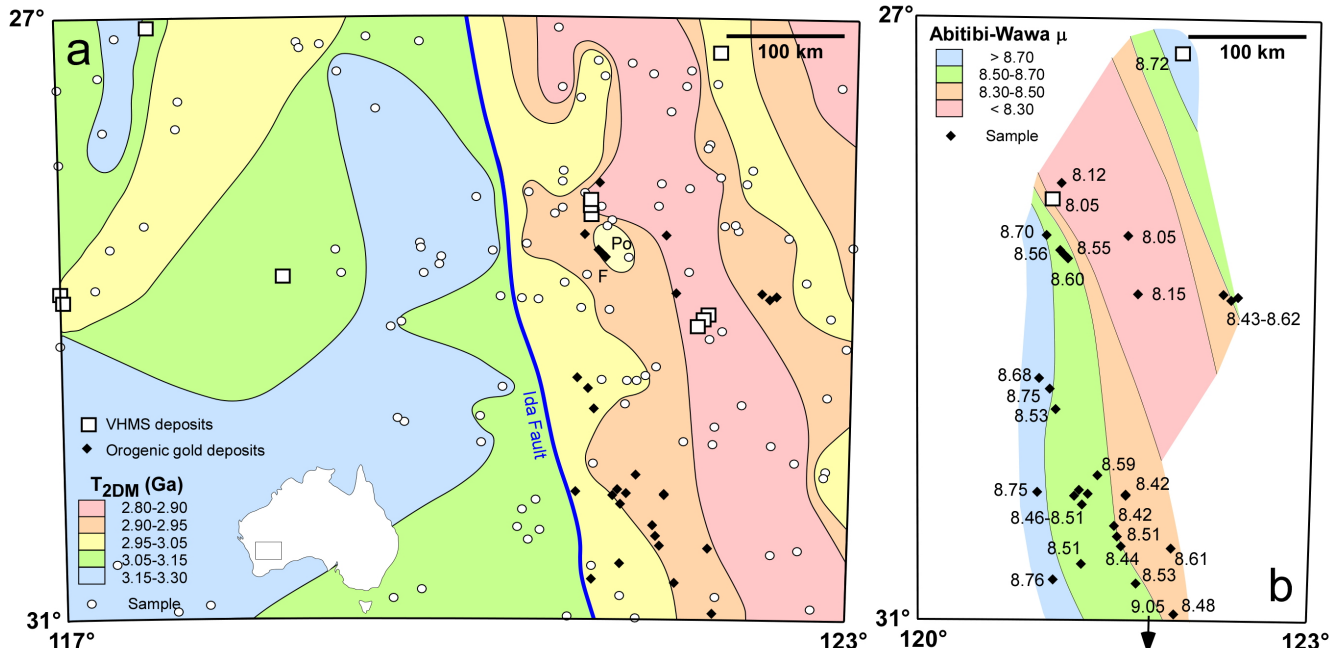


Figure 1.  $\text{La}/\text{Yb}_{\text{CN}}$  versus  $\text{Yb}_{\text{CN}}$  diagram showing the rhyolite types of Lesher et al. (1986) and Hart et al. (2004).

Hart et al. (2004) found that the geochemical characteristics of rhyolites in fertile host packages changed with time: although the characteristics of most fertile Archean and Paleoproterozoic packages were broadly similar, fertile packages in Phanerozoic provinces were dominated by FII and FIV, the latter a new rhyolite type not noted in the signatures of Archean (or Paleoproterozoic) provinces by Lesher et al. (1986). Moreover, Mercier-Langevin et al. (2007) noted that the host to the precious metal-rich, Neoarchean Bousquet district was dominated by F1 rhyolites, indicating that some Neoarchean districts, in this case containing high-sulfidation VHMS deposits, do not fit the results of Lesher et al. (1986). Other precious-metal rich deposits that formed on thicker crust, such as the Nimbus deposit in the Yilgarn Craton (Hollis et al. 2017), also do not fit with in the classification of Lesher et al. (1986).



**Figure 2.** Maps showing variations in the northern Yilgarn Craton for (a) Nd model ages ( $T_{2\text{DM}}$ ) of granites and (b)  $\mu$  values determined from lead isotope measurements from mineral deposits using the Abitibi-Wawa lead isotope evolution model of Thorpe et al. (1992). The diagram is modified after Huston et al. 2014).

The changes in REE geochemistry used by Lesher et al. (1986) and Hart et al. (2004) as VHMS fertility indicators relate to presence or absence of garnet in the source regions of the rhyolitic melts (e.g. Rollinson 1993), which in turn is related to the pressure (depth) at which melting occurs (e.g. Zhang et al. 2013). The geochemistry of FIIa and FIIb rhyolites, which are fertile in the Neoarchean and Paleoproterozoic, indicates high temperature, shallow melting in the absence of garnet in the crust, whereas the geochemistry of FII rhyolites, which are most prospective in the Phanerozoic, and, particularly, FI rhyolites are indicative of deeper melting in the presence of garnet. This suggests that the depth of melting for VHMS-fertile rhyolites has increased with geological time, and that rhyolites associated with high-sulfidation VHMS deposits may have been sourced from a greater depth than “normal” VHMS deposits.

Barrie (1995) found zircon saturation temperatures, which are calculated from rhyolite geochemical data, are also indicative of VHMS fertility. Fertile volcanic packages have higher zircon saturation temperatures than less-fertile packages. The results of Barrie (1995) were based solely on Neoarchean districts, so potential secular changes in the indicator are not known.

### 3 Radiogenic isotope indicators of VHMS potential

Huston et al. (2005, 2014: Fig. 2) first noted that more fertile VHMS provinces were associated with juvenile crust as indicated by variations in granite Nd model ages (e.g. Champion and Cassidy 2008) and  $\mu$  values ( $^{238}\text{U}/^{204}\text{Pb}$ ) calculated from ore lead isotope data. Highly mineralized terranes (e.g. Abitibi-Wawa Subprovince,

southeastern Canada), and more strongly mineralized zones within less mineralized provinces (e.g. Teutonic Zone in Eastern Goldfields Superterrane, and Cue Zone in Youanmi Terrane, Western Australia) have granite Nd model ages close to emplacement ages and/or low  $\mu$  values (Fig. 2). In general, juvenile Archean provinces are more fertile for VHMS deposits than more evolved provinces (Fig. 3). This general relationship also applies to Paleoproterozoic provinces, but not to Phanerozoic provinces, where highly mineralized VHMS provinces are commonly present in more evolved crust (e.g. Mount Read Volcanics, Tasmania, Australia).

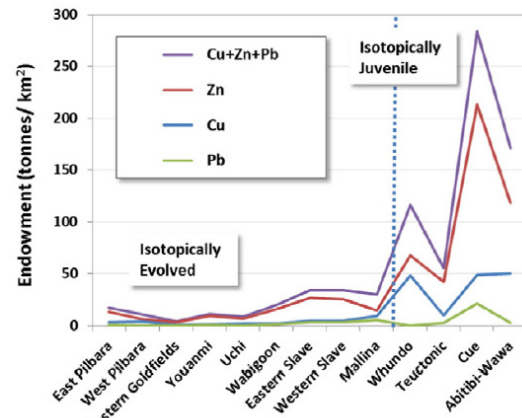


**Figure 3.** Plot of Cu, Zn, Pb and combined Cu-Pb-Zn VHMS metal endowment (in tonnes of metal/km<sup>2</sup>) for Archean cratonic blocks in Canada and Australia, highlighting the much greater endowment in isotopically primitive blocks (after Champion and Huston 2016).

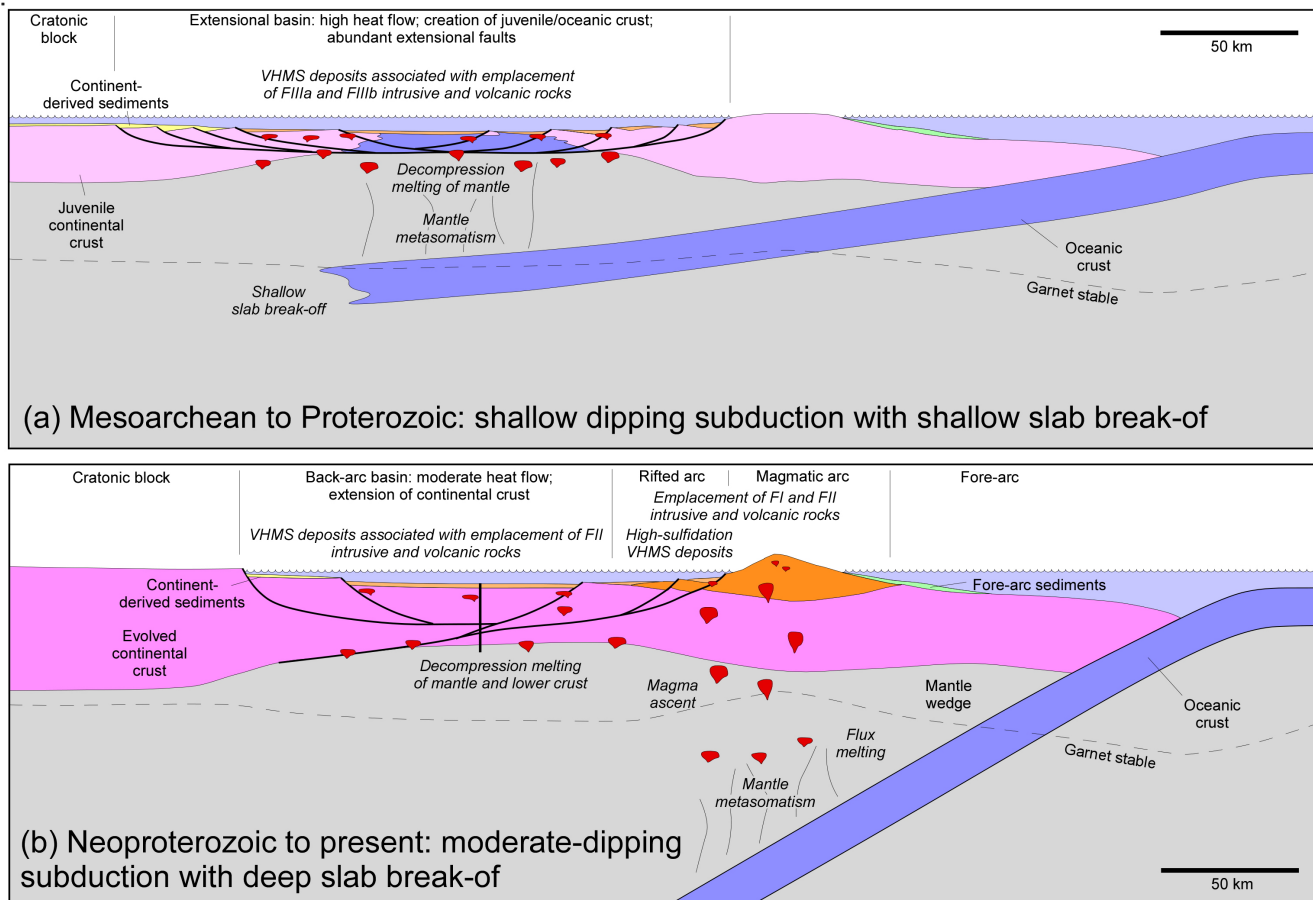


**Figure 4.** Possible changes in tectonic style and volcanic-hosted massive sulfide deposit formation between (a) Neoarchean-Paleoproterozoic and (b) late Neoproterozoic-Phanerozoic times.

#### 4 Volcanic-hosted massive sulfide fertility indicators in a tectonic context

Disparate geochemical data sets have been used to infer the fertility of volcanic successions for VHMS deposits. In most cases these fertility indicators were developed in Neoarchean VHMS provinces, and later research has indicated that indicators have changed through time, with the greatest changes between the Paleoproterozoic and Phanerozoic.

The style of tectonics also appear to have changed through geological time as a consequence of mantle cooling from some form of stagnant lid regime in the Paleoarchean through shallow slab break-off subduction in the Mesoarchean through the mid-Neoproterozoic to modern-style deep slab break-off subduction from the mid-Neoproterozoic to now (Sizova et al. 2010; Moyen and van Hunen 2012). Moreover, the style and, particularly, the duration of metallogenesis along convergent margins (Huston et al. 2018) has also changed, with Neoarchean to Paleoproterozoic margins characterized by a shorter duration of metallogenesis (<200 Myr) than those in the Phanerozoic (400-700 Myr). These changes in tectonic setting, metallogenesis and VHMS fertility indicators may be linked.

Figure 4 illustrates a model that accounts for changes in VHMS indicators between the Neoarchean-

Paleoproterozoic and Phanerozoic as a consequence of changes in tectonics. In this model, subduction during the Neoarchean to Paleoproterozoic (Fig. 4a) is unstable due to repeated (and shallow) slab break-off, leading to relatively short periods of subduction and convergent-margin metallogenesis. Possibly, due to the shallow dip of subduction, arcs may not form. In contrast, from the late Neoproterozoic onwards (Fig. 4b), subduction is characterized by generally coherent and often steeper slab dips and is more stable with consistent development of volcanic arcs. This leads to significantly longer periods of subduction, with a greater flux of hydrated oceanic crust and eroded continental crust into the subduction channel, and also to a cooler environment in the subduction zone (Brown 2014). The cooler environment leads to melting at greater depths, commonly in the garnet present zone, leading to the formation of a greater association of VHMS deposits with type FII and FIV volcanics. Moreover, the introduction of greater amounts of evolved crustal material in the subduction channel along with greater crustal thicknesses lead to a breakdown in the relationship between juvenile crust and VHMS deposits seen in older deposits.

## 5 Summary, implications for exploration and future research

The review presented above suggests that although there appear to be reasonably reliable geochemical indicators of VHMS fertility at the province- to district-scale, these indicators appear to change with geological time. This means that caution needs to be exercised in applying the techniques during exploration; in particular the age of the mineralization must be considered.

The development of micro-analytical geochemical and isotopic techniques, including the geochemistry and isotopic composition of zircon, offers new opportunities to develop fertility indicators. These techniques have been developed for porphyry copper exploration (e.g. Dilles et al. 2015) and can be potentially adapted for VHMS exploration.

## Acknowledgements

The authors acknowledge the input of our collaborators, both past and present, who have influenced our thoughts over the years. The collaborators include Kevin Cassidy, Bruce Eglington, Sally Pehrsson, Steve Piercy and Shen-Su Sun. Roger Skirrow and Steve Hollis are thanked for their reviews. This contribution is published with permission of the Chief Executive Officer of Geoscience Australia.

## References

- Barrie CT (1995) Zircon thermometry of high-temperature rhyolites near volcanic-associated massive sulfide deposits, Abitibi subprovince, Canada. *Geology*:169-172
- Brown M (2014) The contribution of metamorphic petrology to understanding lithosphere evolution and geodynamics. *Geoscience Frontiers* 5: 553-569
- Champion DC, Huston DL (2016) Radiogenic isotopes, ore deposits and metallogenic terranes: Novel approaches based on regional isotopic maps and the mineral systems concept. *Ore Geol Rev* 76:229–256
- Champion DC, Cassidy KF (2008) Using geochemistry and isotopic signatures of granites to aid mineral systems studies: an example from the Yilgarn Craton. *Geoscience Australia Record* 2008/09:7–16
- Dilles JH, Kent AJR, Wooden JL, Tosdal RM, Koleszar A, Lee RG, Farmer LP (2015) Zircon compositional evidence for sulfur-degassing from ore-forming arc magmas. *Econ Geol* 110:241–251
- Hart TR, Gibson HL, Lesher, CM (2004) Trace element geochemistry and petrogenesis of felsic volcanic rocks associated with volcanogenic massive Cu-Zn sulfide deposits. *Econ Geol* 99:1003-1013
- Hollis SP, Yeats CJ, Wyche S, Barnes SJ, Ivanic TJ (2017) VMS mineralization in the Yilgarn Craton, Western Australia: a review of known deposits and prospectivity analysis of felsic volcanic rocks. *Geol Sur Western Austr Rep* 166
- Huston DL, Champion DC, Cassidy KF (2005) Tectonic controls on the endowment of Archean cratons in VHMS deposits: evidence from Pb and Nd isotopes. In *Mineral Deposit Research: Meeting the Global Challenge*. Springer, Berlin Heidelberg, pp 15–18
- Huston DL, Champion DC, Cassidy KF (2014) Tectonic controls on the endowment of Neoarchean cratons in volcanic-hosted massive sulfide deposits: evidence from lead and neodymium isotopes. *Econ Geol* 109:11–26
- Huston DL, Doublier MP, Champion DC (2018) Can mineral deposit assemblages be used to infer tectonic settings in the Archean? *Resourcing Future Generations Abstracts*
- Lesher CM, Goodwin AM, Campbell IH, Gorton MP (1986) Trace-element geochemistry of ore-associated and barren, felsic metavolcanic rocks in the Superior Province, Canada: Can J Earth Sci 23:222–237
- Mercier-Langevin P, Dubé B, Hannington MD, Richer-Laflèche M, Gosselin G (200). The LaRonde Penna Au-rich volcanogenic massive sulfide deposit, Abitibi Greenstone Belt, Quebec: Part II. lithogeochemistry and paleotectonic setting. *Econ Geol* 102:611-631
- Moyen, J-F, van Hunen J (2012) Short-term episodicity of Archaean plate tectonics. *Geology* 40:451-454.
- Rollinson H (1993) *Using geochemical data: evaluation, presentation, interpretation*. New York, John Wiley and Sons, 352 p
- Sizova E, Gerya T, Brown M, Perchuk LL (2010) Subduction styles in the Precambrian: Insight from numerical experiments. *Lithos* 116:209-229
- Zhang C, Holtz F, Koepke J, Wolff PE, Ma C, Bédard JH (2013) Constraints from experimental melting of amphibolite on the depth of formation of garnet-rich restites, and implications for models of Early Archean crustal growth. *Precam Res* 231:206-217

# Does heat matter? Magmatism and metallogeny in the IPB: assessment of future mineral exploration vectors

André Cravinho, Jorge MRS Relvas

Instituto Dom Luiz, Faculdade de Ciências, Universidade de Lisboa, Portugal

Rita Solá, Igor Morais, Luis Albardeiro, João X Matos, Rute Salgueiro, Daniel de Oliveira

Laboratório Nacional de Energia e Geologia / Centro de Estudos Geológicos e Mineiros do Alentejo, Portugal

Nelson Pacheco

Somincor-Lundin Mining, Castro Verde, Portugal

**Abstract.** The Iberian Pyrite Belt (IPB) is historically considered one of the most important VHMS (felsic-siliciclastic) provinces worldwide. Moreover, its seven deposits currently in operation represent the most important base-metal producers in Western Europe. Notwithstanding, the number of massive and/or stringer sulfide intersections in the province is currently declining and, thus, new exploration vectors must be developed for new deposits to be found, probably at greater depths. Traditional approaches to brownfield VHMS exploration focuses mostly on detecting any geophysical and/or geochemical features possibly related to massive sulfide orebodies, but the understanding of the relation between these ore-forming systems and heat sources is still poorly constrained and can potentially prove to be critical in defining regional and/or local target areas for VHMS exploration. This on-going research project uses the Neves-Corvo deposit as a case-study and aims to constrain the relationships between petrogenesis and metallogeny, in order to assess which petrogenetic conditions, timings, and thermal evolution of the felsic volcanism are more prone to trigger and sustain high-temperature hydrothermal systems and, hence, VHMS formation, and/or to provide direct magmatic metal contributions.

## 1 Introduction

Heat is one of the most critical components of hydrothermal systems: it has a crucial role in controlling metal solubility, transport and metal deposition, and is paramount in the development of thermal gradients, which are the effective drivers of sustained crustal-scale fluid flow processes responsible for the formation of mineral deposits, such as volcanic-hosted massive sulfide deposits (VHMS). These deposits are important base-metal sources that can be classified into five categories, based on the geodynamic setting and/or hosting lithostratigraphic sequence (e.g. Barrie and Hannington 1997). Nevertheless, the relation between these deposits and magmatism has been proved to be, in most cases, unquestionable. Magmatism provides not only the heat source to trigger and sustain hydrothermal circulation and ore forming processes but can also act as an important metal source (e.g. Huston et al. 2011).

One of the most important VHMS provinces worldwide is the Iberian Pyrite Belt (IPB), which hosts nearly 90

deposits, seven of them in operation, providing the most important EU base-metal supply. In this felsic-siliciclastic province, despite the variety of sulfide depositional environments recognized, with some deposits exhibiting hybrid genetic features between sediment-hosted and volcanic-hosted massive sulfides, the large majority are undoubtedly associated with felsic volcanic rocks (Tornos 2006), as in other felsic-siliciclastic VHMS provinces.

VHMS deposits exploration, at a regional and local scale, in the IPB and elsewhere, commonly relies in the use of geophysical methods and the detection of the typical hydrothermal alteration patterns related to mineralization. Nevertheless, in the IPB and other brownfield provinces, the rate of deposit discoveries is decreasing and, although these methodologies keep being of inestimable value, the challenge is to seek for new additional exploration tools able to find deeper orebodies. Thus, new exploration criteria need to be developed, in order to maintain or even increase the EU's contribution of base-metals in the future.

This project aims to understand how magmatism and volcanism impact (temperature-wise) ore-forming systems and the formation of massive sulfide deposits. Its major goal is to establish a more complete relationship between the orebodies and their likely heat sources, and, ultimately, to develop new regional exploration criteria, able to distinguish productive from barren volcanic axes and cycles, by using the Neves-Corvo ore-forming system as a case-study.

## 2 Geological background

### 2.1 Iberian Pyrite Belt

The oblique collision between the South Portuguese Zone (SPZ) and the Ossa Morena Zone (OMZ) led to the closure of the Rheic ocean during the Variscan orogeny resulted in a local transtensive tectonic setting, generating a series of pull apart elongated basins infilled by a siliciclastic-dominated lithostratigraphic sequence (Tornos et al. 2005, 2006). This infill constitutes one of the most important tectonostratigraphic domains of the SPZ.

The most important lithostratigraphic unit is the Volcanic-Sedimentary Complex (VSC), characterized by a bimodal volcanic suite, which hosts all the VHMS orebodies. The VSC outcropping sequences suggest that

felsic volcanism largely dominates, but geophysical surveys indicate that mafic counterparts can be more significant at depth (Tornos et al. 2005).

The IPB deposits occur associated to felsic volcanic rocks (e.g. Tornos et al. 2006), and thus, this spatial and temporal association has long been interpreted as reflecting a genetic relationship with felsic magmatism and used in exploration. Nevertheless, no direct correlations between the metallogenetic and the petrogenetic constraints and signatures have been established so far.

## 2.2 The Neves-Corvo deposit

The Neves-Corvo deposit is one of the giant VHMS deposits in the IPB and one of the seven active mines in this district. It is composed of seven, unusually Cu-, Zn- and Sn-rich deposits found in the SE termination of the Rosário antiform. As in other sectors of the IPB, at the Neves-Corvo area the tectonically imbricated lithostratigraphic sequence includes (from bottom to top) i) the Phyllite Quartzite group (PQG), composed mostly of a more than two km thick sequence of metagraywacke and shale/schists, whose top is dated from the upper Famennian (base unknown); ii) the VSC, comprising a variably thick (usually less than 600m thick) metasedimentary-dominated sequence, with dark shales and other mudstone-siliciclastic rocks, ranging from the Upper Famennian up to the Visean, with two important sedimentary hiatuses – one corresponding to the Tournasian, and another one dated from the early Visean; iii) the synorogenic Baixo Alentejo Flysch Group (BAFG) composed of turbiditic and other gravity-driven deposits, often more than 2 km thick.

The orebodies are hosted by the lower VSC sequence, mostly comprising felsic explosive and effusive volcanic rocks and dark-shales dated from the Upper Famennian (Oliveira et al. 2004, Rosa et al. 2008, Solá et al. 2015).

Although the gross metal budget of the Neves-Corvo orebodies formed as typical IPB VHMS ore-forming system, the unusually high tonnages, metal grades and ratios, and radiogenic signatures reflect a unique metallogenetic evolution, involving different metal and fluid sources, in time and space, including the typical IPB ore-fluid and metal sources, local magmatic-hydrothermal contributions and tectonometamorphic remobilisations (e.g. Relvas et al. 2001, 2006). Ore-forming systems must have been especially effective in this area, and abundant data has been gathered for the Neves-Corvo deposit (the best-known deposit in the IPB), making this deposit an excellent case-study to address the relationship between magmatism and metallogeny.

## 3 Petrogenesis of felsic volcanic rocks and VHMS exploration

Besides contributing with metals and fluids, magmatism plays a critical and more general role in the formation of VHMS deposits it acts as the heat source. Crustal thermal gradients, triggered by the shallow emplacement of crustal-derived felsic melts or mantle-derived mafic

magmas, promote crustal-scale hydrothermal circulation and consequently the formation of massive sulfide deposits. Several authors have proposed that estimating melt temperatures using zircon saturation temperatures can provide important regional and/or local criteria for VHMS exploration, namely at the Abitibi and the IPB felsic-siliciclastic provinces (e.g. Barrie 1995; Codeço et al. 2018), where “higher-temperature” rhyolitic melts are more prone to trigger, sustain and host hydrothermal systems and VHMS deposits. Furthermore, lithgeochemistry data has been also proposed as regional criteria for VHMS exploration (e.g. Hart et al. 2004), focusing essentially on the petrogenetic processes and the classification of the felsic rocks that more often host VHMS deposits: FII, FIIIa and FIIIb rhyolites are more commonly the hosts of VHMS deposits and their petrogenetic processes considered ideal to trigger hydrothermal circulation and mineralization processes.

### 3.1 Neves-Corvo and other IPB sectors

Numerous studies have focused on the geochemistry and petrogenesis of the (sub)volcanic rocks in the IPB (e.g. Munhá 1983, Mitjavilla et al. 1997). Presently, it is widely accepted that mafic rocks are the result of partial melting of a heterogeneous mantle source and their emplacement at shallower (upper-crustal) depths triggered crustal melting and the formation of felsic melts from which the calc-alkaline felsic volcanic suites derive. These suites range from dacites to (high-silica) rhyolites, interpreted as the result of differential partial melting rates (Mitjavilla et al. 1997). Minor intermediate rocks (andesitic-like) are also recognized in the IPB, resulting from the mixture between felsic and mafic melts.

A compiled local (Neves-Corvo) and regional (mineralized and apparently barren IPB sectors) lithgeochemistry database ( $n=99$  and  $334$ , respectively; references of the regional data in Codeço et al. 2018) show that both the hanging-wall and footwall felsic volcanic rocks in the Neves-Corvo area are altogether similar to those commonly found throughout the IPB, classified as FII and minor FIIIa rhyolites to dacites (Fig. 1A). Moreover, when inspecting the calculated zircon saturation temperatures ( $T_{\text{SatZirc}}$ ; Fig. 2) for the various mineralized (e.g. Neves-Corvo, Aljustrel, Rio Tinto) and barren sectors (e.g. Ervidel-Roxo), it is clear that: 1) the temperature range for the IPB is similar to those of the Abitibi greenstone belt (Barrie 1995); and, 2) although several “groups” can be divided considering their median and average  $T_{\text{SatZirc}}$  temperatures, some mineralized sectors are clearly characterized by lower  $T_{\text{SatZirc}}$  temperatures than some barren sectors, and vice-versa.

Furthermore, the samples do not show geochemical evidences of intense hydrothermal and/or regional alteration. Hence, significant mass-changes are not expected and absolute Zr contents (for  $T_{\text{SatZirc}}$  calculations) should not be biased (Fig. 1B).

Another noteworthy feature is the discrepancy between calculated  $T_{\text{SatZirc}}$  temperatures and the so far published Ti-in-zircon temperatures in the IPB, which are significantly higher (for detailed comparison see Codeço et al. 2018).

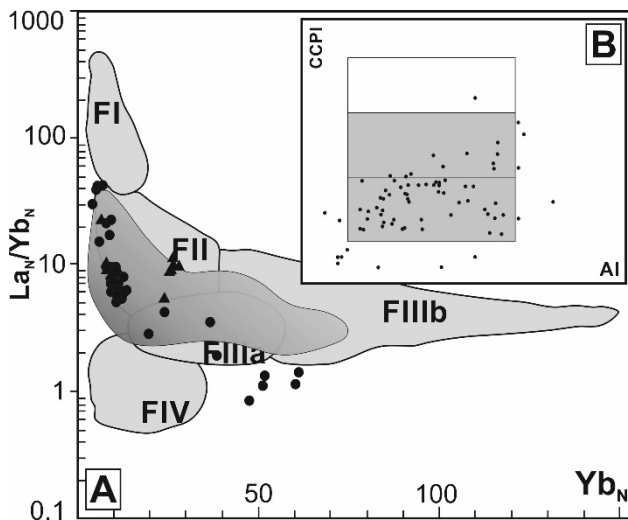


**Figure 1.** A.  $\text{La}_N/\text{Yb}_N$  vs  $\text{Yb}_N$  plot from Hart et al. (2004) and database samples: shaded area corresponds to the regional IPB database (Albernoa, Erveld-Roxo, Aljustrel, Lagoa Salgada, Lousal, Rio Tinto and Aznalcóllar); circles represent footwall and triangles hanging-wall samples. B. AI vs CCPI alteration indices; grey areas represent the dacitic and rhyolitic least-altered box areas.

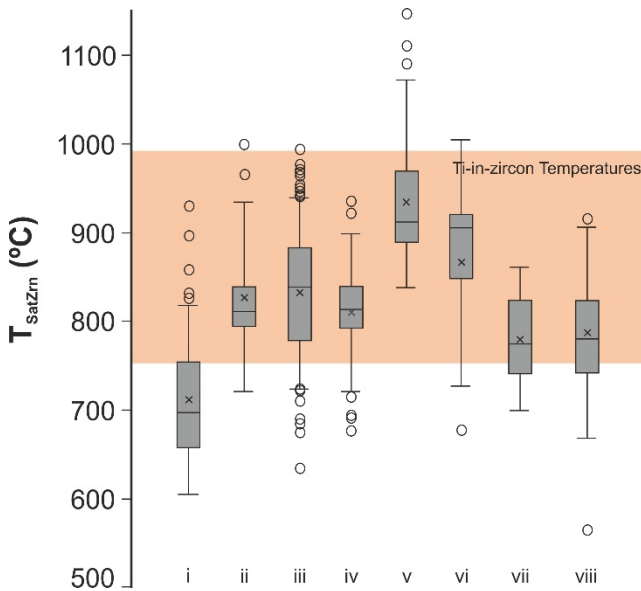


**Figure 2.** Calculated  $T_{\text{SatZirc}}$  for some mineralized and barren IPB sectors following the approach of Boehnke et al. (2013) (samples from: i. Albernoa; ii. Roxo; iii. Aljustrel; iv. Lagoa Salgada; v. Neves-Corvo; vi. Lousal; vii. Rio Tinto; and viii. Aznalcóllar; 90% of data within each box, black line and cross represent median and average values, respectively). All samples with  $\text{SiO}_2 > 60 \text{ wt\%}$  and  $1 < M < 1.9$ . Ti-in-zircon temperatures from Codeço et al. (2018).

Hence, if overall all the sectors show potential to host VHMS deposits, are zircon saturation temperatures real “temperatures” and useful to evaluate potential heat sources and VHMS deposit “productivity”? And can they be useful as exploration vectors?

#### 4 Zircon saturation temperature – is it a real geothermometer?

The development and review of zircon saturation models

(Watson and Harrison, 1983, Boehnke et al. 2013) had tremendous impact in the understanding of magmatic systems. Recent reviews (e.g. Siégele et al. 2018) have shown that, although these models have been widely interpreted as real “geothermometers”, the calculated temperature data must be carefully interpreted. Once the estimation of the M factor and Zr contents are based in the whole-rock geochemical composition, the calculated  $T_{\text{SatZirc}}$  values only represent the temperature at which a specific melt, with a specific composition (the lithogeochemical input data), starts to precipitate zircon. Hence,  $T_{\text{SatZirc}}$  should not be considered a magmatic geothermometer but a theoretical variable intrinsic to the magmatic evolution process (see Siégele et al. 2018). For  $T_{\text{SatZirc}}$  data to be reliable as a geothermometer for volcanic rocks, it should be applied to rocks with bulk-rock compositions similar to the melts from which zircon grew, and, ideally, glassy (if altered, alteration must be accounted) and almost phenocryst-free rocks, with autocrystalline zircon grains (Hanchar and Watson 2003). Furthermore, for correctly interpreting such temperatures, a detailed geochronological characterization is required examining the relative amount of autocrystalline, antecrystalline and xenocrystic zircon. This is not the case for the previously mentioned works, and hence, the proposals assume that all Zr contents derive from autocrystalline zircon, precipitated from melts with a similar composition to that of the volcanic rock, surely biasing and overestimating temperatures.

Thus, if  $T_{\text{SatZirc}}$  does not prove to be a reliable magmatic geothermometer, it should not be considered a useful criterion for VHMS exploration, and other methodologies for studying the thermal evolution of these crustal melts must be envisaged.

#### 5 Thermal evolution of felsic melts: future approaches and possible implications for VHMS mineral exploration

The fact that zircon saturation temperatures alone should not be used as valid criteria for calculating the temperature evolution of specific volcanic suites, hence assessing the productivity of specific melts as favourable heat sources for triggering and sustaining hydrothermal systems, does not imply that considering the overall petrogenetic processes and thermal evolution of crustal melts for the development of VHMS exploration criteria cannot be considered. When combined geochronology, other zircon- and other mineral-based data (e.g. rutile, quartz) can be used to better constrain the petrogenesis and thermal evolution of volcanic rocks.

A possible approach is to use Ti-in-zircon (Watson et al. 2006; Ferry and Watson 2007) to constrain the melt temperature during zircon crystallization. This approach is even enhanced when combined with U-Pb data, tracking temperature evolution within the magmatic system and the life-span of felsic plutonic to subvolcanic systems. This data integration must be made carefully, as zircon-based temperatures give only information regarding crystallization temperatures, and so, information regarding subsequent temperature changes

can only be inferred interpolating the obtained data from different time intervals. Even when state-of-the-art equipment or analytical techniques are used, the combination of geochronology and Ti-in-zircon data does not provide distinction between continuous long-lived magmatic systems and episodic, multi-staged short-pulses of melts, as analytical uncertainties (in dating) are usually too big (Kent and Cooper 2018). This has critical implications for the understanding of thermal evolution of igneous systems and, hence, for the heat supply in ore-forming hydrothermal systems, sometimes providing reliable information, useful for mineral exploration. Other geothermometers that allow to constrain temperature evolution in magmatic systems are the Zr-in-rutile (Watson et al. 2006) and/or Ti-in-quartz (Wark and Watson 2006). The latter is often used for the interpretation of the time-scale and temperature estimation of magmatic and hydrothermal systems (e.g. Audétat 2013, Codeço et al. 2017), and can prove to be useful as quartz phenocrysts are relatively common in felsic volcanic rocks, possibly offering a way of estimating temperatures and/or pressures in subvolcanic settings.

The variety of volcanic rocks in the Neves-Corvo area (and in the IPB) must reflect different petrogenetic processes. Thus, a comprehensive and complete petrogenetic model for the volcanic rocks of Neves-Corvo, integrating geochronology and thermochronology, is envisaged as a possible major contribution to a better understanding of the metallogenesis of this fascinating deposit and outstanding province. Different thermal evolutions should be assessed and since these magmatic events were conceivably largely responsible for the heat supply, they should be related with the corresponding metallogenetic processes. In this sense, this project aims to develop new mineralogical, geochemical and isotopic exploration criteria, relating heat sources, hydrothermal systems and formation of VHMS deposits in the IPB.

## Acknowledgements

A. Cravinho has been awarded with a PhD scholarship funded by Fundação para a Ciência e Tecnologia (FCT) (PD/BD/142784/2018), under the scope of the Earth Systems Doctoral Program - Instituto Dom Luiz (IDL). The research project is funded by SOMINCOR-LUNDIN Mining. Publication supported by FCT- project UID/GEO/50019/2019 - Instituto Dom Luiz, and EXPLORA/Op.ALT20-03-0145-FEDER-000025 Project, funded by Alentejo2020/Portugal2020 + European Regional Development Fund/ERDF.

## References

- Audétat A (2013) Origin of Ti-rich rims in quartz phenocrysts from the Upper Bandelier Tuff and the Tunnel Spring Tuff, southwestern USA. *Chem Geol* 360:99–104.
- Barrie CT, Hannington MD (1997) Classification of Volcanic-Associated Massive Sulphide Deposits Based on Host-Rock Composition. In: Barrie, CT and Hannington MD (eds) *Volcanic-Associated Massive Sulphide*.pp 1–11.
- Barrie CT (1995) Zircon thermometry of high-temperature rhyolites near volcanic-associated massive sulfide deposits, Abitibi subprovince, Canada. *Geology* 23:169–172.
- Boehnke P, Watson EB, Trail D, Harrison TM, Schmitt AK (2013) Zircon saturation re-revisited. *Chem Geol* 351:324–334.
- Codeço M, Mateus A, Figueiras J, Gonçalves L, Rodrigues P (2018) Development of the Ervedel-Roxo and Figueirinha-Albernoa volcanic sequences in Iberian Pyrite Belt, Portugal: metallogenetic and geodynamic implications. *Ore Geol Rev* 98:80–108.
- Codeço MS, Weis P, Trumbull RB, Pinto F, Lecumberri-Sánchez P, Wilke FDH (2017) Chemical and boron isotopic composition of hydrothermal tourmaline from the Panasqueira W-Sn-Cu deposit, Portugal. *Chem Geol* 468:1–16.
- Ferry JM, Watson EB (2007) New thermodynamic models and revised calibrations for the Ti-in-zircon and Zr-in-rutile thermometers. *Cont Miner Petrol* 154:429–437.
- Hanchar JM, Watson EB (2003) Zircon Saturation Thermometry. *Rev Min Geochim* 53:89–112.
- Hart TR, Gibson HL, Lesher CM (2004) Trace element geochemistry and petrogenesis of felsic volcanic rocks associated with volcanogenic massive Cu-Zn-Pb sulfide deposits. *Econ Geol* 99:1003–1013.
- Huston DL, Relvas JMRS, Gemmell JB, Drieberg S (2011) The role of granites in volcanic-hosted massive sulphide ore-forming systems: an assessment of magmatic-hydrothermal contributions. *Miner Deposita* 46:473–507.
- Kent AJR and Cooper KM (2018) How well do zircons record the thermal evolution of magmatic systems? *Geology*, 46:111–114.
- Mitjavilla J, Martí J, Soriano C (1997) Magmatic Evolution and Tectonic Setting of the Iberian Pyrite Belt Volcanism. *J Petrol* 38:727–755.
- Munhá J (1983) Hercynian magmatism in the Iberian Pyrite Belt. In: Sousa MJL & Oliveira JT (eds) *The Carboniferous of Portugal, Memorias Serviços Geológicos de Portugal* 29:39–81.
- Oliveira, JT, Pereira Z, Carvalho P, Pacheco N, Korn D (2004) Stratigraphy of the tectonically imbricated lithological succession of the Neves Corvo mine area, Iberian Pyrite Belt, Portugal. *Miner Deposita* 39:422–436.
- Relvas JMRS, Barriga FJAS, Ferreira A, Noiva PC, Pacheco N, Barriga G, (2006) Hydrothermal alteration and mineralization in the Neves-Corvo volcanic-hosted massive sulfide deposit, Portugal: I. Geology, mineralogy, and geochemistry. *Econ Geol* 101:791–804.
- Relvas JMRS, Tassinari CCG, Munhá J, Barriga FJAS (2001) Multiple sources for ore-forming fluids in the Neves Corvo VHMS Deposit of the Iberian Pyrite Belt (Portugal): strontium, neodymium and lead isotope evidence. *Miner Deposita* 36:416–427.
- Rosa JPC, McPhie J, Relvas JMRS, Pereira Z, Oliveira T, Pacheco N (2008) Facies analyses and volcanic setting of the giant Neves Corvo massive sulphide deposit, Iberian Pyrite Belt. *Miner Deposita* 43:449–466.
- Siegel C, Bryan SE, Allen CM, Gust DA (2018) Use and abuse of zircon-based thermometers: A critical review and a recommended approach to identify antecrustic zircons. *Earth Sci Rev* 176:87–116.
- Solá, AR, Salgueiro R, Pereira Z, Matos JX, Rosa C, Araújo V, Neto R, Lains JA (2015) Time span of the volcanic setting of the Neves-Corvo VHMS deposit. X Congresso Ibérico de Geoquímica/XVII Semana de Geoquímica abs 120–123.
- Tornos F, Casquet C, Relvas JMRS (2005) 4: Transpressional tectonics, lower crust decoupling and intrusion of deep mafic sills: a model for the unusual metallogenesis of SW Iberia. *Ore Geol Rev* 27:133–163.
- Tornos F (2006) Environment of formation and styles of volcanogenic massive sulfides: The Iberian Pyrite Belt. *Ore Geol Rev* 28:259–307.
- Wark DA, Watson EB (2006) TitaniQ: a titanium-in-quartz geothermometer. *Contrib Mineralog Petrol* 152:743–754.
- Watson EB, Harrison TM (1983) Zircon saturation revisited: temperature and composition effects in a variety of crustal magma types. *Earth Planet Sci Lett* 64:295–304.
- Watson EB, Wark DA, Thomas JB (2006) Crystallization thermometers for zircon and rutile. *Contrib Mineralog Petrol* 151:413–433.

# Unravelling the geochemistry of dark-grey to black metapelites in the Iberian Pyrite Belt (Portugal): the relation to massive sulphide ores

Filipa Luz & António Mateus

Dep. Geologia & IDL, Faculdade de Ciências, Univ. de Lisboa, Lisboa, Portugal

**Abstract.** Volcanogenic massive sulphide deposits in the Iberian Pyrite Belt can be linked with the deposition and evolution of fine-grained siliciclastic sediments represented by dark-grey to black metapelites. We present a lithogeochemical study of 60 samples from the Aljustrel and Neves Corvo mines and exploration drill holes in the Portuguese IPB segment. Geochemical fingerprinting of these dark-grey to black metapelites allow us to discriminate barren from altered/mineralized samples using the ratios  $\text{Al}_2\text{O}_3/(\text{Al}_2\text{O}_3+\text{Fe}_2\text{O}_3+\text{MnO})$ ,  $\text{Fe}_2\text{O}_3/\text{TiO}_2$ ,  $(\text{As}+\text{Sb})/\text{Sc}$ ,  $(\text{Cu}+\text{Zn}+\text{Pb})/\text{Sc}$ , and  $5\times[(\text{Fe}_2\text{O}_3+\text{MgO}+\text{MnO})/\text{Al}_2\text{O}_3]$ . Geochemical data indicate that sulphide mineralization in dark-grey to black metapelites does not necessarily imply that early sediments were deposited in anoxic (to euxinic) environmental conditions.

## 1 Introduction

Massive sulphide ores of the Iberian Pyrite Belt (IPB) are mostly hosted in volcanic-sedimentary rocks of uppermost Devonian age [Late Strunian, miospore biozone LN,  $360.7 \pm 0.7$  Ma - 362 Ma] to Early Carboniferous (e.g. Carvalho et al. 1999; Barrie et al. 2002; Pereira et al. 2007; Oliveira et al. 2013). These ore bodies do not show simple relationships with volcanic piles and some of them occur near the top of sequences that mark the waning stages of volcanic cycles. Here they show clear connections with the deposition of fine-grained siliciclastic sediments now represented by black metapelites (Sáez et al. 1999, 2011). There are also examples where the association of sulphide ores with volcanic rocks is not supported by firm evidence of any kind (e.g. Tornos et al. 1998). Therefore, additional data are needed to improve the characterization of specific geological settings where sulphide ore formation may have occurred.

## 2 Geological Background

The IPB is a fundamental unit of the South Portuguese Zone (SPZ) of the SW Variscides. Its stratigraphy includes, from bottom to top, the Phyllite-Quartzite Group (PQG), the Volcano-Sedimentary Complex (VSC) and part of the Baixo Alentejo Flysch Group (BAFG), also known as Culm Group (e.g. van den Boogaard 1963; Oliveira 1990). The Middle to Upper Devonian PQG consists of a siliciclastic succession composed of dark-grey to black metapelites, quartzites and meta-quartzwackes. The VSC (Upper Fammenian to Upper

Visean) comprises different volcanic suites inter-fingered or interbedded with a variety of metasedimentary rocks, including dark-grey to black metapelites and meta-siltstones, locally accompanied by meta-quartzwackes. The upper sections of VSC are dominated by siliceous, green and purple metapelites often coming along with meta-jaspers (or meta-cherts). The basal sequence of BAFG (Mértola Fm.) is a typical flysch sequence that contains intercalations of variable thickness of prevalent meta-greywackes and metapelites.

Variscan deformation is intense, documenting the progression of strain accommodation triggered by the oblique continental collision during Carboniferous. The resultant south-verging thin-skinned thrust-fold belt (e.g. Silva et al. 1990; Quesada, 1998) is concurrent of synorogenic metamorphic re-crystallization from the prehnite-pumpellyite to greenschist facies conditions (e.g. Munhá et al. 1983 a, b; Abad et al. 2001).

The sulphide ore-forming systems related to the large massive bodies are usually rooted in stockworks hosted in hydrothermally altered volcanic and metasedimentary sequences (e.g. Barriga et al. 1997, Tornos et al. 2000, Sáez et al. 2011). Evidence of synorogenic ore remobilization (during metamorphism and tectonic stacking) is common, further complemented by late-Variscan hydrothermal activity related to the propagation and reactivation of several strike-slip fault zones (e.g. Quesada 1998; Castroviejo et al. 2011; Luz et al. 2014).

## 3 Sampling

A geochemical sampling program was performed in the Portuguese segment of IPB, being oriented to (mineralized or non-mineralized) dark-grey or black metapelites included in several PQG and VSC sections. At the Aljustrel and Neves Corvo mining centres, samples were collected from different orebodies. Additional samples were obtained from drillcore of exploration surveys, including the recent massive sulphide intersection (hosted in black metapelites) of Sesmarias.

According to the compiled information (Pereira et al. 2007; Oliveira et al. 2013; unpublished technical reports), samples gathered in PQG sections ( $n=14$ ) range from AD to LN miospore biozones (Givetian-Strunian). The VSC samples are distributed into three subsets: i) Lower VSC ( $n=15$ ), spreading from VCo to LN miospore biozones (Upper Fammenian); ii) Intermediate VSC ( $n=8$ ), between LN and CM miospore biozones ( $\approx$  Lower Tournasian); and iii) Upper VSC ( $n=23$ ) ranging from CM to NL miospore biozones ( $\approx$  Upper Visean).

## 4 Main features of dark-grey to black metapelites

Metapelites show lepidoblastic textures and many microstructures that document heterogeneous strain accommodation. Irrespectively of the lithostratigraphic unit or their sub-divisions, all metapelites are variably enriched in non- or poorly ordered organic matter and the prevailing mineral assemblage comprises fine-grained white mica ( $\pm$  chlorite) and quartz, along with other accessory minerals, such as zircon, rutile, apatite and tourmaline. Considering the relative abundance of the major mineral phases, many of the sampled metapelites from PQG and Lower VSC comprise a significant component of sandy-derived (sub-millimetre sized) quartz. When enriched in sulphides, the relative abundance of chlorite and siderite ( $\pm$  dolomite/ankerite) increases.

Botryoidal and euhedral pyrite are common, often coupled with very fine-grained disseminations of chalcopyrite, pyrrhotite, sphalerite and galena. Early-fracture fillings (folded and affected by schistosity) are frequent and comprise siderite/dolomite/ankerite + pyrite  $\pm$  pyrrhotite ( $\pm$  chalcopyrite  $\pm$  sphalerite). At Aljustrel and Neves Corvo, many of these early-fracture infillings also contain Co-Ni- and Ni-Sb-bearing sulphides along with As-Co-Ni- and As-Ni(-Sb)-bearing sulfosalts.

## 5 Geochemical fingerprinting

According to the available whole-rock geochemical data, no significant differences exist in major element abundances for samples from PQG, Lower/Intermediate and Upper VSC. However, when samples are sorted as mineralized and non-mineralized according to their petrographic features, it is clear that: (i) higher median abundances of SiO<sub>2</sub>, Fe<sub>2</sub>O<sub>3</sub>, MgO and MnO characterize mineralized samples in Neves Corvo, Aljustrel, Lousal and Sesmarias; and (ii) higher median abundances of Al<sub>2</sub>O<sub>3</sub>, CaO and Na<sub>2</sub>O typify non-mineralized metapelites in all the sampled sections. The K<sub>2</sub>O, P<sub>2</sub>O<sub>5</sub> and TiO<sub>2</sub> abundances are not significantly different for the two groups of samples.

Abundances of minor and trace elements normalized to the Average Shale Composition (AS; Wedepohl, 1991) generate patterns that are similar for PQG and VSC metapelites. Systematic As and Sb positive anomalies (up to 5 $\times$ , sometimes 10 $\times$ AS) are observed when metapelites do not comprise sulphides. These As and Sb anomalies increase to 50 $\times$ AS (at times 100 $\times$ AS), when the samples are mineralized. In these cases, positive anomalies in Co, Ni and Cu (5 $\times$  to 30 $\times$ AS)  $\pm$  Zn  $\pm$  Pb (5 $\times$ AS) are also seen. Locally stronger (above  $\times$ 100AS) positive anomalies in Zn and Pb typify metapelites from Lower VSC of Neves Corvo and Upper VSC of Moinho orebody (Aljustrel mine) and of Monte das Mesas (mineral exploration drilling). Samples from Neves Corvo also show consistent depletions in Cu, Rb and Ba (<0.05 to 1 $\times$ AS). One sample from Moinho orebody (Aljustrel mine) displays a positive anomaly in Ba ( $\times$ 10AS). The

remaining elements tend to be close to the standard AS contents.

Patterns of REE abundances normalized to AS are flat, excepting those of mineralized samples from Neves Corvo which show slightly positive anomalies in Eu.

### 5.1 Provenance analysis

Considering the Zr/Sc (5.82-29.66), Th/Sc (0.56-2.06) and Eu/Eu\* (0.31-1.90) elemental ratios, an evolved felsic source might be inferred for the prevalent siliciclastic component forming the examined dark-grey to black metapelites from PQG or VSC (for reference values see, e.g., Middelburg et al. 1998, McLennan et al. 1993; Slack et al. 2004). This conclusion is also consistent with results reported in many other studies (e.g. Jorge et al. 2006; Luz et al. 2019), indicating that the chemically alike PQG and VSC metapelites derive from the same continental source.

### 5.2 Alteration/Mineralization Indexes

The Al<sub>2</sub>O<sub>3</sub>/(Al<sub>2</sub>O<sub>3</sub>+Fe<sub>2</sub>O<sub>3</sub>+MnO) and Fe<sub>2</sub>O<sub>3</sub>/TiO<sub>2</sub> ratios can be used to assess overprints of hydrothermal processes acting over a prevalent siliciclastic component (e.g. Marchig et al. 1982; Goodfellow et al. 2003). For IPB metasedimentary rocks, the overprinting is evident for Al<sub>2</sub>O<sub>3</sub>/(Al<sub>2</sub>O<sub>3</sub>+Fe<sub>2</sub>O<sub>3</sub>+MnO) <  $\approx$ 0.6 and Fe<sub>2</sub>O<sub>3</sub>/TiO<sub>2</sub> > 10 (see also, Luz et al. 2019; Fig.1).

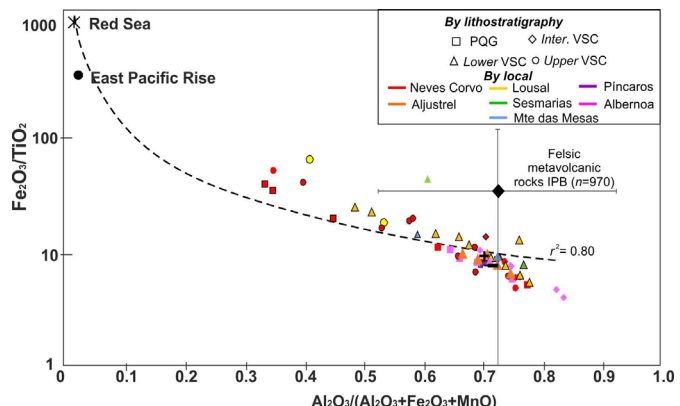


**Figure 1.** Fe<sub>2</sub>O<sub>3</sub>/TiO<sub>2</sub> vs. Al<sub>2</sub>O<sub>3</sub>/(Al<sub>2</sub>O<sub>3</sub>+Fe<sub>2</sub>O<sub>3</sub>+MnO) diagram illustrating a possible mixing strip between a “terrigenous” end-member (samples clustering) and a conceptual “exhalative-hydrothermal” term represented by the East Pacific Rise and/or the Red Sea brine pool compositions (e.g. Marchig et al. 1982; Goodfellow et al. 2003). Black borders indicate mineralized samples. Average values for felsic metavolcanic rocks of IPB are shown, using the dataset in Codeço et al. 2018.

The  $5\times[(\text{Fe}_2\text{O}_3+\text{MgO}+\text{MnO})/\text{Al}_2\text{O}_3]$ ,  $(\text{Cu}+\text{Zn}+\text{Pb})/\text{Sc}$  and  $(\text{As}+\text{Sb})/\text{Sc}$  ratios, when above 10, can also be used to separate barren from altered/mineralized dark grey to black metapelites (Fig. 2), in agreement with previous results gathered for other metasedimentary sequences in IPB (Luz et al. 2019).

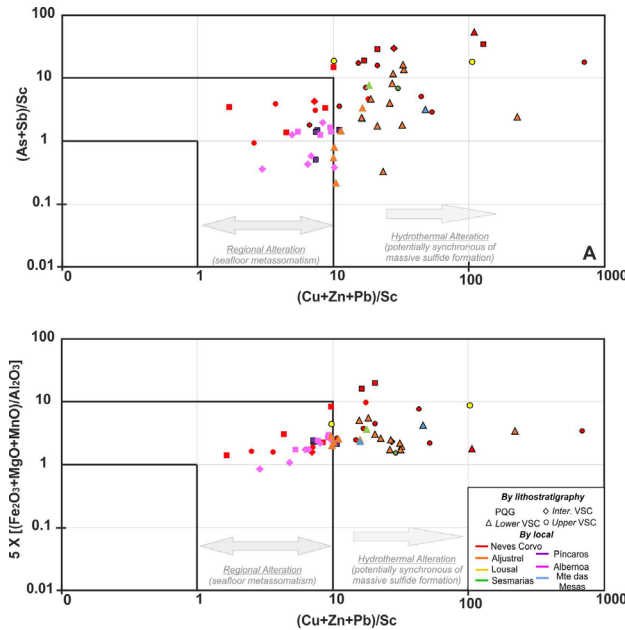


**Figure 2.**  $(\text{Cu}+\text{Zn}+\text{Pb})/\text{Sc}$  versus  $(\text{As}+\text{Sb})/\text{Sc}$  and  $5\times[(\text{Fe}_2\text{O}_3+\text{MgO}+\text{MnO})/\text{Al}_2\text{O}_3]$  diagrams illustrating the chemical effects related to post-sedimentary transformations. Values between 1 and 10 for the three ratios trace seafloor metasomatism; ratios above 10 indicate the proximity of hydrothermal discharges potentially related to massive sulphide ores. Black border mark mineralized samples.

### 5.3 Redox Conditions

Environmental redox conditions are critical to evaluate the degree of oxygen and hydrogen sulphide available in bottom-waters in equilibrium with sediments; and these may be determinant for the accumulation of shale-hosted massive sulphide ores (e.g. Sáez et al. 2011; Velasco-Acebes et al. 2018). Redox conditions can be inferred from a combined interpretation of some elemental abundances (e.g. S, Fe, Mn and Co) along with several element ratios (e.g. V/Cr, V/(V+Ni), U/Th) previously validated in a large variety of sedimentary settings (e.g. Wignall & Myers, 1988; Jones and Manning, 1994; Wignall & Twichett, 1996; Hoffman et al. 1998; Georgiev et al. 2012). However, as briefly documented above, some of these elements (S, Fe, Mn, Ni and Co) are included in mineral fingerprints of hydrothermal alteration and mineralization processes. In addition, U/Th ratios tend also to increase during fluid flow related to the formation of massive sulphide ores (Luz et al. 2019; Piercy & Kamber 2019). Thus, abundances of redox sensitive elements are disturbed in mineralized samples, which should be discarded of the intended assessment.

Most of our dataset display V/Cr ratios below 2 and 0.6 < V/(V+Ni) < 0.9; the correspondent S/Fe ratios are lower

than 0.52. Deviations from these trends are recorded for some mineralized samples of Aljustrel and Neves Corvo, documenting the hydrothermal alteration and mineralization progression. The U/Th ratios range mostly from 0.14 to 0.70; samples from Neves Corvo, Albernoa, Píncaros and part of Aljustrel are mostly below 0.5, but mineralized samples of Aljustrel show U/Th ratios above 0.5, reaching 2.94 (Fig. 3 and 4).

Considering only the non-mineralized samples from all sectors, parental sediments of the dark-grey to black metapelites were mainly deposited under oxygenated environments (sometimes transitional to suboxic conditions). At Aljustrel and Neves Corvo, many of these samples represent stratigraphic levels laterally equivalent to those that are mineralized. So, as far as can be extrapolated from the available information, sulphide mineralization in dark-grey to black metapelites does not implies necessarily that early sediments were deposited in anoxic (to euxinic) settings.

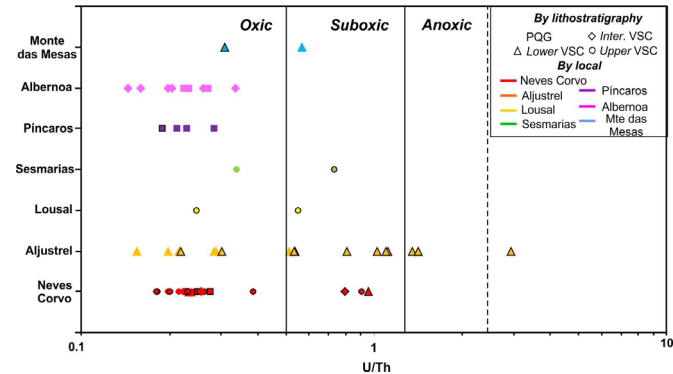


**Figure 3.** U/Th ratios for all dataset plotted by sector. Black border mark mineralized samples. Modified after Wignall & Myers, 1988; Jones and Manning, 1994; Wignall & Twichett, 1996.

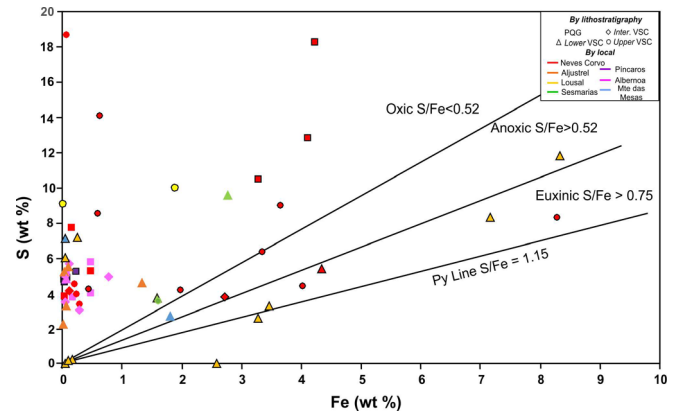


**Figure 4.** Bivariate diagram S vs Fe. Modified after Georgiev et al. 2012 and Rainswell et al. 1988.

### 6 Final Remarks

#### The main highlights from our results can be summarized as follows:

- Early-developed (prior to Variscan metamorphism and deformation) hydrothermal overprinting over a prevalent siliciclastic composition lead to  $\text{Fe}_2\text{O}_3/\text{TiO}_2$  ratios  $\geq 10$  and  $\text{Al}_2\text{O}_3/(\text{Al}_2\text{O}_3+\text{Fe}_2\text{O}_3+\text{MnO})$  ratios  $\leq \approx 0.6$ ;

- Proximity to hydrothermal discharges potentially associated with massive sulfide mineralization is indicated by  $(\text{As}+\text{Sb})/\text{Sc}$ ,  $(\text{Cu}+\text{Zn}+\text{Pb})/\text{Sc}$  and  $5 \times [(\text{Fe}_2\text{O}_3+\text{MgO}+\text{MnO})/\text{Al}_2\text{O}_3]$  ratios  $\geq 10$ ; and
- The development of sulphide mineralization in dark-grey to black metapelites does not imply necessarily that early sediments were deposited in anoxic (to euxinic) environmental conditions.

## Acknowledgements

Filipa Luz acknowledges the support of Fundação para a Ciência e Tecnologia (FCT; PD/BD/114485/2016 grant). Publication support by FCT project – UID/GEO/50019/2019 – Instituto Dom Luiz. Support provided by EPOS S.A., Lundin Mining, ALMINA, EDM, ESAN and AVRUPA Minerals to the performed sampling surveys is warmly acknowledged.

## References

- Abad I, Mata JP, Nieto F, Velilla N (2001) The phyllosilicates in diagenetic metamorphic rocks of the South Portuguese Zone, Southwestern Portugal. Canadian Mineralogist 39: 1571-1589
- Barrie C, Amelin Y, Pascual E, (2002) U-Pb geochronology of VMS mineralization in the Iberian Pyrite Belt. Mineralium Deposita 37:684-703
- Carvalho D, Barriga FJAS, Munhá J (1999) Bimodal-siliciclastic systems – the case of the Iberian Pyrite Belt. Rev Economic Geology 8:375-408
- Castroviejo R, Quesada C, Soler M (2011) Post-depositional tectonic modifications of VMS deposits in Iberia and its economic significance. Mineralium Deposita 46: 615-637
- Codeço M, Mateus A, Figueiras J, Gonçalves L, Rodrigues P (2018) Development of the Ervedel-Roxo and Figueirinha-Albernoa volcanic sequences in Iberian Pyrite Belt, Portugal: metallogenetic and geodynamic implications. Ore Geology Reviews 98:80-108
- Jones B & Manning DAC (1994) Comparison of geochemical indices used for the interpretation of paleoredox conditions in ancient mudstones. Chemical geology 111(1-4):111-129
- Georgiev S, Stein HJ, Hannan JL, Weiss HM, Bingen B, Xu G, Rein E, Hatio V, Loseth H, Nali M, Piasecki S (2012) Chemical signals for oxidative weathering predict Re-Os isochroneity in black shales, East Greenland. Chemical Geology 324-325:108-121
- Goodfellow WD, Peter JM, Winchester JA, van Staal CR (2003) Ambient Marine Environment and Sediment Provenance during Formation of Massive Sulfide Deposits in the Bathurst Mining Camp: Importance of Reduced Bottom Waters to Sulfide Precipitation and Preservation. Economic Geology, Monograph 11:129-156
- Jorge RCGS, Relvas JMRS, Matos JMX (2006) Geochemistry of metasediments from the Phyllite-Quartzite Group, Iberian Pyrite Belt: implications for provenance and source-area weathering. VII Congresso Nacional de Geologia, Livro de Resumos I. Estremoz, Universidade de Évora (Portugal):175-178
- Hoffman DL, Algeo TJ, Maynard JB, Joachimski MM, Hower JC, Jaminski J (1998) Regional stratigraphic variation in bottom waters anoxia in offshore core shales of Upper Pennsylvanian cyclothems from Eastern Midcontinent Shelf (Kansas), USA. In: Schieber J, Zimmerle W, Sethi P (eds) Shales and mudstones I. E Schweizerbart'sche Verlagsbuchhandlung, Stuttgart, 243-269
- Luz F, Mateus A, Matos JX, Gonçalves MA (2014) Cu- and Zn-Anomalies in the NE border of the South Portuguese Zone (Iberian Variscides, Portugal) Identified by Multifractal and Geostatistical Analyses. Natural Resources Research 23(2):195-215
- Luz F, Mateus A, Figueiras J, Tassinari CCG, Ferreira E, Gonçalves (2019) Recognizing metasedimentary sequences potentially hosting concealed massive sulfide accumulations in the Iberian Pyrite Belt using geochemical fingerprints. Ore Geology Reviews 107:973-998
- McLennan SM, Hemming S, McDanniel DK, Hanson GN (1993) Geochemical approaches to sedimentation, provenance, and tectonics. In: Johnsson MJ, Basu A (Eds). Processes controlling the Composition of Clastic Sediments. Geological Society of America Special Paper 285:21-40
- Middelburg JJ, Van Der Weijden CH, Woittiez JRW (1988) Chemical processes affecting the mobility of major, minor and trace elements during weathering of granitic rocks. Chemical Geology 68:253-273
- Oliveira JT (1990) Stratigraphy and syn-sedimentary tectonism in the South Portuguese Zone. In: Dallmeyer, RD, Martinez Garcia E (Eds), Pre-Mesozoic Geology of Iberia. Springer Berlin Heidelberg, Berlim, pp. 334-347
- Oliveira JT, Relvas J, Pereira Z, Matos J, Rosa C, Rosa D, Munhá J, Fernandes P, Jorge R, Pinto Á (2013) Geologia da Sul Portuguesa, com ênfase na estratigrafia, vulcanologia física, geoquímica e mineralizações da faixa piritosa. In: Dias R, Araújo A, Terrinha P, Kullberg JC (Eds). Geologia de Portugal Vol. I, Geologia Pré-Mesozóica de Portugal, Escolar Editora, pp.0.807
- Pereira Z, Matos J, Fernandes P, Oliveira JT (2007) Devonian and Carboniferous palynostratigraphy of the South Portuguese Zone, Portugal – An overview. Comunicações Geológicas 94:53-79
- Piercey SJ & Kamber BS (2019) Lead isotope geochemistry of shales from the Wolverine volcanogenic massive sulfide deposit, Yukon: implications for Pb Isotope vectoring in exhalative ore systems. Economic Geology 114(1):47-66
- Quesada C (1998) A reappraisal of the structure of the Spanish segment of the Iberian Pyrite Belt. Mineralium Deposita 33:31-44
- Raiswell R, Buckley F, Berner RA, Anderson TF (1988) Degree of pyritization of iron as a paleoenvironmental indicator of bottom-water oxygenation. Journal of Sedimentary Petrology 58:812-819
- Sáez R, Pascual E, Toscano M, Almodóvar GR (1999) The Iberian type of volcano-sedimentary massive sulfide deposits. Mineralium Deposita 34:549-570
- Sáez R, Moreno C, González F, Almodóvar GR (2011) Black shales and massive sulfide deposits: causal or casual relationships? Insights from Rammerlsberg, Tharsis and Draa Sfar. Mineralium Deposita 46:585-614
- Slack HF, Dumoulin JA, Schmidt JM, Young LE, Rombach CS (2004) Paleozoic sedimentary rocks in the Red Dog Zn-pb-Ag district and vicinity, western metallogenetic significance. Economic Geology 99:1385-1414
- Tornos F, Spiro B, (1998) The genesis of the shale hosted massive sulphides in the Iberian Pyrite Belt. In: Stacey, CJ (Ed), Mineral Deposits: processes to processing. Balkema, Rotterdam, pp. 605-608
- Tornos F, Barriga F, Marcoux E, Pascual E, Pons JM, Relvas J, Velasco F (2000) The Iberian Pyrite Belt. In: Large R, Blundell D (Eds), Database on global VMS districts: CODES-GEODE, pp. 29-52
- Van den Boogaard M (1963) Conodonts of Upper Devonian and Lower Carboniferous age from Southern Portugal. Geologie en Mijnbouw 42:248-259
- Velasco-Acebes J, Tornos F, Kidane AT, Wiedenbeck M, Velasco F, Delgado A (2018) Isotope geochemistry tracks the maturation of massive sulfide mounds (Iberian Pyrite Belt). Mineralium Deposita
- Wignall PB & Myers KJ (1988) Interpreting benthic oxygen levels in mudrocks: A new approach. Geology 16 (5): 452-455
- Wignall PB & Twichett RJ (1996) Oceanic Anoxia and the End Permian Mass Extinction. Science 272:1155-115

# Diagenetic evaluation of a possible redbed source for anomalous Cu in the Paleozoic-hosted Cornwallis Zn district, NU

Mathieu, J., Turner, E.C

*Laurentian University*

**Abstract.** The Storm Cu deposit in Arctic Canada overlies a Proterozoic red sandstone unit (Aston Formation), which may have had a role in mineralisation. Petrographic analysis of red and grey/white samples of the Aston Formation reveal multiple hematite cement phases, including an early and a late stage. Early hematite is identified by the presence of hematite-coated Aston Formation grains in Mesoproterozoic strata. Late hematite is identified by relationships indicating that it post-dated chemical compaction during maximum burial. Bleaching removed hematite cement locally and is associated with higher amounts of quartz cement and maximum burial. Bleaching implies the circulation of a reduced fluid, whereas oxidised fluid circulation is implied by the presence of hematite post-dating bleaching. The timing relationship of a reduced fluid mobilised during early to maximum burial followed by the circulation of oxidised fluids is similar to that recorded at the Storm Cu deposit. This suggests that the Proterozoic Aston Formation red sandstone may have been a source for metals for the Paleozoic Storm Cu deposit, and that several prolonged episodes of fluid circulation took place.

## 1 Introduction

Sedimentary-rock-hosted Cu deposits are commonly attributed to metals sourced from adjacent red-bed units (Hitzman et al. 2005), but diagenetic studies of the redbeds invoked are generally lacking. Walker et al. (1984) and Zelinski et al. (1987) concluded that red-bed source rocks were not deposited red, but were reddened during early diagenesis over several millions of years. It is this oxidising process that liberates and transports the Cu to the site of mineralisation Brown (2005; 2009). In the Cornwallis Zn-Pb district of Arctic Canada (Dewing et al. 2009), an anomalous Cu deposit (Storm copper) is exposed in the southern part of the district on Somerset Island. Storm copper is a carbonate-hosted Cu deposit that overlies Mesoproterozoic red-beds of the Aston Formation, an inferred source of metal for Storm copper (Mathieu et al. 2018). The present study involves a petrographic analysis of the Aston Formation red-beds in order to determine its diagenetic history and evaluate whether it was a metal source for the Storm copper deposit.

## 2 Geologic history

The stratigraphy on Somerset Island is a succession of Paleozoic carbonate rocks unconformably overlying

Mesoproterozoic clastic (Aston Formation) and carbonate (Hunting Formation) units, both of which are cross-cut by Proterozoic dykes and sills (Tuke et al. 1966).

The Aston Formation is an 800-m-thick succession of red, purple, grey, brown, and white terrigenous clastic sandstone, conglomerate, and siltstone/shale (Tuke et al. 1966). The Hunting Formation is a 1.3-km-thick carbonate succession (Dixon et al. 1971).

The Devonian-Carboniferous Ellesmerian orogeny was the main tectonic event that affected the Cornwallis district and resulted in a clastic wedge up to 6 km thick (Embry 1991). This event is also thought to be the main fluid mobilisation event responsible for mineralisation in the district (Dewing et al. 2007).

## 3 Materials and methods

Samples collected along a transect through the Aston Formation, which include both red and white (bleached) sandstone (Fig. 1), were used for this study.

Samples were prepared as polished thin sections for petrographic and SEM analysis at Laurentian University, Sudbury Ontario. Petrography was done on standard petrographic microscope using transmitted, reflected, and oblique incident light. Abundance of grains, cement, and porosity was estimated visually.

## 4 Results

Sandstone samples are composed of 75-85% framework grains, with 10-20% cement, and approximately 5% porosity. Framework grains are predominantly fractured quartz (80%) and feldspar (20%), with rare Ti-Fe grains. Grain-to-grain contacts are predominantly long concavo-convex surfaces with subordinate sutured and point contacts (Fig. 1). Quartz cement is the dominant pore-filling phase, with lower amounts of feldspar. Hematite is present primarily as grain-coating cement (providing the red colour of the formation).

Hematite cement is typically overlain by other cements, but is also present as overgrowths on other cements. It is less abundant in bleached samples and apparently absent at pressure-solved contacts, but present around pressure-solved grains (Fig. 1). Some bleached samples have grains that are partially coated with hematite. Muscovite is primarily pore-filling but is also present in bleached samples coating grains and altering feldspars.

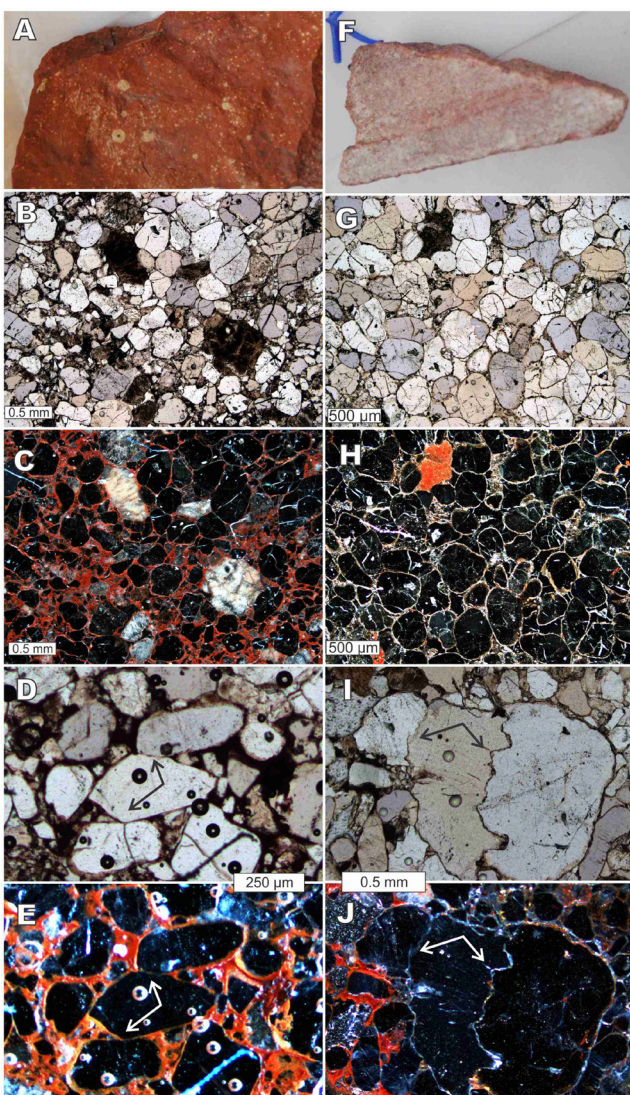


**Figure 1.** Hand sample and thin section photographs of unbleached (A-E) and bleached (F-J) samples that show the characteristics of the paragenesis. (B and C) transmitted and oblique incident light images show the red hematite coating around framework grains, except at (D and E) point and concavo-convex and (I and J) sutured grain contacts (arrows). (G and H) bleached samples had hematite removed from around grains.

## 5 Interpretation

In order to determine the timing of fluid circulation and the possibility that the Aston Formation was the metal source for the Storm copper deposit, the paragenesis of diagenetic events is presented in Figure 2 and discussed below.

The presence of hematite both underlying and overlying other cements indicates that at least two episodes of hematite precipitation took place (reddening events). The first reddening is represented by hematite underlying later cements; the timing of this cement is constrained by the presence of hematite-coated Aston Formation grains in Hunting Formation (Mesoproterozoic) rocks, which indicates an early diagenetic event. The absence of hematite at pressure-solved grain contacts, but its presence around such grains, indicates that a

second hematite-precipitating event post-dated (maximum) burial. This timing then provides a youngest time constraint on the timing of the bleaching event, which predated hematite in order to not have hematite at pressure-solved grain contacts.

Partly hematite-coated grains that are overgrown by quartz cement suggest that bleaching occurred prior to or at the same time as quartz cementation. The abundance of fractures in framework grains, but their absence in cement, suggests that cementation took place during (near-)maximum burial, and may be related to pressure-solution. This provides an additional timing constraint sandstone bleaching which had to take place at burial depths where pressure-solution is the dominant compaction process (i.e., deeper than 2 km; von Noort et al. 2008). Because The Hunting Formation is only approximately 1 km thick, it may not have been thick enough to cause chemical compaction of Aston Formation sandstone; therefore burial must have been related to the accumulation of Paleozoic passive-margin strata and/or the clastic wedge of the Ellesmerian orogeny.

## 6 Discussion

The majority of diagenetic events recorded by the Aston Formation took place during the middle Paleozoic (Fig. 2). The initial reddening processes may have prepared the rocks for a later fluid that transported Cu. Bleaching of the red sandstone indicates a reduced fluid, which removed the hematite at around the time of the Ellesmerian orogeny, which was probably the driving force behind fluid circulation. This condition is in agreement with the fluid history of pre-ore mineralisation at the Storm copper deposit, which involved a reduced, basement-equilibrated fluid (Mathieu et al. 2018). Following bleaching and maximum burial, the Paleozoic reddening process most probably indicates the circulation of a meteoric-sourced, oxidised fluid that would have transported Cu (Brown, 2005; 2009). The shift from a reduced basin-equilibrated fluid to an oxidised meteoric fluid as indicated here is in agreement with the change from pre-ore to main-stage ore at Storm copper, which was precipitated by a meteoric-sourced fluid that acquired Cl by dissolving evaporites and equilibrated at depth (with the Aston Formation), bringing Cu to a site of reduction (Mathieu et al. 2018). Therefore, it is probable that the Aston Formation red-beds were the metal source for the Storm copper deposit.

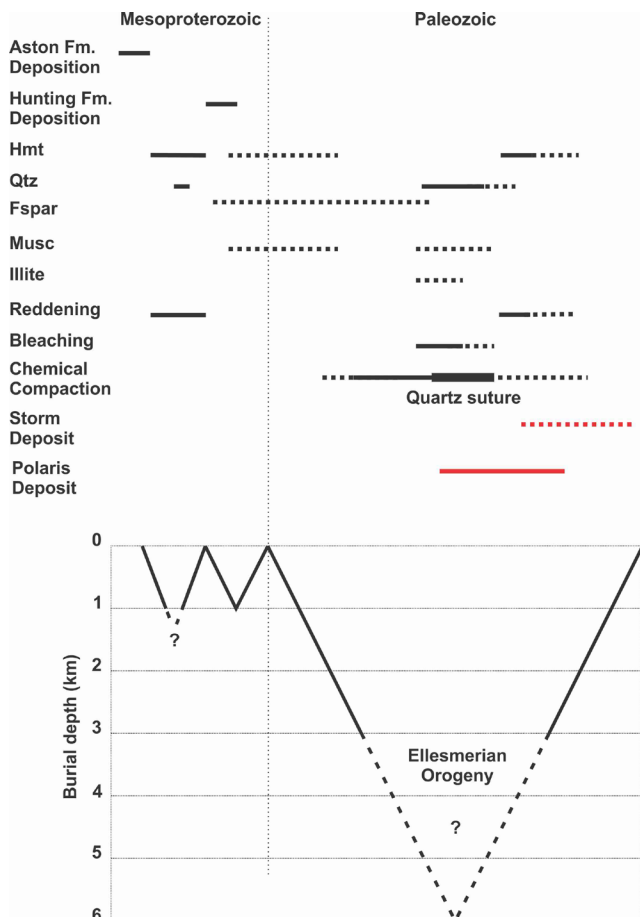


**Figure 2.** Paragenetic interpretation of diagenetic phases and the proposed timing relative to fluid circulation and burial history.

## Acknowledgements

Financial support for analytical work supplied by Geological Survey of Canada GEM-II program; field

support and logistics through NSERC-Discovery Grant to E. Turner and Polar Continental Shelf Project (NRCan).

## References

- Brown AC (2005) Refinements for footwall red-bed diagenesis in the sediment-hosted stratiform copper deposits model. *Econ. Geol.* 100:763-771.
- Brown AC (2009) A process-based approach to estimating the copper derived from red beds in the sediment-hosted stratiform copper deposit model. *Econ. Geol.* 104:857-868.
- Dewing K, Sharp RJ, Turner EC (2007) Synopsis of the Polaris Zn-Pb district, Canadian Arctic Islands, Nunavut. In: Goodfellow, W.D. (Ed.), *Mineral Deposits of Canada: A Synthesis of Major Deposit-Types, District Metallogeny, the Evolution of Geological Provinces, and Exploration Methods*, Geological Association of Canada, Mineral Deposits Division. Special Publication No. 5:655-672.
- Dixon J (1977) Revised stratigraphy of the Hunting Formation (Proterozoic), Somerset Island, Northwest Territories. *Can. J. Earth Sci.* 11:635-642.
- Embry AF (1991) Middle-Upper Devonian clastic wedge of the Arctic Islands. In: Trettin, H.P. (ed) *Geology of the Inuitian Orogen and Arctic Platform of Canada and Greenland*. Geol. Surv. Canada, pp. 261-291.
- Hitzman MW, Kirkham R, Broughton D, Thorson J, Selley D (2005) The sediment hosted stratiform copper ore system. *Economic Geology*, 100:609-642.
- Mathieu J, Turner EC, Kontak DJ, Fayek M, Mathur R (2018). Atypical Cu mineralisation in the Cornwallis carbonate-hosted Zn district: Storm copper deposit, Arctic Canada. *Ore Geol. Rev.* 99:86-115.
- Tuke MF, Dineley DL, Rust BR, (1966) The basal sedimentary rocks in Somerset Island, N.W.T. *Can. J. Earth Sci.* 3: 697-711.
- Von Noort R, Spiers CJ, Pennock GM (2008) Compaction of granular quartz under hydrothermal conditions: controlling mechanisms and grain boundary processes. *J. Geophys. Res.* 113:1-23.
- Walker TR (1984) Application of diagenetic alterations in red beds to the origin of copper in stratiform copper deposits. GAC Special Paper 36:85-96 (1984)
- Zelinski RA, Bloch S, Walker TR (1983) The mobility and distribution of heavy metals during the formation of first cycle red beds: *Econ. Geol.* 78:1574-1589.

# Hot, deep-sourced, hydrothermal Cu-Ag-Au-PGE-polymetallic deposits of Zechstein Kupferschiefer age

**Volker Spieth, Hans-Joachim Massonne**

*University Stuttgart, Germany, Institute for Mineralogy and Crystalchemistry*

**Jürgen C. Kopp**

*JCK Consulting, Seddiner See, Germany*

**Tillmann Viefhaus**

*AVISpectro TGU, Stuttgart, Germany*

**Michael Trinkler**

*Erz und Stein, Bobritzsch, Germany*

**Heinz-Jürgen Bernhardt**

*University Bochum, Mineralogical Institute*

**Stanley B. Keith, Jan C. Rasmussen**

*MagmaChem, Sonoita, Arizona, USA*

**Abstract.** Cu-Ag-Au ore grade mineralization of hot hydrothermal origin has been discovered in the Zechstein Kupferschiefer deposit in Spremberg, Lausitz, Germany. The uppermost Permian-aged, 15 by 5 km deposit is hosted in Weissliegend silica extrudite, Kupferschiefer *sensu stricto* Mg-Ca-Si-rich chemical mud and Mg-Ca-rich Zechstein dolostone.

Multi-phase mineralogical investigations based on a large number of new exploration drill samples have revealed hydrocarbon-rich and co-existing metallic mineralization with depositional temperatures of >350°C. The dominant metallic mineral assemblage is chalcocite, digenite, bornite, chalcopyrite, electrum and disseminated silver and gold. Microscopic, electron microprobe, Raman and Sulfur isotope studies indicate an origin of deep-sourced basic-ultrabasic brines of serpentinitic-Iherzolitic geochemistry in the continent sized European-Copper-Belt extending over more than 750 km with a width of 5 to 20 km. Non-stoichiometric composition of the Cu-sulfides, copper-copper-exsolutions in solid-state and of electrum in bornite are common. The PGE-V-Mo-polymetallic-hydrocarbon-rich extrudite Kupferschiefer *sensu stricto* slurry mud is typical for Kupferschiefer Zechstein deposits of Germany and Poland. The sheer billion-ton-volume of economic grade Cu-Ag-Au-PGE-polymetallic-hydrocarbon-rich mineralization of the narrow E-W continuous European-Copper-Belt of Zechstein age favors a dynamic extrusive Zechstein age submarine depositional model.

## 1 Introduction

The recent exploration of the Spremberg Kupferschiefer Cu-Ag-Au-polymetallic deposit, Lausitz, Germany, has produced a great many new samples and insights. Geological and mineralogical research has resulted in a paradigm change in the depositional model for the European upper Permian Kupferschiefer class of deposits of global importance.

The European Copper Belt of Permian Kupferschiefer deposits stretches from the Rhön-Richelsdorf mountains in the west of Germany via the Spremberg to the Sudetic Forelands in the east of Poland over a distance of more than 750 km. The individual deposits are about 5 to 20 km wide, 2 to 40 meters thick, outcropping sometimes, but are mostly at a depth from 300 to 2,500 m. The Polish Lubin district mines produce more than 500,000 t of Cu metal annually (Zientek et al. 2015).

Change is happening in the understanding of the high grade Zechstein Kupferschiefer paragenesis. For decades the depositional model was synsedimentary-sapropelic, replacement, low-temperature mineralization in the context of an euxinic Kupferschiefer sea (Köbel 1958; Richter 1941; Rentzsch 1965; Borg et al. 2012). Recent publications have indicated the novel possibility of Permian to Triassic era rift-related, multi-phase, hydrothermal geological models (Blundell et al. 2001; Blundell et al. 2003; Kopp and Spieth et al. 2012; Spieth et al. 2014) causing the abandonment of the "obsolete" syn-sedimentary (Borg 2017) model. Though most paragenetic observations are shared, the interpretation of the origins is leading to a contentious scientific discourse. Here, the current research results favor the high energy, hot hydrothermal, deep sourced models.

## 2 Geological setting and age of the deposits

The Kupferschiefer sea transgression covered more than 600,000 km<sup>2</sup> of upper Permian peneplain from Greenland to eastern Poland. The calcareous shale may carry some iron sulfides and rarely reaches a thickness of more than a few centimeters. The southern margin of the Kupferschiefer sea covered the west-east striking continent size lineaments on top of the buried Variscan massifs with a perpendicular tectonic faulting pattern. These basement deep lineaments and faults have been active pre- and post-Permian. They can be traced by 3-D seismic geophysical and residual anomalous heat

measurements (Blundell et al. 2003; Borg et al. 2012; Kopp and Spieth et al. 2012; Oszczepalski et al. 2017).

A great deal of individual micro-layers in the Kupferschiefer *sensu stricto* was analyzed (Von Bubnoff 1950) and calculated regarding the time needed for the deposition with the result of not more than 10,000 years. This does not contradict the accepted depositional age of the Zechstein Kupferschiefer black shale *sensu stricto* to be from 247 to 257 Ma, based on Re-Os dates (Mikulski et al. 2017). Also reported is a whole-rock and mineral-separate isochron from several samples from the Sangerhausen, Germany, Kupferschiefer *sensu stricto* deposit with a Re-Os date of  $257 \pm 1.6$  Ma. This represents a depositional age for the base of the Zechstein Group. Six samples of non-mineralized black shale from a Kupferschiefer section in the northern part of the Polish Zechstein Basin yield a Re-Os date of  $247 \pm 20$  Ma (Pašava et al. 2010). The paleo-magnetic dating of the alteration phase "Rote Fäule" hematite yielded dates of 255 to 245 Ma (Nawrocki 2000). Eight high-quality illite samples (Bechtel et al. 1999) yielded an average age for the Kupferschiefer *sensu stricto* of  $252.5 \pm 4.5$  Ma (Keith and Spieth et al. 2018). These illite samples occur in the high energy / high early copper / Rote Fäule illite-hematite core zones of the Cu-Ag-Au-polymetallic high grade Kupferschiefer system. The complex age history centered on 252.5 Ma with a range of plus/minus 5 Ma indicates the multi-phase origin and consequent alteration of the high grade Kupferschiefer deposits.

### 3 Spremberg, Lausitz, Germany, Zechstein Kupferschiefer deposit

The Spremberg-Graustein-Schleife Zechstein Kupferschiefer deposit is representative for the mineralization along the Permian-Triassic age European Copper Belt. In each of these deposits, the geometallurgy of the Kupferschiefer related high-grade, copper-polymetallic-precious-metal, hydrocarbon mineralization is present. Chalcocite and digenite are common occurrences. Bornite often carries disseminated silver and exsolutions of electrum. Base-metal-bearing selenides (klockmannite [CuSe] and krutaite [CuSe<sub>2</sub>]) coexist with covellite and digenite, which form at high temperatures (384–343°C). The Kupferschiefer *sensu stricto* facies contains exotic elements such as PGE, Co, Ni, Cr, V, Se, Re, Os, that suggest Kupferschiefer copper-silver mineralization fractionated from deep-sourced, high-temperature, hydrothermal fluids, possibly mantle-sourced ultra-mafic rocks. The new high energy hot hydrothermal Kupferschiefer deposit model is a paradigm change to the "obsolete" (Borg 2017) syn-sedimentary to epigenetic model.

#### 3.1 Zechstein Weissliegend sand injectite/extrudite silica slurry

A principal geological parameter for the recognition of the dynamic emplacement model are the observations and geological mappings in Sangerhausen-Wetteldorf and Spremberg, Germany, and the Lubin-Rudna district,

Poland, that shows: (1) The Weissliegend sand is an injectite/extrudite, silica slurry of Zechstein age that mostly rests on top of the Permian Rotliegend peneplain and is covered in an undulating manner by Kupferschiefer *sensu stricto*. (2) The Weissliegend sands are cut by veins and veinlets of sulfides and hydrocarbon and Kupferschiefer-like black mud rock that may represent the feeder veins of an open, hot-hydrothermal vent. (3) The Weissliegend sand hosts by far the majority in quality and quantity of the Kupferschiefer-type, mineable copper resources, measured in 100s of millions of tons. The recognition of sand injectites/extrudites is a paradigm change in evaluation of the Zechstein Weissliegend sands and sandstone sedimentary structures globally (Hurst et al. 2006; Hurst et al. 2011).

#### 3.2 Hot hydrothermal metallic and hydrocarbon mineralization

Mineralogical results obtained from the Spremberg-Graustein-Schleife and other European Cu-Ag-Au-polymetallic high grade deposits through microscopy, electron microprobe, Raman spectroscopy, geochemistry and  $\delta^{34}\text{S}$  sulfur isotope analysis show that: (1) The Kupferschiefer deposit type mineralization in its vast majority is somewhat monotonous, as it is made up in Spremberg and the European Copper Belt of chalcocite (Cu<sub>2</sub>S), digenite (Cu<sub>1.75</sub>S<sub>5</sub>), covellite (CuS), bornite (Cu<sub>5</sub>FeS<sub>4</sub>) and chalcopyrite (CuFeS<sub>2</sub>), plus a high (up to 24 wt. % Corg or nearly 50 % by volume) hydrocarbon content, which is significant as it occurs over a distance of more than 750 km in length. (2) Much of the copper minerals are of non-stoichiometric composition and unusual association. Bornite, chalcocite, chalcopyrite and pyrite occur as spherules, immiscible metallic drops in the slurry mud. Bornite of the Kupferschiefer *sensu stricto* T-1 layer often shows exsolutions of electrum (AuAg) and other solid state copper-copper exsolutions with chalcopyrite and covellite, indicating pre-mixture in the rising metal-hydrocarbon mud slurry and rapid cooling after extrusion on the sea floor surface. (3) The microprobe element analysis of sulfide phases that are widespread in natural ores of the Kupferschiefer Cu-Ag deposits plot in a phase field that includes chalcocite, digenite, djurleite, anilite, yarrowite ("blaubleibender" covellite), klockmannite and krutaite. Klockmannite (CuSe) and krutaite (CuSe<sub>2</sub>) have a stability field of about 343°C and 384°C and thus document the high-temperature, hydrothermal nature of the mineral deposition (Kopp and Spieth et al. 2012; Viefhaus and Spieth et al. 2013). The calculations were undertaken with the MINCALC program (Bernhardt et al. 1995; Bernhardt 2010).

#### 3.3 $\delta^{34}\text{S}$ Sulfur stable isotopes analysis

The  $\delta^{34}\text{S}$  Sulfur stable isotopes are a unique feature to the Kupferschiefer *sensu stricto* and at Spremberg have a similar composition as those of the copper mineralization of the other deposits of the European Copper Belt. The  $\delta^{34}\text{S}$  Sulfur stable isotopes are light to very light with values

ranging from  $-15\text{\textperthousand}$  to  $-31\text{\textperthousand}$  to  $-42\text{\textperthousand}$  in chalcocite-digenite and chalcopyrite samples of the Kupferschiefer *sensu stricto*. Given the high temperature of the sulfide mineralization, these low values cannot be explained by microbial reduction. Published diagrams (Tornos et al. 2008; Wagner et al. 2010; Schwarzenbach et al. 2012; Basori et al. 2017) show deep-sourced systems of ultramafic to serpentinitic origin and composition can contribute brines with a similar light  $\delta^{34}\text{S}$  sulfur stable isotope composition.

### 3.4 Geochemistry and geometallurgy

Geochemical, major and trace element compositions are anomalous and much enhanced compared to average global black shale. The Kupferschiefer *sensu stricto* analysis and geostatistical comparison diagrams demonstrate the interdependence of the base, precious and polymetallic mineralization with the hydrocarbon deposition in the Zechstein rocks.

Geometallurgical analysis of the available operational and scientific data proves the genetic association of the enriched exotic elements PGE, Co, Ni, Cr, V, Se, Re, Os with the contemporaneously deposited (up to 24 wt. % Corg) hydrocarbon chemical mud, a mineralogical factum that influences the beneficiation of the Kupferschiefer *sensu stricto* ore greatly. (Guzmer 2014; Rahfeld and Guzmer et al. 2018)

### 3.5 Rote Fäule hematitic alteration

Geological observation and mineralogical analyses demonstrate that the hematitic “Rote Fäule” is a post-Zechstein-Kupferschiefer pervasive alteration event. In places, the “Rote Fäule” may have two distinct phases, of which one might have added gold to the system, forming independent new deposits. The advancing “Rote Fäule” front creates a “TZ Transition Zone” where existing base and precious metals are enriched to a higher grade while in the vast areas covered by pervasive “Rote Fäule” all sulfide mineralization has been oxidized leaving hematitic remnants.

## 4 The new hot, deep-sourced, hydrothermal Cu-Ag-Au-PGE-polymetallic deposit model

The new hot hydrothermal deposit model documented by geochemical, mineralogical, sulfur isotope measurements in tables and diagrams has been developed during the recent PhD study by Spieth (2019).

The new model for the Zechstein Kupferschiefer depositions postulates a high-energy, hot hydrothermal, extrusive environment that is somewhat similar to submarine “black smoker” and volcanogenic, submarine, metal-brine deposits. The metal-rich fluids ascended through deep-reaching faults and erupted as slurries in low-relief, mud volcanism above fractures in an open, shallow, inland sea. Metal sulfide deposition is systematically accompanied by the precipitation of silica, dolomitic carbonate, and illite, as well as primary copper chlorides (such as atacamite  $\text{CuCl}_2$ ) and other brine

minerals, such as anhydrite and sylvite.

Large, deep-reaching, continent-size, rifting lineaments are known in the Zechstein mineralized area of the European Copper Belt. These NW-SE lineaments are disrupted by NE-SW faults. This tectonic pattern is common in all Kupferschiefer districts and has been demonstrated with a seismic exploration program at Spremberg

The ultimate brine source is interpreted to be serpentized peridotite in the lower crust near the Moho transition to the mantle. Dehydration of the serpentinite source to talc (steatization) by mantle heat during failed, intra-continental rifting of the Pangaea supercontinent at the end of Permian time released vast amounts of element-laden, high-density brines into deep basement fractures, depositing them above the continental flysch sediments of the Rotliegend sandstone and conglomerate peneplain in the shallow Kupferschiefer sea, which is analogous to the modern northern Caspian Sea and the Salton Sea of southern California, USA.

## 5 Outlook

The paradigm change (Spieth 2018) in the geologic and paragenetic Kupferschiefer deposit model has consequences for exploration and mining in the European Copper Belt. The Cu-Ag-Au-PGM-polymetallic “undiscovered Kupferschiefer resources” (Zientek and Spieth et al. 2015) may be hosted by (1) the underexplored footwall Zechstein Weissliegend injectite/extrudite hot hydrothermal primary silica slurry metallic mud strata; (2) the primary native gold deposits (Pieczonka et al. 2008); and (3) the Cu-Ag-Au-PGM-polymetallic enriched “TZ” Transition Zone in front of the vast advancing “Rote Fäule” hematitic alteration (Oszczepalski et al. 2017).

Two thirds of the European Copper Belt is underexplored. The new model, based on the underground mining and geological knowledge from the Polish operations and the Spremberg deposit, indicates that the guides to locate new Zechstein Kupferschiefer resources are (1) large tectonic lineaments; (2) Weissliegend “sand bars” in the sulfide mineralized areas; (3) the up to several kilometer wide fringes of the “TZ” Transition Zone in front of the “Rote Fäule” alteration; and (4) the large “sand bars” possibly mineralized with primary native gold within the “Rote Fäule” alteration zone that was previously considered barren. This exploration model has been successfully tested at the Spremberg-Graustein-Schleife deposit that contains in an area of about 20 km by 5 km an underground resource of 3 Mt copper plus associated metals (Spieth 2016).

## Acknowledgements

This research was carried out with the support of the Mineralogical Institute of the University Stuttgart under the leadership of Prof. Dr. Massonne, and at the Mineralogical Institutes at Tuebingen, Bochum, Aachen and Freiberg, Germany, whose technical and knowledge

support is gratefully acknowledged. Much appreciation is expressed for the generous assistance provided by many research colleagues, geologists and engineers in the Spremberg project, Germany, the Gliwice Instytut Metalu Nielazanych, Poland, and Kupferschiefer exploration projects, mines and plants that were visited and studied.

## References

- Basori MBI, Zaw K, Large RR, Hassan WFW (2017) Sulfur isotope characteristics of the Permian VHMS deposits in Tasik Chini district, Central Belt of Peninsular Malaysia. *Turkish J Earth Sci* 26:91–103.
- Bechtel A, Elliott WC, Wampler JM, Oszczepalski S (1999) Clay mineralogy, crystallinity, and K-Ar ages of illites within the Polish Zechstein Basin: Implications for the age of Kupferschiefer mineralization. *Econ Geol* 9:261–272.
- Bernhardt HJ, Massonne HJ, Reinecke T, Willner AP (1995) Digital element distribution map, an aid for petrological investigations. *Ber. Dt. Mineral. Ges., Beih. 1, European J. Mineral.* 7:28,
- Bernhardt HJ (2010) MINCALC-V5-Program. Inst Geol Mineral Geophy Univ Bochum.
- Blundell DJ, Alderton DHM, Karnkowski PH, Oszczepalski S, Streetmann-Heinen V, and Kucha H, (2001) A new genetic model for the copper mineralization of the Polish Kupferschiefer. *In Piestrynski A ed, Mineral deposits at the beginning of the 21th century. Lisse (Swets & Zeitlinger)*, 215–218.
- Blundell DJ, Karnkowski PH, Alderton DHM, Oszczepalski S, Kucha H (2003) Copper mineralization of the Polish Kupferschiefer—A proposed basement fault-fracture system of fluid flow. *Econ Geol* 98:1487–1495.
- Borg G, Piestrynski A, Bachmann GH, Püttmann W, Walther, S, Fiedler M (2012) Chapter 18, An overview of the European Kupferschiefer deposits. In Society of Economic Geologists, Spec Pub 16:455–486.
- Borg G (2017) It's all about timing – The origin of the European Kupferschiefer ores. *World Mining* 69:1:1–7.
- Bubnoff S (1950) Die Geschwindigkeit der Sedimentbildung und ihre endogener Antrieb: – Abhandlung zur Geotektonik. Akademie Verlag Berlin 1–33.
- Guzmer J (2014) Geometallurgie – warum Metallurgen mit Geowissenschaftlern kommunizieren sollten. *Erzmetall* 67:54–58
- Hurst A, Cartwright JA, Huuse M, Durati D (2006) Extrusive sandstone (extrudites): a new class of stratigraphic trap? *In Allen MR, Goffey GP, Morgan RK, Walker IM (eds.), The Deliberate Search for the Stratigraphic Trap: Special Publication. Geological Society London* 254:215–246
- Hurst A, Scott A, Vigorito M (2011) Physical characteristics of sand injectites: *Earth-Science Reviews* 106:215–246.
- Keith SB, Spieth V, Rasmussen JC (2018) Zechstein Kupferschiefer mineralization reconsidered as a product of ultra-deep hydrothermal, mud-brine volcanism. *In Ali Al-Juboury (ed) Contributions to Mineralization Chapter* 2:23–66
- Köbel F (1958) Das Prätertiär der Struktur von Mulkwitz bei Spremberg nördlich des Lausitzer Hauptabbruches. *Geologie* 3/6:676–681
- Kopp JC, Spieth V, Bernhardt HJ (2012) Precious metals and selenides mineralisation in the copper-silver deposit Spremberg-Graustein, Niederlausitz, SE-Germany. *Zeitschrift Der Deutschen Gesellschaft Fuer Geowissenschaften* 163/4: 361–384.
- Mikułski M, Stein H (2017) Re-Os isotopic age of the Cu-Ag sulfide ore and its mineralogical and geochemical characteristic from the Lubin-Polkowice mining area (SW Poland): *Bulletyn: Panstwowego Instytutu Geologicznego* 468:79–96.
- Nawrocki J (2000) Clay mineralogy, crystallinity, and K-Ar ages of illites within the Polish Zechstein basin—Implications for the age of Kupferschiefer mineralization—A discussion. *Econ Geol* 95:241–242.
- Oszczepalski S, Chmielewski A, Speczik S, Krzeminski P (2017) The northwest-trending extension of the Lubin-Sieroszowice Cu-Ag deposit. *Mineral Resources to Discover – 14th SGA Biennial Meeting 2017, v. 3, From fertility to footprints: new vectoring tools for mineral exploration* S08:1159–1162.
- Pašava J, Vymazalová A, Qu W, Korzekwa W (2007) Re-Os study of the Polish Kupferschiefer—Implications for source and timing of metal enrichment. *Goldschmidt Conference 2007, "Atoms to Planets," Cologne, Germany, August 19–24, 2007, conference abstracts,* p A763, <http://goldschmidt.info/2007/abstracts/A763.pdf>.
- Pieczonka J, Piestrynski A, Mucha J, Gluszek A, Kotarba M, Wieclaw D (2008) The red-bed-type precious metal deposit in the Sieroszowice-Polkowice copper mining district, SW, *Annales. Societatis Geologorum Poloniae, Poland* 78:151–280.
- Rahfeld A, Kleeberg R, Moeckel R, Guzmer J (2018) Quantitative mineralogical analysis of European Kupferschiefer ore. *Minerals Engineering* 115:21–32
- Rentsch J (1965) Die feinstratigraphisch-lithologische Floezeparallelisierung im Kupferschiefer am Suedrand des norddeutschen Zechsteinbeckens: *Z. Angew. Geol* 11:11–14.
- Richter G (1941) Geologische Gesetzaessigkeiten in der Metallfuehrung des Kupferschiefers. *Arch. Lagerstaettenforsch.* 73:1–61.
- Sawkins FJ, Burke K (1980) Extensional tectonics and mid-paleozoic massive sulfide occurrences in Europe. *Geol. Rundschau* 69:349–360.
- Schwarzenbach EM, Frueh-Green GL, Bernasconi SM, Alt JC, Shanks III WC, Gaggero L, Crispini L (2012) Sulfur geochemistry of peridotite-hosted hydrothermal systems: Comparing the Ligurian ophiolites with oceanic serpentinites. *Geochimica et Cosmochimica Acta* 91: 283–305
- Spieth V, Trinkler M, Kopp JC, Viehhaus T, Massonne HJ (2014) Cu-Ag-Au-mineralization of the German copper belt – new results from the Spremberg Kupferschiefer deposit, Lausitz, Germany: *DMG, Abstracts: Economic minerals – formation, characterization, and applications, 92nd Annual Meeting, Deutsche Mineralogische Gesellschaft, Jena, ECO-T02:113.*
- Spieth V (2016) Copper-silver-gold deposits: Germany's world class potential in the 21st century. *World of Metallurgy – Erzmetall* 69/1:38–49.
- Spieth V (2018) Hydrothermal gold in Permian black shale Kupferschiefer: A paradigm change in science, exploration and mining. A dynamic model for metal, mud slurry and sand extrudite emplacement. *In Soc. Econ. Geol. Postersession. 2018 Annual Conference Keystone Colorado USA*
- Spieth V (2019) Zechstein Kupferschiefer at Spremberg and related sites: Hot hydrothermal origin of the polymetallic Cu-Ag-Au deposit. *PhD Thesis, Stuttgart, unpublished, 438 p.*
- Tornos F, Solomon M, Conde C, Spiro B (2008) Formation of the Tharsis massive sulfide deposit, Iberian pyrite belt: geological lithogeochemical, and stable isotope evidence for deposition in a brine pool: *Economic Geology* 103,1:185–214.
- Viehhaus T, Spieth V, Massonne HJ (2013) Ramanspektroskopische Untersuchungen an Kupfersulfiden zur Identifikation von Elektrum und Cu/Au/Ag/S Verbindungen aus der Kupferschieferlagerstaette Spemberg, Deutschland. *DMG-GV, Tuebingen, Presentation and Abstract and Presentation 10 p.*
- Wagner T, Okrusch M, Weyer S, Lorenz J, Lahaye Y, Taubald H, Schmitt RT (2010) The role of the Kupferschiefer in the formation of hydrothermal base metal mineralization in the Spessart ore district, Germany: insight from detailed sulfur studies. *Mineralium Deposita* 45:217–239.
- Zientek ML, Oszczepalski S, Parks H, Bliss JD, Borg G, Box SE, Denning PD, Hayes TS, Spieth V, Taylor CD (2015) Assessment of undiscovered copper resources associated with the Permian Kupferschiefer, Southern Permian Basin, Europe: U.S. Geological Survey Scientific Investigations Report 2010-5090-U:94